

CHRISTIAN DAVID DIELEMAN

PATTERNING COLLOIDAL QUANTUM DOTS
WITH LIGHT AND ELECTRONS

Ph.D. thesis, University of Amsterdam, June 2021
Christian D. Dieleman

The work described in this dissertation has been carried out between January 2017 and March 2021 at AMOLF and ARCNL, Science Park 104/106, 1098 XG Amsterdam, the Netherlands. The research was financed by the Netherlands Organization for Scientific Research (NWO).

Printed by GVO drukkers & vormgevers B.V.
Cover design by Kimberly McGuire, based on *"Het Meisje met de Parel"* by Johannes Vermeer, Maurithuis, Den Haag, NL.

This document was typeset using the classicthesis style for L^AT_EX, developed by André Miede.

A digital version of this dissertation can be downloaded from impv.nl and dare.uva.nl.

ISBN: 978-94-6332-760-2



Patterning Colloidal Nanocrystals with Light and Electrons

ACADEMISCH PROEFSCHRIFT

ter verkrijging van de graad van doctor
aan de Universiteit van Amsterdam
op gezag van de Rector Magnificus
prof. dr. ir. K.I.J. Maex
ten overstaan van een door het College voor Promoties ingestelde commissie,
in het openbaar te verdedigen in de Agnietenkapel
op woensdag 30 juni 2021, te 13.00 uur

door Christian David Dieleman

geboren te Goes

Promotiecommissie

<i>Promotores:</i>	prof. dr. A. Polman	Universiteit van Amsterdam
	prof. dr. B. Ehrler	Rijksuniversiteit Groningen

<i>Copromotores:</i>	dr. S. Castellanos Ortega	Inpria
----------------------	---------------------------	--------

<i>Overige leden:</i>	dr. J. van de Groep	Universiteit van Amsterdam
	dr. L. Protesescu	Rijksuniversiteit Groningen
	prof. dr. A.M. Brouwer	Universiteit van Amsterdam
	prof. dr. L. Manna	IIT Central Research Labs Genova
	prof. dr. E.C. Garnett	Universiteit van Amsterdam

Faculteit der Natuurwetenschappen, Wiskunde en Informatica

The sky is clearing and the night
Has cried enough
The sun, he come, the world
To soften up
Rejoice, rejoice, we have no choice but
To carry on

Crosby, Stills, Nash & Young (1970)

Voor mijn lieve ouders, dank voor jullie onwrikbare vertrouwen.

CONTENTS

1	INTRODUCTION	1
1.1	Colloidal quantum dots & perovskite nanocrystals	2
1.1.1	Quantum confinement	3
1.1.2	Synthesis	6
1.1.3	Perovskite nanocrystals	8
1.2	Photo- & electron-beam lithography	9
1.2.1	Photolithography	10
1.2.2	Resolution and roughness	13
1.2.3	Electron-beam lithography	15
1.2.4	Photoresists	16
1.3	Patterning of CQDs and NCs	17
1.4	Outline	19
2	CQD PATTERNING <i>via</i> EUV LITHOGRAPHY	21
2.1	Introduction	22
2.2	Results and discussion	23
2.3	Conclusions	33
2.4	Experimental methods	34
2.5	Appendix	38
3	CQD PATTERNING <i>via</i> E-BEAM LITHOGRAPHY	45
3.1	Introduction	46
3.2	Results and discussion	47
3.3	Conclusions	53
3.4	Experimental methods	54
3.5	Appendix	57
4	DIRECT PATTERNING OF CSPBBR ₃ NCS <i>via</i> E-BEAM LITHOGRAPHY	61
4.1	Introduction	62
4.2	Results and discussion	63
4.3	Conclusion	74
4.4	Experimental methods	74
4.5	Appendix	78
5	TOWARDS WAVEGUIDING AND LASING IN PATTERNED QD FILMS	81
5.1	Introduction	82

5.2	Bragg gratings	85	
5.3	Towards a lasing CQD device		89
5.4	Discussion and outlook	91	
5.5	Conclusions	94	
5.6	Experimental methods	95	
5.7	Appendix	99	
	REFERENCES	107	
	SUMMARY	119	
	SAMENVATTING	122	
	LIST OF PUBLICATIONS	125	
	ACKNOWLEDGMENTS	127	
	CURRICULUM VITAE	135	

ACRONYMS

ACE	Acetone
AFM	Atomic force microscopy
ASE	Amplified stimulated emission
BBO	Beta-barium borate
CAR	Chemically amplified resist
CB	Conduction band
CE	Counter electrode
CQD	Colloidal quantum dot
DFB	Distributed feedback
DI	De-ionized
DUV	Deep-ultraviolet
DUVL	Deep-ultraviolet lithography
DMSO	Dimethylsulfoxide
EBL	Electron-beam lithography
EUV	Extreme-ultraviolet
EUVL	Extreme-ultraviolet lithography
FA	Formamidinium
FTIR	Fourier transform infrared spectroscopy
FRET	Förster resonant energy transfer
FWHM	Full-width at half-maximum
IC	Integrated circuit
IPA	Isopropanol
ITO	Indium tin oxide
LED	Light-emitting diode
LEE	Low-energy electron
LEEM	Low-energy electron microscope
LER	Line-edge roughness

LHP	Lead halide perovskite
LWR	Line-width roughness
MA	Methylammonium
MeOH	Methanol
NC	Nanocrystal
NIR	Near-infrared
OA	Oleic acid
ODE	1-octadecene
ODPA	Octadecylphosphonic acid
OlAm	Oleylamine
PAG	Photo acid generator
PDMS	Polydimethylsiloxane
PL	Photoluminescence
PLQY	Photoluminescence quantum yield
PMMA	Poly(methyl methacrylate)
PRE	Pseudo-reference electrode
PTFE	Polytetrafluoroethylene
QD	Quantum dot
SC	Semiconductor
SNR	Signal-to-noise ratio
SEM	Scanning electron microscope
SHG	Second-harmonic generation
TCSPC	Time correlated single photon counting
TOP	Trioctylphosphine
TOPO	Trioctylphosphineoxide
THF	Tetrahydrofuran
TMS	Bis(trimethylsilyl)sulphide
VB	Valence band
WE	Working-electrode
XPS	X-ray photoelectron spectroscopy
YAG	Yttrium aluminium garnet

INTRODUCTION

"It is a capital mistake to theorize before one has data."

— Sherlock Holmes

Colloidal quantum dots (CQDs) and other semiconductor (SC) nanocrystals (NCs), like perovskites, have developed to be a high-performance and reliable platform for numerous applications ranging from photovoltaics [1–3], to light-emitting diodes (LEDs) [4–6], single photon sources [7, 8], transistors [9, 10] and many more [11–13]. This class of nanocrystals is extremely versatile due to their tunable properties in terms of size, composition and surface chemistry, which in turn influence important characteristics like bandgap, absorption and emission wavelengths, photoluminescence quantum yield, charge transport, processability, colloidal stability and film formation properties [14]. Extending the unique tunability of these nanocrystals by patterning them on the micro or nanoscale can lead to entirely new applications, for instance small LEDs for high resolution (flexible) displays [15] or waveguiding structures that support directional emission [16]. Ultimately, nanostructuring on the scale of the wavelength of light can lead to collective effects such as resonances, allowing for enhanced emission and absorption of metasurfaces [17]. Manufacturing of these structures usually requires multiple intricate processing steps, like stamping [15], template stripping [16] or multistep lithography with lift-off [18]. In this thesis we explore the use of lithographic techniques to pattern several types of CQDs and NCs at the nanoscale. In the following sections we will first introduce the concepts that are important to the understanding of the work presented here.

1.1 COLLOIDAL QUANTUM DOTS & PEROVSKITE NANOCRYSTALS

Colloidal quantum dots are nanocrystals made from inorganic semiconductor materials and have been a research field of interest due to their interesting properties. In bulk SCs there are bands of allowed energy states for the electrons in the crystal with an energy gap between the occupied and unoccupied states, the bandgap. The band below the bandgap in energy is mostly occupied with electrons and is called the valence band (VB), while the band above the bandgap, the conduction band (CB), is mostly empty. However, when electrons are given enough energy, either due to thermal energy, by excitation with radiation or other ener-

getic electrons, then electrons are able to move from the VB into the CB, where they are free to move through the crystal lattice. The positive hole that was left behind in the VB can also move through this band, allowing for the movement of charges through the crystal, and thus the conduction of electricity. In the reverse process, an electron in the CB can recombine with a hole in the VB while emitting a photon of the bandgap energy. In bulk SCs the energy needed to promote an electron to the higher energy CB is typically in the order of near-infrared (NIR) and visible light, making it an interesting class of materials for applications where light can be detected or used as energy source, like photodetectors, photovoltaics and photocatalysis, as well as light emitting applications like LEDs and lasers, and as electronic devices such as transistors.

1.1.1 *Quantum confinement*

What sets quantum dots (QDs) apart from bulk SCs is the fact they exhibit the quantum confinement effect. This effect is related to the exciton Bohr radius in the material. QDs are small particles made from semiconductor material where the size is smaller than this Bohr radius. When an electron is excited to the CB and leaves a positive hole behind in the VB, this electron-hole pair is bound to each other by the Coulomb force and forms a neutral quasi-particle, the exciton. The radius of this interaction is described by the exciton Bohr radius (Equation 1.1):

$$r_{Bohr} = \frac{\epsilon_r \hbar^2}{e^2} \left(\frac{1}{m_e^*} + \frac{1}{m_h^*} \right) \quad (1.1)$$

where:

- r_{Bohr} = Exciton Bohr radius
- ϵ_r = Dielectric constant of the material
- \hbar = Reduced Planck's constant
- e = Elemental charge
- m_{e^*} = Effective mass of the electron
- m_{h^*} = Effective mass of the hole

If this exciton Bohr radius is larger than the crystal, the wavefunction will be confined, much like the particle-in-a-box model of simple atoms. This leads to a discretization of energy levels as the spacing between the different states becomes larger than thermal energy kT , and an increase in the bandgap energy as shown in Figure 1.1a (adapted from [14]). This increase in bandgap can be calculated with equation 1.2.

$$E_{QD} = E_0 + \frac{\hbar^2 \pi^2}{8r^2} \left(\frac{1}{m_{e^*}} + \frac{1}{m_{h^*}} \right) \quad (1.2)$$

where:

- E_{QD} = Bandgap of the quantum dot
- E_0 = Bulk bandgap
- \hbar = Reduced Planck's constant
- r = Radius of QD

Equation 1.2 shows an inverse quadratic dependence of the bandgap on the size of the crystal. In practice, this means that by shrinking the crystal size, the bandgap is increased and absorption and emission blue-shift. Vice versa, by growth of the crystal the bandgap reduces and emission red-shifts, as first described by Ekimov et al. in the early 1980s [19]. The confinement effect will diminish as the crystals grow and the bulk bandgap will be approached when the crystal size becomes larger than the Bohr radius. This is indeed a trend that is observed in practice. Figure 1.1b and c show the absorption spectra of different

sized PbS CQDs [20] and the emission of different sized CdSe CQDs respectively. The shift in bandgap is apparent in both cases and is a beautiful tool to optimize the bandgap for the desired application.

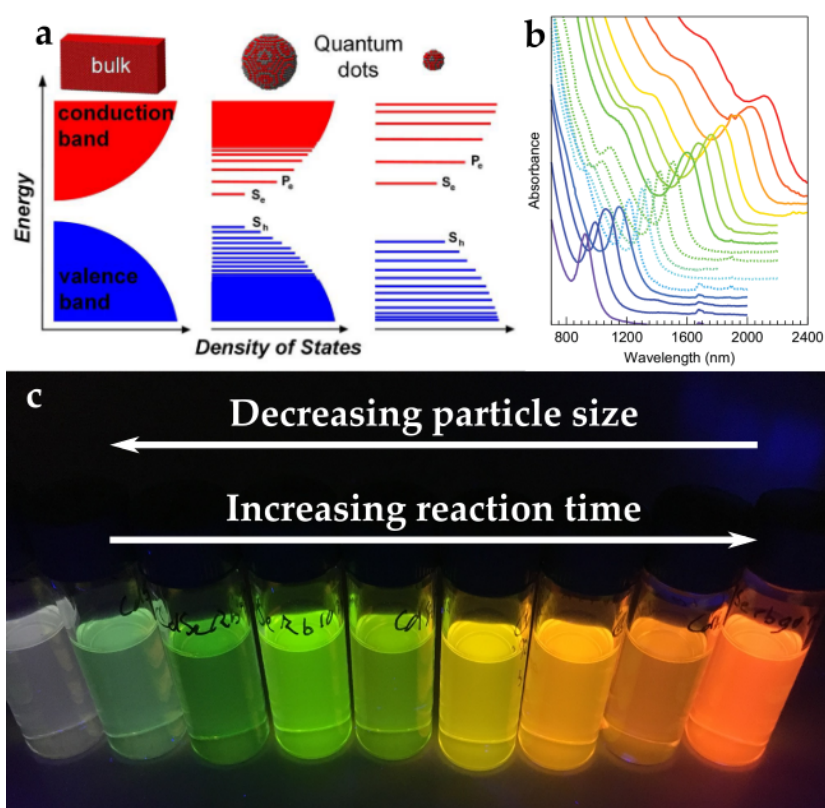


Figure 1.1: (a) Size dependence of energy levels in semiconductors. By reducing the size of the crystal, the energy levels become discrete and further separated. Adapted from [14]. (b) Absorption spectra of differently sized PbS CQDs. Smaller crystals result in a blue-shift of the absorption. Adapted from [20]. (c) Emission of differently sized CdSe CQDs as synthesized by the author. There is a clear shift in the emission wavelength as a result of a change in confinement. From left to right the CQDs were given more time to grow, and are therefore larger.

Due to their optical behavior CQDs are sometimes also referred to as artificial atoms, since their energy levels are discrete. Therefore the absorption spectrum shows distinct peaks, and the emission wavelength is comparably sharp and well-defined. Still, since CQDs are usually assembled and measured in ensembles,

any variation in their sizes leads to a broadening of absorption and emission. With advanced synthetic protocols this variation in size does not account for a large variation in emission wavelengths, meaning that the full-width at half-maximum (FWHM) can be well below 100 meV.

1.1.2 *Synthesis*

Although the first QDs were embedded in a glass matrix [19] a major boost to the field came after the development of the hot-injection synthesis method introduced by Murray et al. [21]. This method is now the most common way to produce CQDs in large quantities and with small size-dispersion, following the LaMer growth model [22]. In a hot-injection synthesis, depicted in Figure 1.2a, typically one precursor is heated up in high-boiling point solvent together with surfactants, after which a second precursor is rapidly added. Due to the high temperature, usually well over 100 °C, the precursors decompose into monomers. The rapid injection creates a state of supersaturation which is resolved by rapid nucleation of small crystals. It is key that the nucleation phase ends quickly, so all crystals start growing at the same time and end up at the same size. Nucleation will stop when the concentration drops below the nucleation threshold or when temperature drops after injection. This initiates stage two, where the crystals start growing due to addition of the monomers to the existing crystals. During this stage two competing processes are present, influencing the CQD size. Size focusing ensures that the crystals are growing at different rates based on their size. Due to diffusion-limited growth, larger crystals will increase in size slower than smaller crystals, allowing them to “catch up” in their growth, such that the sizes of the particles will grow closer to each other over time. At the same time, Ostwald ripening causes larger particles to keep growing by incorporating smaller particles, thereby causing defocusing of the particle size. Since the larger surface-to-volume ratio of small particles is energetically unfavorable, smaller particles tend to merge with the bigger crystals over time. Next to this, smaller crystals are easier to redissolve, especially in unstable temperature conditions. Since the focusing effect is usually observed first, it is key to terminate

the growth stage at the right moment by cooling the reaction with a water or ice-bath, or the injection of a cold solvent.

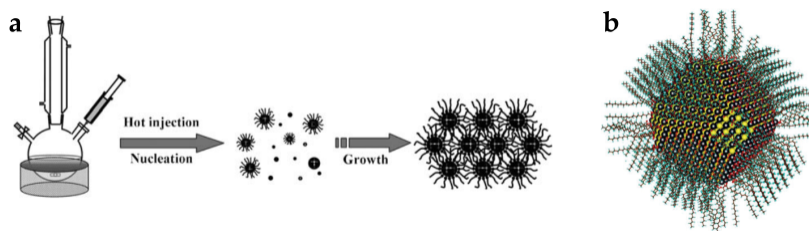


Figure 1.2: (a) Typical hot-injection CQD synthesis. Adapted from [23]. (b) Representation of PbS quantum dot with attached surface ligands. Adapted from [24].

Long organic molecules are used in order to stabilize the crystals during the growth. Typical examples include oleic acid, oleylamine and trioctylphosphine oxide. The high surface-to-volume-ratio of CQDs makes them very susceptible to surface reactions, like oxidation, that would introduce trap states in the bandgap. The ligand molecules have a charged endgroup (carboxylic acid, amine or thiol), that is able to passivate the surface of the crystal, while the long hydrophobic tail ensures colloidal stability in the solvent, giving CQD their name. Moreover, the type and ratio of the ligands used can influence which facets of the growing crystals are being terminated during growth, thereby influencing the shape of the CQDs. After synthesis, these surface ligands can be exchanged in order to passivate the surface better, reducing the number of trap states in the bandgap which is beneficial for properties like photoluminescence quantum yield (PLQY). Next to this, changing the ligands can also alter the local electronic landscape which can be beneficial for charge transport or luminescent properties [25–28]. Exchanging the ligands can also make the CQDs compatible with other matrices like polymers, or make them even water-soluble [24].

Growing a passivating shell around the core, either directly [29, 30] or by ion exchange after the initial synthesis [31], is another effective way of passivating the surface of the core crystal. This is also the reason that the reactions are usually performed under inert, oxygen- and water-free conditions in a three-neck flask. The second benefit of shells is the fact that they can introduce

extra compositional freedom, that is for instance beneficial for reduction of Auger recombination [32].

1.1.3 Perovskite nanocrystals

A class of nanocrystals that has gained attention in the past few years is that of lead halide perovskite (LHP) nanocrystals. Perovskites have shown a tremendous potential for optoelectronic applications due to their rapid rise in solar cell efficiency from 2.2% in 2006 [33] to 25.6% [34] in 2021, which is already rivaling the most efficient silicon solar cells at 26.7% [35] that have been under investigation for over 40 years. The name perovskite is related to a general crystal structure with a composition of ABX_3 . The crystal consists of a cubic or tetragonal lattice with cornersharing octahedra, shown in Figure 1.3a. In LHPs, the A-site holds a large cation in between the octahedra, often methylammonium (MA) or formamidinium (FA) in hybrid perovskites, Cs, in a fully inorganic perovskite or a mixture of some or all of these. The B-site inside the octahedra is occupied by Pb or Sn and the corners of the octahedra are (a mixture of) halides ($X = \text{I}, \text{Br}, \text{Cl}$) [36]. Typical LHP NCS of around 15 nm are shown in Figure 1.3b.

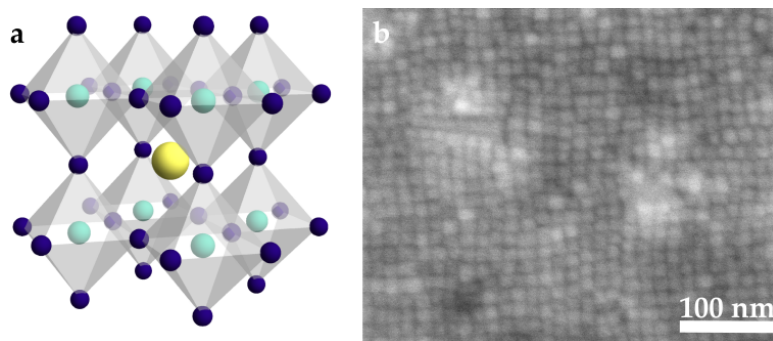


Figure 1.3: (a) The perovskite crystal structure of cornersharing octahedra. The yellow A-site atoms are in between the octahedra with the halides (X-site) at the corners (blue) and a heavy Pb or Sn atom (B-site) in the center (green). (b) Example of 15 nm sized LHP NCS.

LHP NCS are interesting due to their excellent light emission properties and tunability. Already in the first reports of colloidal

perovskite NCs, it was shown that the emission can be tuned through the whole visible spectrum by simply changing the halide composition [37]. Note that this is different to the II-VI CQDs discussed above, where the bandgap tunability was achieved through quantum confinement rather than composition engineering. The emission spectrum is also very narrow (<100 meV) and PLQY of over 90% has been achieved [38–40]. One of the reasons for the high performance of LHP NCs is their high tolerance to defects. This tolerance means that the bandgap emission depends less on the surface atoms, which makes the crystals relatively insensitive to small changes in the surface passivation [41].

The defect tolerance also makes the synthesis of LHP NCs relatively straight-forward. The most common synthesis route is via the hot-injection method, developed by Protesescu et al. [37]. A precursor of lead-halide is heated in a non-coordinating high boiling point solvent and a second precursor, like Cs-oleate, is added to the mixture in the presence of surface ligands. These ligands passivate the surface and terminated certain facets, to control the overall shape of the crystals [42]. The crystals form very quickly, in the order of seconds, due to their ionic nature, and NCs can even be formed at room temperature [43]. One of the more difficult challenges is the purification. Due to their ionic nature, LHP NCs are (at least partly) soluble in polar solvents. Next to this the ligands are not strongly bound to the crystals, which makes the particles sensitive to aggregation and loss of colloidal stability in the purification process, diminishing their optical properties. Despite these challenges, many devices have been made with LHP NCs, for example highly efficient LEDs [5, 44, 45] and solar cells [2, 46].

1.2 PHOTO- & ELECTRON-BEAM LITHOGRAPHY

Photolithography, also called optical lithography, is a process used in semiconductor industry to transfer patterns onto a substrate as part of the manufacturing of integrated circuits (ICs) [47]. After this pattern transfer it is possible to etch into the substrate or to deposit new layers only in desired areas, thereby allowing the manufacturing of small devices like transistors. Advances in

photolithography have allowed to follow Moore's Law, a prediction made in 1965 and later adjusted in 1975 by Gordon Moore, that advances in fabrication would allow the number of transistors on the same area to increase by a factor 2 every 2 years [48, 49]. So far, this trend has indeed been followed, although in the last years we have observed a slow down in feature shrinkage due to technical challenges. The advancements in manufacturing have led to a remarkable increase in computing power, while the price of ICs has dropped significantly, allowing us to carry powerful computing devices in our pockets.

Electron-beam lithography (EBL) is a similar technique, which uses incident electrons from a scanning beam, rather than incident light. Due to the high accuracy of positioning of the electron beam, very small resolutions of <10 nm are possible [50]. The process is, however also slower than photolithography, making it especially popular for small scale prototyping [50] instead of high volume manufacturing [47].

1.2.1 *Photolithography*

In photolithography, patterns are projected onto a light-sensitive layer, the photoresist, that undergoes a chemical change, making the material either soluble or insoluble. This allows for subsequent dissolution of a part of the film in desired areas. Figure 1.4 shows the different steps in the lithographic process.

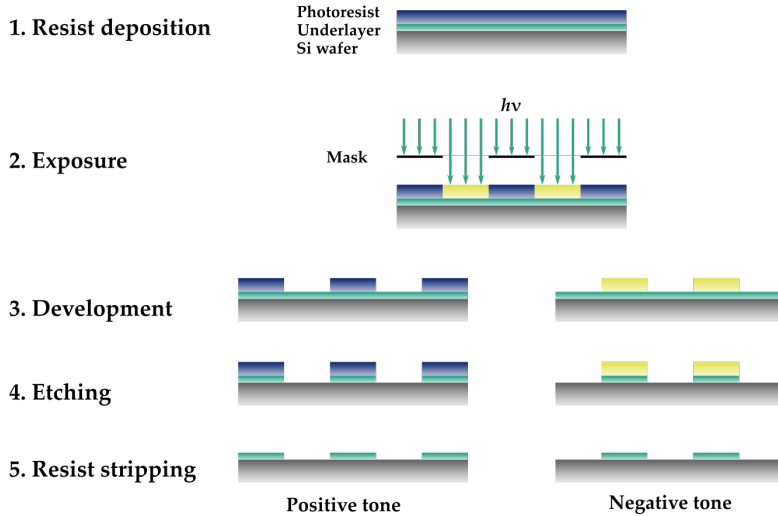


Figure 1.4: The main processing steps in photolithography used to transfer patterns into the photosensitive resist layer.

The resist is usually applied on the wafer through spin coating. This layer is usually thin, in the order of 10s of nanometers [51]. The application of the resist material should be uniform across the wafer, in order to ensure uniform patterns. The second step is exposure which induces chemical changes in the photoresist, that can be either positive-tone or negative-tone [52]. In positive-tone materials, the exposed part is easier to dissolve after exposure, while negative-tone photoresists will be harder to dissolve after exposure resulting in a solubility contrast between exposed and unexposed areas.

Exposure is typically done by shining a light source through a mask, blocking the light in some places and transmitting it in others. The shape of this illumination pattern is important for the final shape of the developed features. In negative photoresists, a certain density of absorbed photons is required to induce a solubility switch, that will turn the material insoluble in the developer. Depending on the shape of the incoming light source and the slope between areas of low and high intensity. Preferably this slope is as steep as possible, to create a precise contrast between intended patterns and intended spaces. The dose cor-

responding to this density of photons is usually designated as D_0 . The material starts to convert into the insoluble product, everywhere on the sample where this threshold is reached. The features will be very small in cases where only the locations with maximum intensity reach the required number of photons for conversion of the material. By increasing the exposure dose, more and more of the projection field will receive the required dose of photons D_0 . When the intensity slope is shallow enough, the printed features will become wider and wider with increasing dose. This principle is demonstrated in Figure 1.5. In interference lithography, that is often used in research, 2 or more coherent extreme-ultraviolet (EUV) light beams interfere to project patterns on the desired material [53]. The sinusoidal shape of this interference pattern has an influence on the quality of the final patterns.

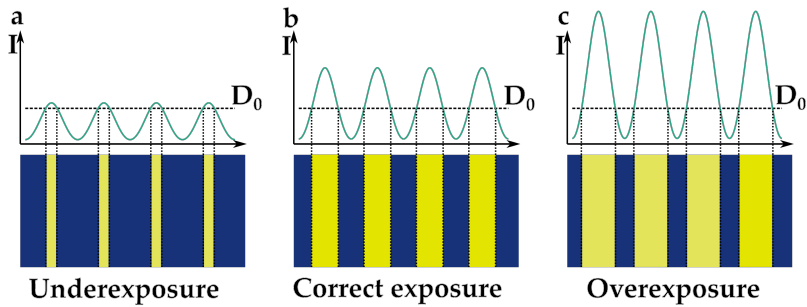


Figure 1.5: The intensity profile of the projected pattern in interference lithography has a direct influence on the patterned features. (a) The solubility switch will only occur where the intensity threshold D_0 is reached. (b) When the exposure dose is increased and the intensity slope is shallow enough, a larger part of the exposed area will receive the minimum required dose for a solubility switch and the features will widen to the correct exposure. (c) If the dose keeps increasing the features will widen further and wider features than desired remain.

The next step in the process is the development, sometimes preceded by a post-exposure bake. Depending on the chemical mechanism behind the solubility switch, for instance chemical cross-linking, a post-exposure bake can aid with the diffusion of reactive species through the photoresist, which helps to smooth line-edges and can reduce the required dose necessary for patterning [47, 54, 55]. Finding the right development conditions

is critical for creating the desired features to the right degree of precision. The chosen developer needs to be selective enough to quickly dissolve the right part of the resist, but very fast dissolution can cause the resist to be "ripped off" the substrate. Next to this, during development, capillary forces between lines of resist can cause pattern collapse, partly blocking the substrate in areas where it should be exposed [56]. Finding the right development conditions is therefore an important aspect of lithography. After development, part of the substrate or underlayer is exposed and can be etched away or a new functional layer can be deposited on top. After resist stripping, the desired features are left on or in the substrate.

1.2.2 Resolution and roughness

The typical exposure source has moved in the past decades from deep-ultraviolet (DUV) (Hg-i-line-lamp, $\lambda = 365$ nm, 3.4 eV) to excimer lasers like KrF ($\lambda = 248$ nm, 5.0 eV) and ArF ($\lambda = 193$ nm, 6.4 eV) [57]. The light source and optics determine the fundamental limit for the features that can be patterned. The smallest resolution is derived from the diffraction limit [47]:

$$CD = k_1 \frac{\lambda}{NA} = k_1 \frac{\lambda}{n \sin \theta} \quad (1.3)$$

where:

CD = Critical dimension

k_1 = Process-dependent parameter, typically >0.25

λ = Wavelength

NA = Numerical aperture

n = Refractive index of background medium

θ = Maximum angle of incidence of the focused light

This principle limits the smallest resolution of these DUV systems in air ($n = 1$) to about 48 nm for a single exposure. With immersion lithography (high NA) and multiple patterning steps this can be stretched a bit further, but for sub-20 nm features a

new wavelength is necessary [57, 58]. This is why in recent years a lot of effort has been put into developing extreme-ultraviolet lithography (EUVL), which operates at the much shorter wavelength of $\lambda = 13.5$ nm (91.9 eV). Despite the many challenges, the first EUV-based fabrication has started in 2019 [59].

As in optical lithography when whole wafers are exposed at once with extremely small features, uniformity is an important parameter. A rough line can lead to yield losses, when two lines touch, or can cause signal disturbance in the final devices. Control of the line-width roughness (LWR) and line-edge roughness (LER) are therefore critical, especially for reaching smaller scales.

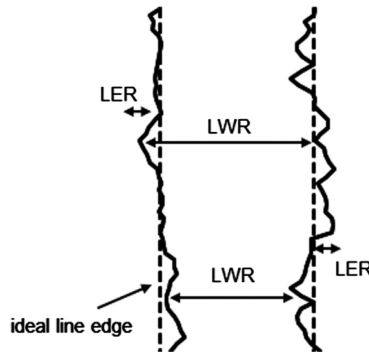


Figure 1.6: The line-edge of a real exposed and developed feature is never the ideal line edge. Variations in the width of the feature as well as the roughness are important parameters. The LER is 3σ variation from the ideal line edge. LWR is defined as 3σ variation of the features' width [47].

Figure 1.6 shows the LER and LWR as compared to the intended line. LER is defined as 3 standard deviations (3σ) of an edge from a line fit to the edge, LWR is the 3σ deviation of the width. Several factors can play a role in the formation of LWR and LER including resist formulation, development and, with decreasing exposure doses, even shot noise: the fact that photons behave like particles when used in low numbers [60]. Achieving low LER and LWR is therefore a trade-off with the sensitivity of the resist and the dose required for good pattern transfer.

1.2.3 Electron-beam lithography

Electron-beam lithography ^{EBL} is a technique where, analogous to photolithography, small patterns are transferred onto a layer of material sensitive to the incoming radiation. As with photolithography, the material will show a change in solubility upon exposure, allowing selective dissolution. The main advantage of ^{EBL} over photolithography is that it can be used to write sub-10 nm features without the use of a mask, since the wavelength of an electron is much smaller than that of even highly energetic EUV photons [50]. The kinetic energy of an electron accelerated at a certain voltage equals:

$$E = qV = eV_{acc} = \frac{m_e v_e^2}{2} \quad (1.4)$$

with:

E = Kinetic energy of accelerated electron

q = Charge of particle

V_{acc} = Acceleration voltage

e = Elemental charge, $1.602 \cdot 10^{-19}$ C

m_e = Mass of electron, $9.109 \cdot 10^{-31}$ kg

v_e = Velocity of electron

De Broglie's equation 1.5 relates the wavelength λ of a fast traveling particle with its momentum p .

$$\lambda = \frac{h}{p} = \frac{h}{m_e v_e} \quad (1.5)$$

with:

λ = Wavelength of particle

h = Planck's constant, $6.626 \cdot 10^{-34}$ J s

p = Momentum of particle

By filling in equation 1.4 into 1.5 we can now calculate the wavelength for an electron that is accelerated at 50 kV, a typical voltage

for e-beam systems, to be $\lambda = 5.48 \cdot 10^{-12}$ m or 5.48 pm only. This allows e-beam systems to write incredibly accurately. The trade-off for this precision is the speed. In contrast to photolithography, where a whole pattern can be projected on a wafer at once, EBL is a maskless method that requires the beam to travel along the sample turning on and off where desired, much like writing with a pen or pencil. This does allow for incredible freedom in the design, as the design is not limited to a mask. On top of that, designs can be easily changed from exposure to exposure, without the need for fabrication of masks, which makes this a desired tool for small volume precision manufacturing, like lab-scale prototyping [50]. The resolution of EBL is, in practice, not as small as the electron wavelength, or even as small as the electron optics would allow. It is limited by practical limits like electron scattering length, secondary electron generation and charging [47]. The electrons from the incoming beam as well as secondary electrons caused by elastic and inelastic scattering deposit energy in the resist leading to resist cross-linking or breaking molecular bonds and creating reactive radicals [55]. Additionally, electrons can backscatter from the substrate, as the highly energetic electrons mostly pass through the thin resist films.

1.2.4 Photoresists

For optimal patterning with different techniques, different types of resist exist. In DUV, the most common type of resist is the chemically amplified resist (CAR), where photo acid generators (PAGs) are dispersed in a matrix of polymer. Upon exposure to DUV light, the electrons in PAG are excited which causes a dissociation leading to the release of a proton (H^+). This acid can subsequently attack certain side groups in the polymer chain in a process called deprotection. The deprotected groups have a different polarity than the original group, causing a solubility switch. Since the acid used for deprotection leads to the creation of another acid, 1 absorbed photon in a PAG can lead to more than 1 deprotection reaction, thereby amplifying the effect of the photon [61]. A post-exposure bake can aid in the diffusion of acids, thereby increasing the sensitivity of the resist. In order to quench the reaction, usually a small amount of bases is present

in the resist as well, to make sure the reaction does not continue too far away from the original absorption event, thereby blurring exposed features [47].

In non-CAR resists, other reactions can also be observed. Poly(methyl methacrylate) (PMMA) can, for instance, undergo scission reactions that break the polymer chain, reducing the molecular weight of the chain, making it more soluble after exposure [62]. These types of reactions happen due to the high energy of the photons or electrons, which is higher than the energy of typical C-C bonds or C-H bonds. Therefore, absorption of an EUV photon or irradiation with a highly-energetic electron can also lead to the creation of reactive radicals that can initiate polymerization reactions [63].

Most CARs are fully organic molecules, heavy in carbon, oxygen and hydrogen. Since the absorption cross-section of these elements for EUV is very low [64], the sensitivity for EUV is low. In order to increase the absorption of EUV, a new class of resists has emerged in the form of metal-based hybrids. These are small nanoparticle based resists with an inorganic core with a size of 1 - 2 nm, surrounded by organic shells that can provide solubility. Many different materials have been developed which are for instance based on Zr, Hf [65, 66], Sn [52, 67, 68] or Ti [69]. The materials have shown promise as EUV resist. Due to the analogous nature of CQDs with these nanoparticle based photoresists, it is interesting to investigate the direct patterning of CQDs with EUVL and EBL.

1.3 PATTERNING OF CQDS AND NCS

CQDs have been patterned with many different approaches like self-assembly [70, 71], template stripping [13, 16], dry-stamping [15], inkjet printing [6, 72], imprint lithography [73, 74], multi-step lithography with resists [18], or direct lithography [75–79].

In self-assembly approaches, substrates are initially patterned with self-assembled monolayers. By tailoring the surface ligands of the CQDs, the interactions with the monolayers are altered, either attracting or repelling them, leading to self-assembly of the crystals after immersion or dropcasting [70, 71]. Downsides of this method are the multi-step processing and the fact that

a functionalization of the surface isolates the CQDs from the substrate, which is bad for charge transfer in electronic devices. Next to this, it is challenging to pattern at sub-micron resolutions.

The template stripping method, applied by the Norris group [13, 16], uses e-beam patterned templates of etched silicon. After etching, the patterns are filled by dropcasting CQD solutions on top. After dropcasting epoxy on top followed by deposition of a glass slide, the epoxy layer is cured and patterns can be stripped from the mold. The resulting structures are well-defined and the templates can be reused. The method does, however, require multiple steps for fabrication, and a new template is needed for every new design.

Dry-stamping is another transfer technique. A CQD layer is spincoated on a functionalized surface and a patterned polydimethylsiloxane (PDMS) stamp is used to transfer parts of the film to a new desired substrate. Benefits are the large area that can be patterned, as well as layer-by-layer deposition. The resolution, however, is limited to the micron range.

Inkjet printing works by directly depositing CQD inks as droplets on the substrate [72] or into patterned photoresist layers. It allows for good precision of deposition, but the uniformity can be a challenge due to non-uniform solvent evaporation after deposition. This also makes it challenging to fabricate structures with straight side-walls.

Several lithography techniques for patterning CQDs have been used as well. Imprinting techniques show a lot of promise for patterning large areas with high resolution [73, 74], but have the downside that the CQDs need to be embedded in a curable matrix, reducing the density of CQDs and isolating them from each other. Multi-step lithography with lift-off, seems the most straightforward method of patterning CQDs. A resist is patterned and developed after which the CQDs are dropcasted or spin-coated on top. After lift-off, good quality structures remain, although the lift-off process is challenging due to CQDs sticking to the sidewalls of the resist.

In direct lithography, the CQD material itself is exposed to a photon or electron source leading to changes in the ligand chemistry that allow a selective dissolution of the unexposed crystals. A direct patterning method, developed in the group

of Talapin, used the photodegradation of the capping ligands under UV [77] and blue light [78]. The technique yields clear structures without affecting the CQDs. The resolution is, however, limited by the wavelength of light used for exposure. Palazon et al. used an X-ray photoelectron spectroscopy (XPS) source ($\lambda = 0.83$ nm, 1486.6 eV) to pattern perovskite NCs directly by cross-linking the ligands [76]. Shadow masks were used to pattern the material at microscale, although the wavelength of light would allow for smaller structures. Next to making patterns by selective dissolution, the exposure also impeded ion-exchange in the crystals, which allowed for selective ion-exchange in the film to create areas with different composition and thus different emission. Little work has been done on patterning CQDs with e-beam lithography. Nandwana et al. showed patterning of CdSe [75] with trioctylphosphineoxide (TOPO) ligands and more recently Dement et al. [79] showed direct patterning of CdSe for precise placement of emitter material in a photonic application.

1.4 OUTLINE

This thesis seeks to shed light on the possibility to pattern CQDs by advanced lithographic methods. Due to their inherent functionality, CQDs are interesting to pattern on the scale that photolithography and e-beam lithography unlock. In *chapter 2* we discuss the patterning properties of as-synthesized PbS and CdSe CQDs when exposed to EUV and discuss the mechanism leading to patterning as well as the optical properties of the patterned materials. In *chapter 3* we discuss the effect of e-beam irradiation on the same materials. Next, in *chapter 4* we discuss how we can pattern a new emerging class of nanoparticles, perovskites nanocrystals, with the use of EBL and we discuss the effects on its optical properties. Finally, in *chapter 5* we discuss an application for the nanopatterning of CQDs with direct lithography in the form of a Bragg grating which manipulates the direction of light emission and paves the way to a lasing CQD device.

COLLOIDAL QUANTUM DOT PATTERNING VIA EXTREME UV LITHOGRAPHY

*“Het zien duurt een seconde, de gedachte blijft voor
altijd.”*

— Thé Lau, *Blauw* (1990)

Parts of this chapter have been published in:

Dieleman, C. D., Ding, W., Wu, L., Thakur, N., Bespalov, I., Daiber, B., Ekinici, Y., Castellanos, S. & Ehrler, B. "Universal direct patterning of colloidal quantum dots by (extreme) ultraviolet and electron beam lithography", *Nanoscale* **2020** 12(20), 11306-11316

2.1 INTRODUCTION

Photolithography is a major manufacturing technique for patterning many functional materials at the nanoscale and is essential for the semiconductor devices that power our modern world. Typically, nanostructures for large-scale applications are written by (deep-) ultraviolet lithography ($\lambda = 193 - 365$ nm, deep-ultraviolet lithography (DUVL)). The resolution of DUVL is limited by its wavelength and sub-20 nm features can only be reached with complex multi-step exposures. This complexity pushes the industry to introduce a new technique based on extreme-ultraviolet lithography ($\lambda = 13.5$ nm, EUVL), which is currently rolling out to become the standard in large-scale lithography manufacturing for the highest performance integrating circuits over the next years. Photolithography processes rely on masks to write the nanostructures onto a substrate covered with photoresist. The illuminated light induces a solubility change of the resist, which allows for subsequent dissolution of either the illuminated (positive tone) or unexposed (negative tone) areas.

Although photolithography is often carried out as an intermediate step in order to deposit or partially remove an active material, previous work has been carried out on patterning active materials in the form of colloidal quantum dots via photolithographic processes. Wang et al. exploited the degradation of 1,2,3,4-thiatriazole-5-thiolate capping ligands. These are soluble in polar solvents, and become insoluble thiocyanate ligands, by UV-radiation ($\lambda = 254$ nm) [77]. This approach with other light-sensitive ligands was later expanded to include blue-light lithography ($\lambda = 405, 450$ nm) as well [78]. Palazon et al. used X-rays from an XPS source ($\lambda = 0.83$ nm, 1486.6 eV) to pattern nanocrystals directly by cross-linking the ligands [76].

Here we show a general, single-step, resistless method that allows direct patterning of two different semiconductor quantum dots (CdSe, PbS) with either low-energy DUV or high-energy EUV photons (5.5 eV or 91.9 eV; DUV & EUV). We find that the quantum dot ligands cross-link upon exposure, making the exposed areas insoluble. This technique allows patterning of nanostructures down to tens of nanometers. The photoluminescence (PL) efficiency remains almost constant upon patterning, making the

patterning technique suitable for optical applications.

2.2 RESULTS AND DISCUSSION

We synthesized two types of colloidal quantum dots from CdSe and PbS. These materials have been used in e.g. solar cells and for light emitting applications. Both materials were capped with their native ligands oleic acid, a mono-unsaturated long (C18) carboxylic acid. We then deposited these CQDs by spin coating thin films onto silicon substrates and exposed them to three different UV light sources in the form of near-UV light ($\lambda = 365$ nm, 3.4 eV) from a MA BA 6 Mask aligner, DUV light from a yttrium aluminium garnet (YAG) DUV laser ($\lambda = 225$ nm, 5.5 eV) and EUV light ($\lambda = 13.5$ nm, 91.9 eV) from a synchrotron (Swiss Light Source). To pattern the CQDs by EUVL we used open frame exposure for large areas (0.5×0.5 mm), or diffractive transmission optics to write either lines or pillars using interference lithography. The size of the features was varied by changing the grating period. After exposure the samples were developed by dipping the samples into toluene or hexane for 10 seconds.

By exposing the CQDs to the EUV light or chemical reactions are induced. These reactions can include cross-linking between the quantum dot ligands, upon which exposed areas become insoluble in the developer. This solubility change allows for contrast between the exposed and unexposed areas and the formation of nanostructures of nanocrystals (Figure 2.1a). Upon exposure with EUV photons, the high energy of the photons induces ionization events in the absorbing atom, leading to the creation of photoelectrons, holes and reactive radicals [55]. These electrons typically still have a relatively high energy of around 80 eV [80] and can scatter inelastically with other electrons, losing energy along the way. The energy transfer from the photoelectron to the surroundings can promote excitations and even ionization events. Typical chemical bonds in organic materials, like the C-C or C-H bond have a bond strength of 3.6 eV and 4.4 eV respectively [81]. Yet even electrons with energy much lower than this bond strength can induce chemical change in the material by means of dissociative electron attachment, where electrons are trapped by

a molecule in an antibonding orbital. [55, 82] This process results in bond cleavage and subsequently in the generation of reactive species like radicals which can react with double bonds and induce the formation of new bonds, leading to the carbon chains cross-linking [83, 84]. As the absorption of one EUV photon can lead to a multiple of lower-energy photoelectrons, EUV radiation can have an inherent chemical amplification, possibly requiring lower exposure doses.

Based on the potential cross-linking chemistry of oleic acid ligands, we anticipated that exposure to radiation could transform the material into a cohesive network of nanocrystals which is insoluble in the developing solvents, even though the unexposed quantum dots are colloidally stable in the same solvents for months. After spin coating thin films of PbS and CdSe we exposed them to EUV radiation. Figures 2.1b-e show scanning electron microscope (SEM) images of pillars written in PbS CQD films by EUV (180 nm pillar diameter, 400 nm pitch, 140 mJ cm^{-2} , Figure 2.1b,c) and line/space patterns written by EUV in CdSe CQD films (50 nm line width, 100 nm pitch, 55 mJ cm^{-2} , Figure 2.1d,e). More examples can be found in the appendix, section 2.5. A clear contrast is observed after development, as the CQDs remain in the areas where the sample was exposed to EUV light. The pattern is visible and uniform over large areas of several μm^2 . The development is rapid, with almost no CQDs left in the unexposed areas after 10 seconds of immersion in the developer.

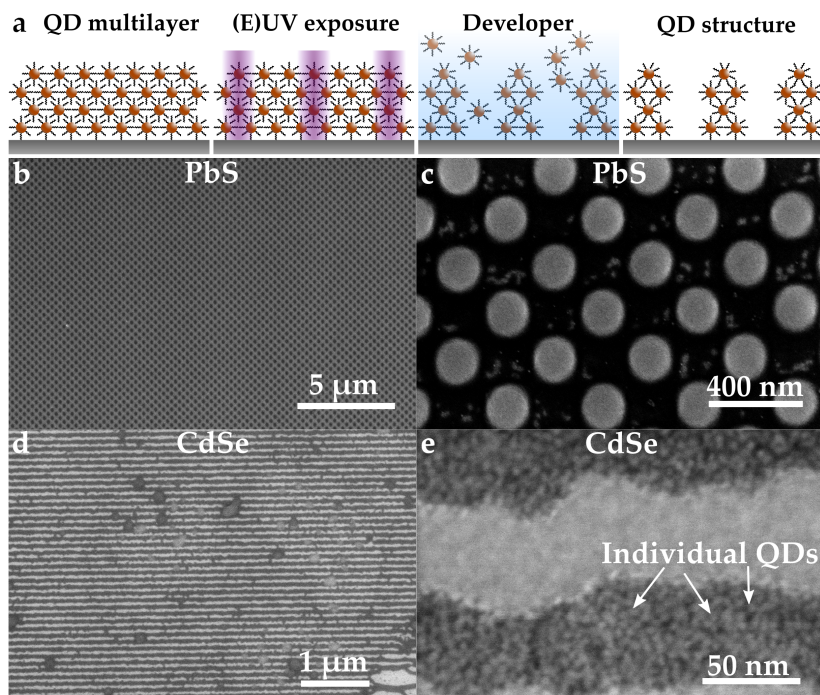


Figure 2.1: (a) Direct quantum dot patterning with different UV sources. Colloidal quantum dots are spin-coated onto silicon substrates to form thin films. After irradiation with photons with different energies, the particles cluster together through cross-linking of their organic shells. After submersion in an apolar developer, the irradiated structures remain on the substrates, while non-irradiated quantum dots dissolve. Images (b-e) are SEM images. (b) Large field of patterned PbS pillars (180 nm diameter, 400 nm pitch) after EUV-exposure (140 mJ cm^{-2}) and development. Very few defects are present. (c) Close-up of patterned PbS pillars. (d) Large-scale field of EUV-patterned CdSe lines. Exposure dose 55 mJ cm^{-2} . (e) Close up of CdSe lines. The individual quantum dots can easily be identified.

To identify the chemical changes leading to the clustering of the nanocrystals and their solubility switch, we investigated samples exposed to different doses of EUV light (0 to 340 mJ cm^{-2}) with Fourier transform infrared spectroscopy (FTIR). The CQD ligand, oleic acid, is a relatively simple molecule, an 18-carbon-atom long mono-unsaturated molecule, with a carboxylic end group. The most prominent features in the FTIR spectra are the features between 2800 and 3100 cm^{-1} , between 1300 and 1600 cm^{-1} and around 1100 cm^{-1} (see Figure 2.2).

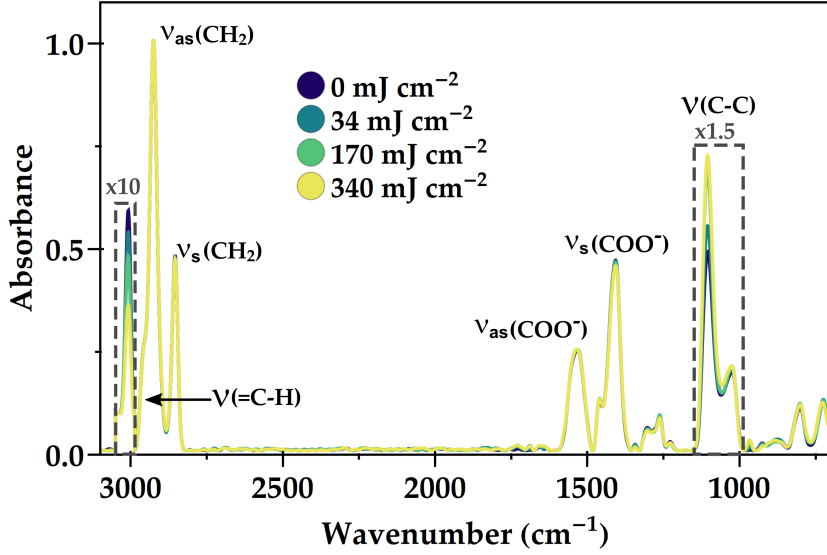


Figure 2.2: FTIR spectra of EUV exposed PbS CQD films. Vibrational features are indicated. Parts of the spectra in the dashed boxes are magnified for clarity. The C-H stretching around the double bond decreases and the C-C stretching increases after exposure, indicating cross-linking of the carbon chains. The carboxylic anchoring group is unaffected. Spectra are normalized with respect to the CH₂ stretches.

The absence of an absorption peak around 1700 cm^{-1} indicates the absence of protonated -COOH end groups, which would reveal the presence of unreacted excess of oleic acid in the sample before exposure, or the formation of free ligands upon exposure. The peaks between 1300 and 1600 cm^{-1} are related to the symmetric and asymmetric stretching modes of deprotonated carboxylate COO^- as bound to inorganic nanoparticles and quantum dots [85–87]. The absorption between $1300 - 1700\text{ cm}^{-1}$ does not change as function of dose, and we therefore conclude that the binding of the ligands to the crystal surface remains unaffected, which is important for maintaining a passivated CQD surface. The high wavenumber region, around 2925 cm^{-1} , corresponds to stretching modes of CH_2 (2850 cm^{-1}), CH_3 (2950 cm^{-1}) [87, 88] and the CH bending of the C=CH bonds (3005 cm^{-1}) [89]. We observe a systematic decrease and broadening of the peak at 3005 cm^{-1} , which corresponds to a reduction in the number of double bonds when higher doses of EUV are interacting with the sample. The often used, but generally weak

feature for C=C around $1650\text{-}1640\text{ cm}^{-1}$ was on the level of the noise and therefore not used in this analysis. C=C features below 1000 cm^{-1} were difficult to separate from -CH modes that are present due to different possible configurations of the oleic acid molecule, as well as influenced by the background signal of the silicon substrates and therefore not used. Finally, we observe an increase in the peak around 1105 cm^{-1} , commonly attributed to C-C-H stretching in metal oleate molecules [88]. An increase in this peak upon exposure can be rationalized by formation of new C-C-H bonds. Taken together, these changes demonstrate the cross-linking of the ligands at the position of the double bond in the carboxylic acid molecule. The cross-linking then turns the nanocrystal film into an insoluble, interlinked solid. Presumably, to form a coupled network, only a small number of cross-links per quantum dot are necessary to switch the solubility. The peak at 3005 cm^{-1} does not disappear even at the highest dose, meaning that many ligands remain unchanged.

Further evidence of such cross-linking was found by measuring the height profile of an EUV exposed PbS film with atomic force microscopy (AFM) mapping shown in Figure 2.3. The film shows virtually no reduction in thickness at the edge of an exposed area before development. This result is consistent with the observation that only a fraction of the ligands cross-link the CQDs and rules out major loss of ligands by outgassing. The phase map in the AFM, however, shows a high contrast between exposed and unexposed areas. The shift of phase angle from 3° to 25° can be correlated to a change in the visco-elastic properties of the material, where higher phase-shifts are related to a stiffer material due to stronger repulsion of the AFM tip, even though this change is difficult to quantify [90]. A stiffer material is consistent with cross-links of the organic ligands into a denser network.

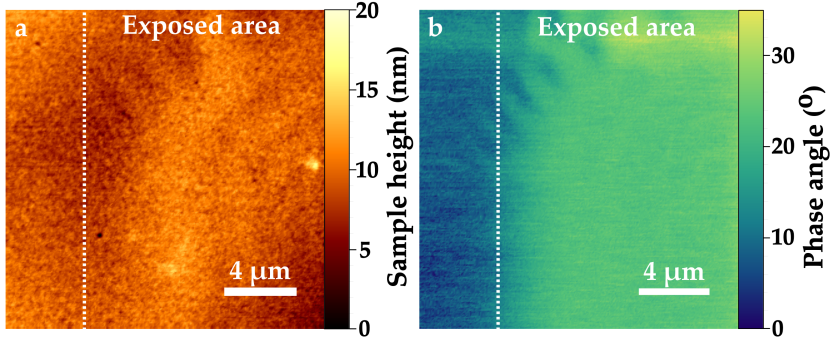


Figure 2.3: AFM height map (a) and phase map (b) of an undeveloped film of PbS quantum dots. The side right of the the dashed line has been exposed to a 340 mJ cm^{-2} dose of EUV. While the height map does not show a significant height difference between exposed and unexposed areas, the phase map shows a clear increase in the phase angle, which is consistent with an increased Young's modulus.

In order to determine the optimal dose for writing nanostructures with EUV, we write the PbS pillars at a range of intensities and measured their topology with AFM (Figure 2.4). We find that even at low exposures ($40 \pm 6 \text{ mJ cm}^{-2}$) we obtain the regular pattern after development, yet very thin. The features are on the order of $5 - 10 \text{ nm}$ high. Presumably, the low number of photons only cross-links a fraction of the particles, slowing down the dissolution rate [91]. When increasing the dose, the features become thicker and more clearly resolved, with sharper contrast between lines and spaces and a more reproducible shape. At $80 - 120 \pm 15 \text{ mJ cm}^{-2}$ we find well-resolved features and the thickness saturates at 40 nm , which is as thick as the original film. We find that the maximum film thickness needs to be on the same order as the desired feature size, as the maximum aspect ratio (height/width) of features is a little over 1. The relatively low dose required to write structures with EUV is particularly desirable because in commercial applications, which require an even lower dose of $20 - 30 \text{ mJ cm}^{-2}$, the EUV photons are produced from tin-droplet plasma, which is expensive. At higher doses the features remain easily distinguishable, but the feature size keeps increasing with dose, indicating overexposure. Overexposure emerges when the number of photons necessary for a solubility switch is surpassed outside of the intended region. As the features are written with interference lithography, the light

pattern consists of sinusoidal intensity patterns with a certain slope between minima and maxima. This leads to broadening of the written features when the dose is increased beyond the intensity threshold, as explained in more detail in chapter 1.

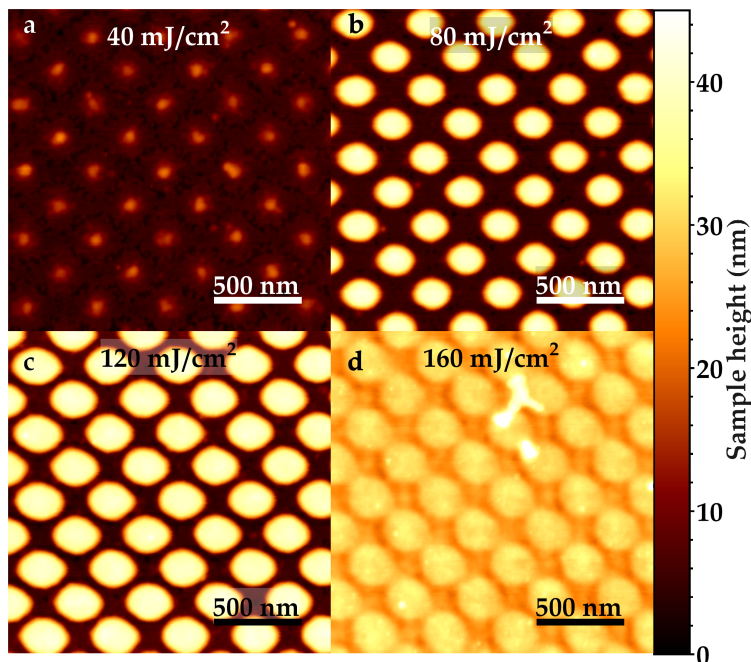


Figure 2.4: AFM image of PbS pillars exposed to different doses of EUV light. (a) Low doses lead to thin features remaining after development, (b, c) with good feature size and contrast between $80 - 120 \pm 15 \text{ mJ cm}^{-2}$. (d) At very high doses the feature dimension increases due to overexposure.

Since the onset of cross-linking was hard to define by AFM because of the absence of a sharp edge, PL measurements were performed on EUV-exposed CdSe films as an accurate probe suitable for very thin films (Figure 2.5a,b). An appreciable PL is detected for doses as low as 19.7 mJ cm^{-2} , consistent with detectable contrast in optical microscopy images which can be found in appendix 2.5. The PL intensity increases with increasing dose, as a thicker film of CQDs remains on the substrate. This increase in PL plateaus at doses over 280 mJ cm^{-2} , which roughly correlates with D100 (Figure 2.5b and Figure 2.9 in the appendix). EUV doses higher than 280 mJ cm^{-2} do lead to a small decrease in PL intensity, but the error bars also increase due to variations

of PL within the film.

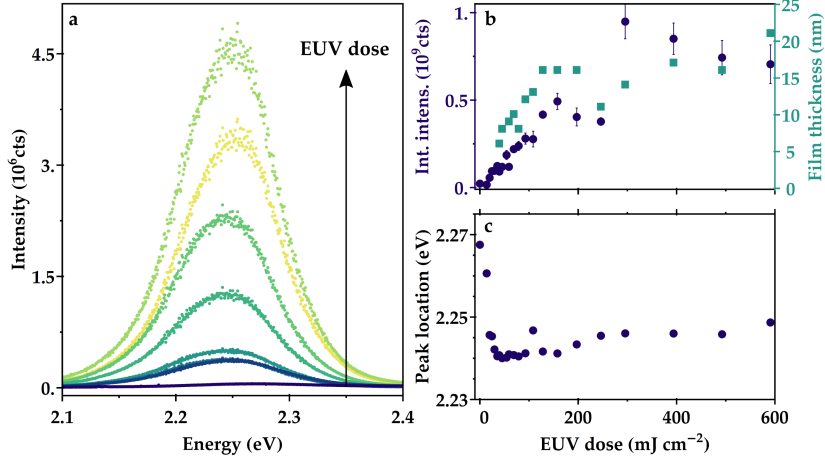


Figure 2.5: (a) PL spectra of CdSe films after exposure with EUV and development. The integrated PL intensity as function of EUV (b) shows an increase in PL intensity as function of the exposure dose, which is related to the increased thickness of the remaining quantum dot film. Error bars indicate spread between multiple measurements on the same sample. (c) Position of peak fluorescence of CdSe films after exposure to EUV and development. Exposure leads to an initial red-shift, followed by a small blue-shift.

We fit the PL curves with a Gaussian profile to extract both the peak location (Figure 2.5c) and FWHM as a function of the dose (shown in the appendix, Figure 2.10). We observe an initial red-shift, followed by a small blue-shift in the emission energy as dose increases. The initial red-shift occurs in the dose range where cross-linking starts. Cross-linking of the CQD ligands may reduce the interparticle spacing. This reduction enhances the energy transfer between the nanocrystals via the Förster resonant energy transfer (FRET) that favors emission from lower-bandgap quantum dots [92–95]. As the efficiency of energy transfer is strongly dependent of the distance between the two dipoles, small differences in interparticle distance in the order of several Å can already lead to such small red-shifts in the spectrum of PL [96]. The reduction in interparticle spacing also increases the electronic coupling between dots, reducing the quantum confinement [92–95, 97, 98]. We attribute the blue-shift at higher doses to a slight etching of the quantum dot surface by the

high dose of highly energetic electrons. This removal of only a few surface atoms reduces the size of the CQD core, leading to an effectively smaller crystal with more confinement, while not necessarily changing the radiative lifetimes [99]. The blue-shift we observe (10 - 20 meV) corresponds to less than 0.1 nm reduction in CQD radius [100]. Another explanation for the blue-shift could be related to a change in the electronic environment, which is mainly a function of the ligands. A change in the electronic environment would require either (i) ligand removal, (ii) a change in the binding of the ligands to the surface or (iii) a change in their chemistry. FTIR indicates that the intensity of CH_2/CH_3 as well as the binding group remain unaffected, excluding (i) and (ii). Cross-linking could indeed form a larger barrier for the electronic wavefunction, and hence leading to a blue-shift. However, this change would be counter intuitive as cross-linking should reduce the (average) chain length leading to a red-shift instead.

The PL intensity scales with the film thickness (Figure 2.12), which is an indication that the PLQY is relatively independent of dose. The PLQY is the ratio of radiative decay rate to the total decay rate (radiative + non-radiative decay). The non-radiative decay is mainly mediated by trap states due to imperfect surface passivation or changes in the electronic environment of the surface [24, 101]. This surface passivation arises from ligands binding to the surface. One would thus assume that a change to the ligand shell may affect the PLQY. Even a small fraction of ligand release would induce a large density of traps. Milder changes such as cross-linking may also change the PLQY, for instance because the refractive index of the ligands will change slightly. Also, cross-linking by aggregation of nanocrystal cores should red-shift the emission strongly due to an effective growth of the crystal and reduction of the confinement [102]. The stability of the signal from the binding group we found earlier in FTIR is consistent with minimal changes to the ligand anchoring on the quantum dot surface.

PL lifetime measurements are an accurate way of quantifying changes in non-radiative recombination [103]. We recorded lifetime traces of CdSe CQD films exposed to different doses of EUV exposed samples are shown in Figure 2.6a. Although de-

decay traces of quantum dots in solution or single quantum dots commonly exhibit a single exponential decay, multi-exponential decay behavior is often found in solid-state ensembles of quantum dots [104–106]. Similar to previous work we observe a bi-exponential decay consisting of one stretched exponential term: $y(t) = A_1 e^{-\left(\frac{t}{\tau_1}\right)^\beta} + A_2 e^{-\frac{t}{\tau_2}}$ [107]. Figure 2.6b shows the different lifetime components for EUV exposure as function of the exposure dose. We can observe a small initial decrease in lifetime for both τ_1 and τ_2 , which is consistent with the enhanced interparticle energy transfer described above. Above 200 mJ cm^{-2} we observe a slow increase in τ_1 with increasing dose. The stretched exponential exponent β , shown in the appendix, Figure 2.13, as function of dose, also appears to be stable at $\beta = 0.29 \pm 0.01$ for EUV exposure. We use these lifetime components to estimate a relative change in internal PLQY (see appendix, section 2.5), and find that upon EUV exposure PLQY_{int} drops by 20 - 50%. It should be noted however, that this analysis assumes no changes in outcoupling, which could affect the results. Although a small decrease in PLQY is observed, we would argue that the exposure is relatively mild to the CQD cores and these issues are likely mitigated by growing shells or using a repassivation step.

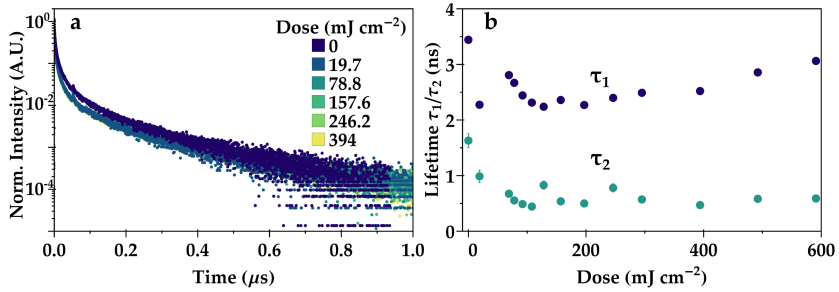


Figure 2.6: (a) PL lifetime traces of EUV exposed CdSe films after development. (b) Fitted lifetime components of the EUV exposed films as function of dose. Radiative lifetimes become shorter after exposure, but are remarkably stable after the initial decrease.

EUV photons are very energetic in comparison to the visible spectrum. In order to investigate the minimum energy required to give rise to the chemical changes inducing a solubility switch, we exposed the quantum dot layers to less energetic radiation, in the form of deep-ultraviolet (DUV) light ($\lambda = 365 \text{ nm}$, 3.4 eV,

and $\lambda = 225$ nm, 5.5 eV). Using lower-energy photons by DUV exposure is also possible. Previously Wang et al. already showed that deep-UV or blue light ($\lambda = 254, 365, 405, 450$ nm, 4.9, 3.4, 3.06, 2.75 eV) can be used for patterning CQDs covered with photoactive ligands, as these molecules are unstable and degrade under exposure and their destruction leads to colloidal instability of the CQDs [77, 78]. As the mechanism of the solubility switch is different in our case (cross-linking), it is not obvious whether DUV is energetic enough to induce this change. Exposure to 365 nm from a Suss MA6 mask aligner was unsuccessful. The intended pattern would not remain on the substrate, indicating that no chemical conversion was achieved. More energetic $\lambda = 225$ nm (5.5 eV) DUV light from a Nd:YAG-laser (NT342B, Ekspla) did induce a solubility switch, however only at very high doses of 4000 mJ cm^{-2} (see appendix, Figure 2.15), which is two orders of magnitude higher than for EUV photons. Photons with energies below the ionization energy promote only resonant electronic transitions. Therefore, if the relaxation process of these bound states does not lead to any bond cleavage, no chemical reaction can occur. It seems that as long as a minimum energy threshold of around 5.5 eV for photons is reached, as-prepared quantum dots can still be cross-linked to pattern them at micron- and nanoscale. We can see however, that the higher energy of the EUV photons allows for a more efficient cross-linking, possibly due to the fact that one absorbed EUV photon can create multiple reactive species that may cross-link more CQDs simultaneously, requiring less photons for full conversion.

2.3 CONCLUSIONS

We demonstrate a general one-step nanopatterning technique for as-synthesized PbS and CdSe quantum dots with advanced photolithography. Both relatively low-energy photons (from 5.5 eV) can be used for patterning, as well as higher-energy EUV photons (91.9 eV). Features can be as small as 60 nm which roughly corresponds to about 10 CQDs in diameter. We find that the solubility change is achieved by cross-linking the organic ligands, to create a cohesive quantum dot film. Required doses

are relatively low and, in the order of commercial state-of-the-art patterning materials ($\sim 120 \text{ mJ cm}^{-2}$) for EUV. Optimizing ligand chemistry might improve the sensitivity even further. The exposure to extreme-UV photons, even to relatively high doses, does not significantly affect the luminescent properties. The versatility and simplicity of the technique allows for intricate designs at both nano- and micron scale. This simple, universal patterning technique can open a route to numerous applications with active semiconductors patterned on the nanoscale.

2.4 EXPERIMENTAL METHODS

Chemicals: Lead oxide (PbO, 99.995%), selenium (Se, 99.999% pure), n-octane (>98%) were purchased from Alfa Aesar. Hexane (anhydrous) and toluene (anhydrous) were purchased from VWR. Bis(trimethylsilyl)sulphide (TMS) (>98%), cadmium oxide (CdO, 99.99%), 1-octadecene (ODE) (technical grade 90%), oleic acid (OA) (technical grade 90%), acetone (ACE) (analytical grade), isopropanol (IPA) (analytical grade), methanol (MeOH) (analytical grade), sulfuric acid (H_2SO_4 , 97.5%) and hydrogen peroxide (H_2O_2 , 30%) were purchased from Sigma Aldrich. Double-side polished silicon wafers were purchased from Sievert Wafer.

Nanocrystal synthesis: PbS nanocrystals were synthesized following Barkhouse et al. [108]. In a typical synthesis of PbS quantum dots, 0.45 g of PbO was added to 1.51 mL of OA to 18 mL of ODE into a three-neck flask. The solution was degassed at 100°C for 3 hours under vacuum. All the powder dissolves, resulting in a clear solution. A second precursor was prepared by adding 0.213 mL of TMS to 10 mL of ODE. The lead precursor was heated to 120°C . When the temperature was stable, the sulphur precursor was injected quickly and PbS quantum dots nucleate, resulting in a black solution. The reaction was quenched after about 30 seconds by injecting 20 mL of cold hexane and removing the flask from the heat, resulting in crystals of about 2 nm in size. After cooling to room temperature, the nanocrystals were washed three times by precipitation in ACE (first wash) and IPA (second, third wash), followed by centrifugation, discarding of the supernatant and redispersion in toluene. Finally the quantum dots were stored in octane at the desired concentration.

Synthesis of the CdSe quantum dots was done similar to Čapek et al. [109]. First, a selenium precursor was prepared of 0.1 M elemental selenium in ODE inside a three-neck flask. In order to accelerate the dissolution, the solution was heated to 180 °C for 5 hours, yielding a clear, orange solution while hot and a clear, deep-golden colored solution upon cooling. A cadmium precursor was made by adding 0.0942 g of CdO, 2.272 mL of OA and 24 mL of ODE in a three-neck flask. The solution was degassed for 1 hour at 100 °C under N₂. The temperature was raised to 260 °C and the CdO fully dissolved to yield a clear, colorless solution. 7.2 mL of Se-ODE was injected into the solution, causing the temperature to drop to 230 °C. The reaction was left ongoing for 5 minutes at this temperature before quenching the reaction by placing the flask in ice water. In the initial washing step, a mixture of toluene, and a 1:1 MeOH:IPA solvent mixture was used to precipitate the nanocrystals. Upon redispersion in toluene, MeOH:IPA solvent mixture was used two more times wash the solution. The final dispersion of the nanocrystals was in octane or toluene at the desired concentration.

Film preparation: Samples for EUV exposure were made by spin coating thin films of quantum dots onto clean silicon substrates. The substrates were cleaned by subsequent ultrasonic cleaning in soap water, de-ionized (DI) water, ACE and IPA. After sonication the substrates were cleaned 30 mins in acid piranha solution (7:3 vol H₂SO₄:H₂O₂) and finally 15 mins ozone plasma. Quantum dot solutions with a concentration between 10 and 35 mg mL⁻¹ were filtered (0.2 micron polytetrafluoroethylene (PTFE) filter) and spin coated at 2500 rpm for 20 seconds, resulting in films with a thickness of around 20-100 nm.

EUV exposure and development: The films were exposed to 92 eV light from the Swiss Light Source synchrotron at the Paul Scherrer Institute. Transmissive diffractive gratings were used as masks to create interfering beams, leading to periodic patterns on the wafer-level, ranging from line patterns (M716 mask) and contact hole patterns (M73 mask) to open frame patterning large areas (0.5 × 0.5 mm²) through a pinhole. With the M73 mask, the error on the tool factor is larger, resulting in an error in the reported doses of 10 – 15%. After exposure the samples were developed in toluene, hexane or octane for 10 seconds, followed

by a dip in clean toluene and subsequently in IPA, before drying with N_2 . Open frame samples were subsequently characterized by AFM, FTIR, PL microscopy, and TCSPC. Patterned samples were analyzed by SEM and AFM.

(Deep)-UV exposure: Two different sources of exposure were used for (deep-)UV exposure. Exposure at (365 nm, 3.4 eV) was performed on a Suss MA/BA6 mask aligner with a 1000W Hg lamp as exposure source. Samples were exposed through a contact mask in hard contact mode at a 100 μm gap. Various exposures were made at 25 mW cm^{-2} for total doses up to 10,000 mJ cm^{-2} .

As second UV exposure source a deep-UV laser was used, in the form of a tunable Ekspla NT342. A NL300 pump laser with second and third harmonic generators (SHG, THG) producing 355 nm light pumps, a parametric oscillator with SHG to generate of 5 ns 225 nm (5.5 eV) light pulses at a repetition rate of 10 Hz. Laser power of 5.0 mW with a spot size radius of 2 mm was used. Samples were exposed directly to the laser spot, to obtain circular exposure spots with doses up to 4000 mJ cm^{-2} .

Scanning Electron Microscope: Scanning Electron Microscope images were taken by a FEI Verios 460 at voltages between 5 and 10 kV at 100 pA.

Atomic Force Microscopy: AFM images were taken on a Veeco Dimension 3100 (Bruker) and a Dimension Icon (Bruker) in tapping mode. The images were scanned at a linescan frequency of 1 Hz.

Photoluminescence: PL of samples was measured using a WITec alpha300 SR confocal microscope with 100 \times Zeiss objective (NA 0.9). A 405 nm Thorlabs S1FC405 fiber coupled laser diode was used as excitation source. A 405 nm notch filter was used to remove the laser light in the detection path which was coupled to the detector. Light is collected in reflection on a UHTC 300 VIS WITec spectrometer. The PL spectra were converted to the energy scale using a Jacobian transformation [110]. The setup can be used to record single spectra as well as perform spatial PL mapping.

Photoluminescence lifetime measurements: Fluorescence lifetimes were recorded with a home-built time correlated single photon counting (TCSPC) setup (PicoQuant PDL 828 “Sepia II”

and a PicoQuant HydraHarp 400 multichannel) in an inverted microscope with an Olympus 60 \times Plan Apochromat water immersion objective. The samples were excited by a 485 nm laser (PicoQuant LDH-D-C-485), which was pulsed at a repetition rate of 0.5 MHz. The excitation laser signal was blocked in the detection path by a Thorlabs FEL-500 long-pass filter in combination with a 488-NF notch filter.

Fourier Transform Infrared Spectroscopy: FTIR samples were spin-coated on double side polished silicon substrates with a thickness of 500 μm . Spectra were recorded in transmission with a Bruker Vertex 80v under vacuum conditions. Each spectrum is an average of 20 spectra with a resolution of 4 cm^{-1} .

Optical microscope: Optical microscope images were recorded with a Zeiss, AxioCam ICc 5 equipped with a 20 \times /0.2 objective.

2.5 APPENDIX

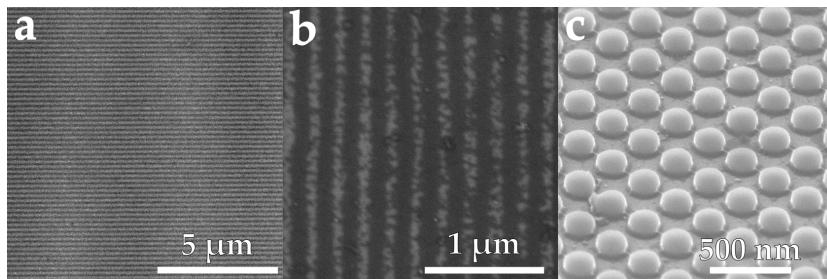
EUV patterned QD films

Figure 2.7: More examples of patterned quantum dot films. (a,b) Lines of PbS quantum dots patterned with EUV, 160 mJ cm^{-2} . (c) PbS quantum dot pillars patterned with EUV, dose 90 mJ cm^{-2} . Development is not complete and some scumming is visible between the pillars. These bridges are in the order of 8 nm.

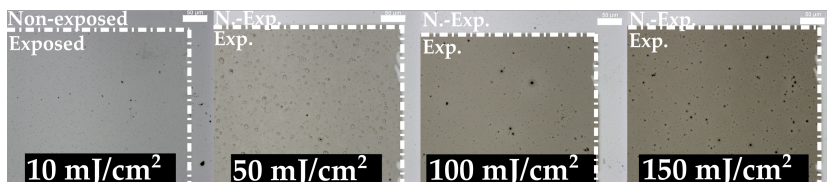
Optical microscope images of contrast fields

Figure 2.8: Optical microscope images of EUV exposure fields of CdSe films after development. From doses as low as 10 mJ cm^{-2} light contrast can be observed between the exposed and unexposed areas. With increasing dose, the film thickness and with that the visible contrast increases.

Contrast curves

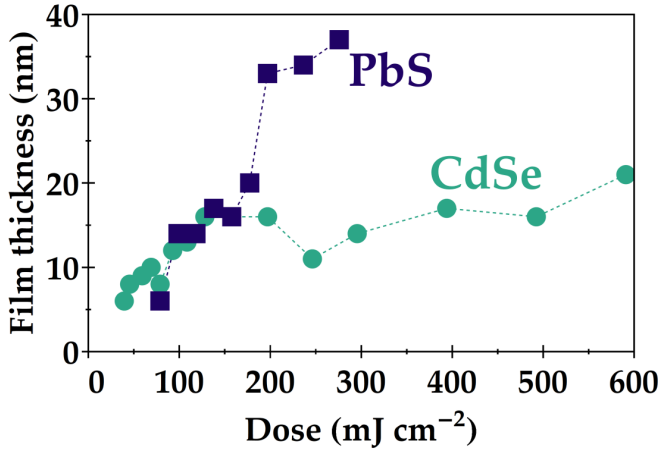


Figure 2.9: Remaining film thickness of EUV exposed films after development as function of dose. CdSe films start to remain on the substrate at doses as low as 20 mJ cm⁻² (D_0). The remaining film thickness saturates at around 120 - 150 mJ cm⁻² (D_{100}). Distinct PbS films start to remain on the substrate at doses of around 70 mJ cm⁻² (D_0). At doses around 200 - 250 cm⁻² the whole film thickness remains (D_0)

Full width at half-maximum as function of signal-to-noise ratio

The PL spectra of exposed and developed CdSe films were first normalized and then fitted with a Gaussian profile (Equation 2.1) in Mathematica.

$$y(x) = \frac{A}{\sqrt{2\pi\sigma^2}} e^{-\frac{(x-\mu)^2}{2\sigma^2}} + \text{b.g.} \quad (2.1)$$

The normalized spectra can be found in Figure 2.10a. Besides the initial red-shift of the spectra mentioned in the main text (Chapter 2), changes in the spectra are subtle. We do, however, observe a slight narrowing of the linewidth with increasing dose, which is also observed when fitting the spectra, as shown in Figure 2.10b.

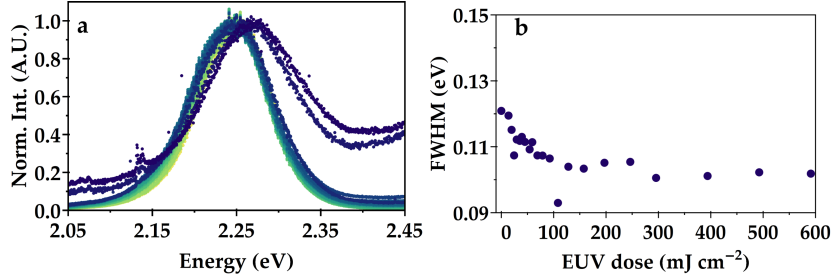


Figure 2.10: (a) Normalized PL spectra of EUV exposed and developed CdSe films. Lighter colors indicate higher doses. Besides an initial redshift, differences between the spectra are very subtle. (b) The FWHM of the PL spectra as fitted for EUV and exposed and developed CdSe films. There is an apparent narrowing of the linewidth with increasing dose.

The FWHM in the EUV exposed samples decreases as a function of dose, yet the EUV exposed samples plateau at around 80 mJ cm^{-2} . Energy transfer leads to a narrowing in the PL linewidth [92], however, we attribute the effect of this apparent narrowing to different signal-to-noise ratio (SNR) ratio of the PL measurements. As mentioned in Chapter 2 and shown in Figure 2.5, because lower doses only cross-link part of the film, the fluorescence signal is relatively weak and has hence a low SNR. When fitting the PL curves, this signal-to-noise level leads to larger fitted peak widths. Figure 2.11 shows this effect. We artificially generated Gaussian spectra with random noise of the same amplitude for all spectra. We fixed the peak centers (2.25 eV) and FWHM (0.12 eV), but varied the height of the spectra, thereby varying the SNR. Subsequently we fitted these spectra with the same fitting routine as used for the fitting of our measured spectra. Figure 2.11a-f show the simulated spectra with the Gaussian fit in red. It is clear that for increasing SNR the fit starts to appear to be more narrow as the base of the curve is not influenced as much by the noise level. Figure 2.11g shows the fitted FWHM value as function of the SNR as well as the actual FWHM used to simulate the spectra. For low SNR the FWHM is grossly overestimated, but when the signal improves, the fit converges on the actual value in a fashion that broadly resembles an inverse square root dependence. At an SNR of 10 the fitted value is still around 9% too high indicating that higher SNR is preferred. Figure 2.11h shows a similar trend in the fitted FWHM of the measured spectra. When plotted against

the measured intensity, the FWHM seems to follow the same inverse square root dependence as the simulated spectra. We therefore conclude that the observed change in FWHM cannot give us significant information on the physical properties of the nanocrystals.

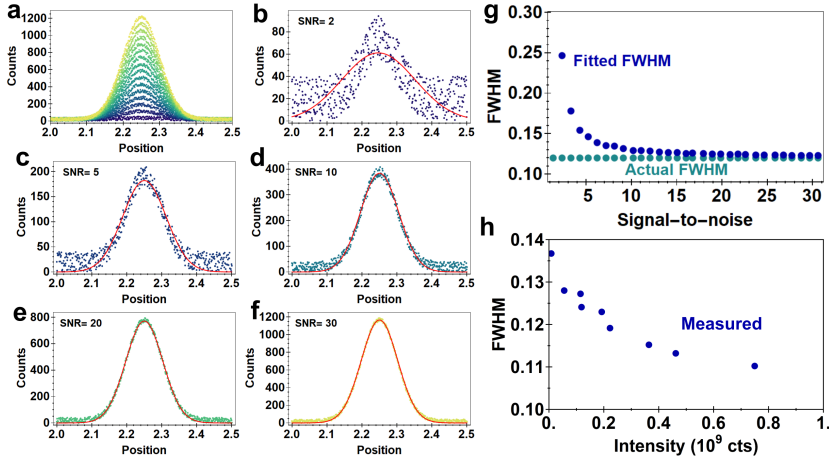


Figure 2.11: The effect of signal-to-noise on FWHM. (a) Simulated PL spectra with different SNR but fixed peak center and FWHM. (b-f) Show different spectra with varying SNR from 2 to 30. The red lines indicate the fit. (g) Shows the fitted FWHM as function of the SNR. Errorbars are within every plot point. It is clear that the fitted FWHM depends on the SNR and that the fit converges onto the correct value only when the signal is good enough. (h) The fitted FWHM of the measured CdSe PL spectra as function of the integrated intensity. The trend in FWHM is similar as for increased SNR in (g).

QD film thickness/PL intensity relation

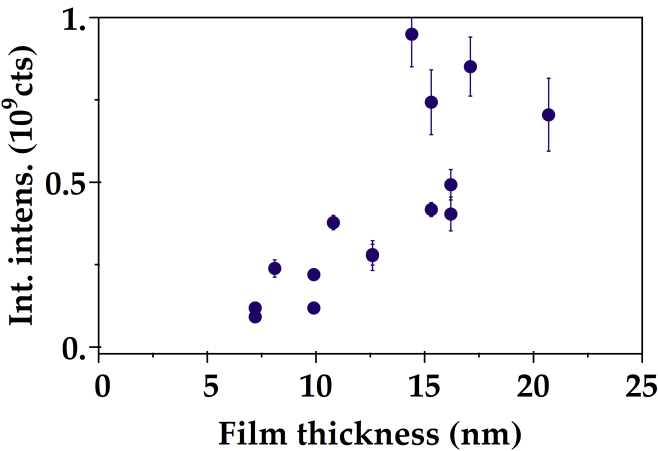


Figure 2.12: PL intensity as function of film thickness of EUV exposed and developed CdSe films.

Stretched exponentials of fitted lifetime curves of EUV exposed CdSe films

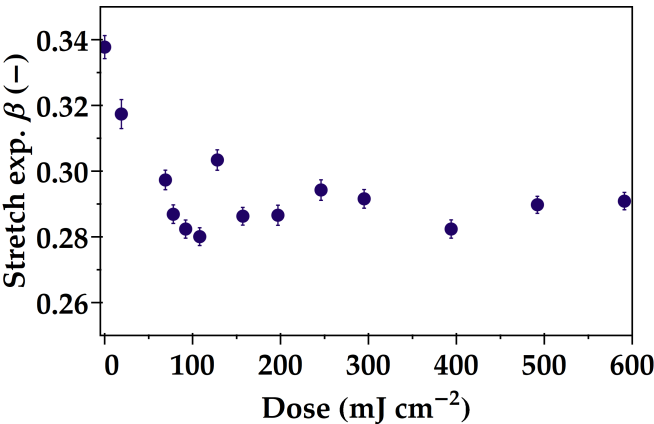


Figure 2.13: Fitted values of the stretched exponential exponent β of EUV exposed CdSe films.

Estimation of internal photoluminescence quantum yield of EUV exposed CdSe films.

We estimate the relative change of PLQY from the internal PLQY, by dividing the rate of emission, by the sum of all rates (Equation 2.2).

$$PLQY_{int} = \frac{k_{rad}}{k_{total}} \approx \frac{k_{rad}}{k_{rad} + k_{non-rad}} \quad (2.2)$$

This estimate assumes that there are no changes in outcoupling. As we can fit our lifetime data with two exponential terms, with two lifetimes, we can also determine two rates: $k_1 = \frac{1}{\tau_1}$ and $k_2 = \frac{1}{\tau_2}$. We can determine the relative change in PLQY by calculating the ratio of $\frac{k_{rad}}{k_{total}}$. We assume here that τ_1 , the long lifetime component is the radiative component and τ_2 , the short time component is the non-radiative component, as the radiative lifetimes of CdSe are dominated by slower time components [111, 112]. By calculating this measure for PLQY of the sample before exposure and normalizing all the other PLQY values to this value, we can estimate the relative change in PLQY. We can observe that the PLQY decreases after EUV exposure by 20 - 50%.

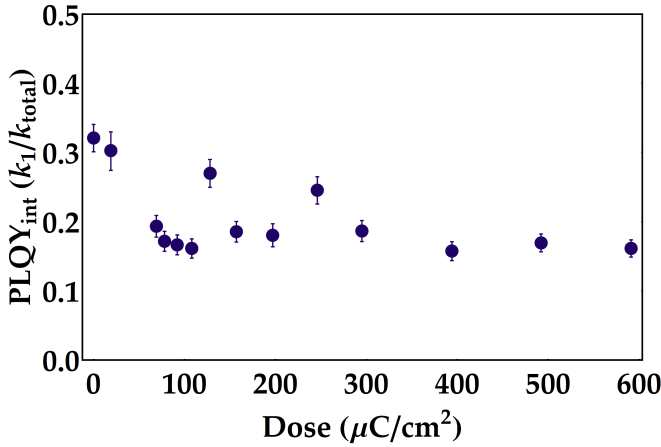


Figure 2.14: Estimated internal PLQY of EUV exposed CdSe films.

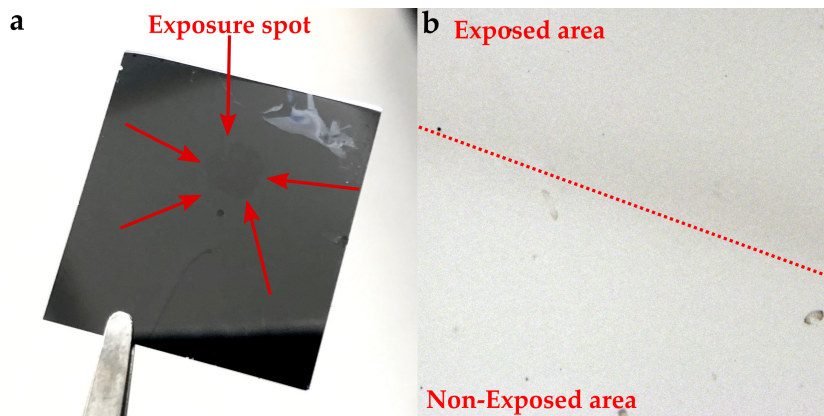
Deep-UV exposed sample

Figure 2.15: CdSe film exposed to 225 nm DUV and developed in toluene. (a) Silicon substrate (19×19 mm) was exposed to 4000 mJ cm^{-2} of a 225 nm laser. After development the exposure spot (4 mm diameter) is visible on the substrate, although the remaining film is very thin. (b) Optical microscope close up of part of the edge of the exposure spot. Contrast between exposed and unexposed areas is faint, but visible.

COLLOIDAL QUANTUM DOT PATTERNING VIA ELECTRON-BEAM LITHOGRAPHY

"With every mistake, we must surely be learning."

— George Harrison, *While My Guitar Gently Weeps*
(1968)

Parts of this chapter have been published in:

Dieleman, C. D., Ding, W., Wu, L., Thakur, N., Bespalov, I., Daiber, B., Ekinci, Y., Castellanos, S. & Ehrler, B. "Universal direct patterning of colloidal quantum dots by (extreme) ultraviolet and electron beam lithography", *Nanoscale* **2020** 12(20), 11306-11316

3.1 INTRODUCTION

Photolithography is not the only form of lithography used for the manufacturing of (semiconductor) devices. Electron-beam lithography EBL is a reliable platform for patterning materials beyond the diffraction limit. As mentioned in chapter 1, the wavelength of an electron depends on its momentum and therefore the acceleration voltage. Nevertheless, the wavelength of the electrons in a e-beam lithography system is on the order of picometers (10^{-12} m), which is 5 orders of magnitude smaller than visible light and still 4 orders of magnitude smaller than extreme-ultraviolet (EUV). This allows electron beams to write smaller features in a single step as compared to the systems that use photolithography, where multistep lithography and advanced optics with high NA is necessary to reach sub-wavelength feature sizes.

A second benefit of e-beam lithography is the absence of masks in the process, as the electron beam can be turned on and off while the sample moves underneath. This gives an enormous flexibility in the exposure pattern, as every possible design can be "pixelated" and transferred into the resist. This flexibility comes at the cost of exposure time however, as the fact that only a single spot is exposed means that the total exposure time for a complicated image is longer than with photolithography where a whole wafer can be exposed at once. Nonetheless, due to its precision EBL has found an important place in nanofabrication for writing sub-10 nm features, lab-scale prototyping and experiments, as well as photomask fabrication. The e-beam directly induces the chemical changes in the resist material, similarly leading to a solubility contrast between exposed and unexposed areas.

High-energy electron beams have previously also been used to pattern colloidal nanoparticles. Reetz et al. [113] and Bedson [114] explored direct patterning of metallic nanoparticles with e-beam. More recently for semiconductor nanocrystals were directly patterned with e-beam (30 keV, 100 keV) [75, 79] and other more energetic sources summarized in an overview by Palazon et al. [115]. In this chapter we discuss the general, one-step, direct patterning of colloidal quantum dots with either low- or high-energy electron beams (3 eV – 50 keV). Similar to the previous

chapter we find that the quantum dot ligands cross-link upon exposure, therefore allowing selective redispersion of unexposed nanoparticles, while preserving the luminescent properties. Due to the precision and versatility of the e-beam, single features can be made sub-100 nm, while very intricate luminescent designs are possible.

3.2 RESULTS AND DISCUSSION

Similar to the previous chapter, we synthesized two types of colloidal quantum dots (CQDs) from CdSe and PbS. Although we obtained the best results with CdSe, which is what we show here, the technique works for both materials. The ligands used are still the same 18-carbon mono-unsaturated oleic acid. The patterning works similar to the process described in chapter 2 and shown in Figure 2.1a. Spin coated thin layers of CQDs on silicon were directly exposed to three different exposure sources in the form of electron beams with either low energy electrons (0 - 70 eV) in a low-energy electron microscope (LEEM, SPECS P90) with a fixed beam spot, depending on its aperture, or high-energy electrons (50 kV) in a commercial EBL system (Raith Voyager) that allowed for exposures of a wide variety of designs. The samples were developed by dipping the samples into toluene or hexane for 10 seconds.

As with EUV exposure, the electron beam irradiation induces chemical reactions in the materials. As the incoming electrons of commercial e-beam systems like the one used in this work have a high energy (50 kV), these electrons have a similar effect as high-energy photons discussed in the previous chapter: ionization and generation of an electron cascade that can lead to reactions like bond cleavage [55, 82] as well as cross-linking, when radicals interact with double bonds [83, 84]. Next to the photoelectrons created by ionization of the resist molecules, secondary electrons emitted from the substrate also play a role, as the mean free path of electrons from a high-energy keV electron beam is longer (10 s of nm) than that of photo-electrons emitted after EUV photon absorption, which is expected to be in the 1 nm range [55].

Figure 3.1 shows some typical structures created by e-beam lithography. More examples can be found in appendix 3.5. In this case we use a 50 keV electron beam ($100 \mu\text{C cm}^{-2}$), which leads to a large number secondary electrons with a broad energy distribution. As in the case of EUV exposure discussed in chapter 2, we find that the e-beam exposed areas remain on the substrate upon development. The structures are well-resolved, rendering the smallest structures down to around 65 nm, which corresponds to a diameter of 10 quantum dots clustering together. From these observations, one can conclude that it is possible to pattern these materials well below the diffraction limit of deep-ultraviolet lithography (DUVL) in a one-step e-beam exposure.

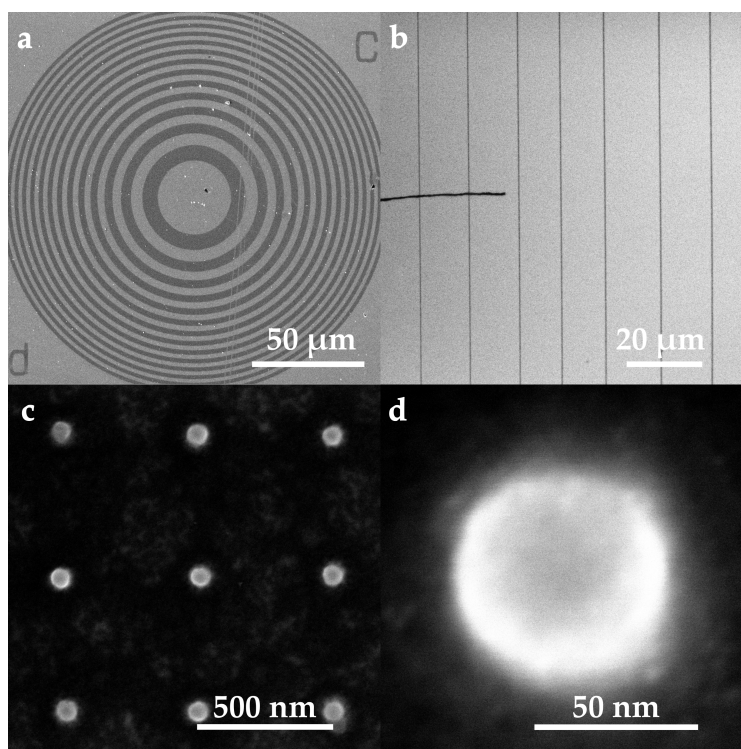


Figure 3.1: SEM images of e-beam patterned CQDs. (a) Larger, circular structure of CdSe CQDs written with e-beam lithography ($100 \mu\text{C cm}^{-2}$). (b) Thin (100 nm) lines of CdSe written with e-beam ($100 \mu\text{C cm}^{-2}$). (c) Array of pillars of CdSe quantum dots with 500 nm spacing written with a $100 \mu\text{C cm}^{-2}$ e-beam dose. (d) Close-up of one of the pillars. The diameter is around 65 nm.

Figure 3.2 shows an atomic force microscopy (AFM) height map of a patterned array of CdSe CQD columns. The columns are spaced 1 micron apart and are very well resolved. The height and shape are very consistent and can reach a thickness of over 100 nm. This is only a small part out of a larger field of columns, meaning that the resulting structure is constant over large micron sized areas. Next to these very regular structures, EBL also allows for more intricate structures. These type of individual "building blocks" can also form more difficult overall structures as shown further in this chapter.

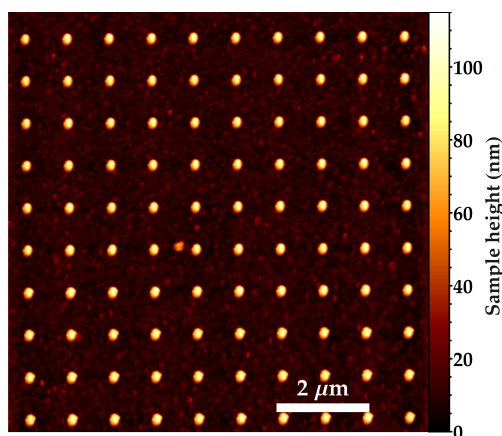


Figure 3.2: AFM height map of exposed and developed CdSe CQD film. The pattern of CQD columns is well resolved, with features of about 100 nm height. The pattern is uniform and extends over a large area.

Similar to extreme-ultraviolet (EUV) exposed films, e-beam exposed and developed films of varying dose were investigated for their photoluminescence (PL) behaviour. Figure 3.3a,b shows the observed PL as function of exposure dose. We observe an increase in PL as function of exposure dose, which is allocated to the increasing film thickness at higher doses. Weak PL can be observed at exposure doses as low as $20 \mu\text{C cm}^{-2}$, indicating that even very small e-beam doses can already cross-link a few CQDs. Higher doses crosslink a larger part of the film, hence increasing the PL. In the investigated dose range, with a maximum of $300 \mu\text{C cm}^{-2}$ no plateau in the PL is reached, indicating that the full film is not yet cross-linked. At high doses one might expect beam damage affecting the emission intensity, for instance due to

removal of ligands which would reduce surface passivation, but for the dose range tested we do not observe a decrease in intensity. As the film thickness continues to increase, the PL intensity also increases, even at doses $>200 \mu\text{C cm}^{-2}$ which is on the high end of the tested exposure doses.

Similar to the EUV samples, we do observe a larger variation in the PL intensity at higher doses and thicker films, likely due to the increased chance of anisotropy in a thicker film. After a Gaussian fit of the PL curve we extract the peak location of the PL as function of exposure dose (Figure 3.3c). The energy of the peak emission slightly red-shifts upon small e-beam doses, very similar to the red-shift observed in the EUV exposed CQDs in chapter 2. With similar reasoning we allocate this red-shift to the cross-linking itself and possible subsequent changes in intraparticle distance, thereby enhancing Förster resonant energy transfer (FRET) [92–95]. The subsequent blue-shift that was observed with EUV exposed CQDs seems to be less pronounced after the e-beam exposure at higher doses, which could be explained by the fact that as mentioned before, we seem not yet to be in the regime of complete cross-linking. Removal of some surface atoms could nonetheless explain the small blue-shift we do observe. The fitted full-width at half-maximum (FWHM) is becoming smaller as well, as can be found in appendix 3.5, and is likely related to the change in SNR, as explained in appendix 2.5.

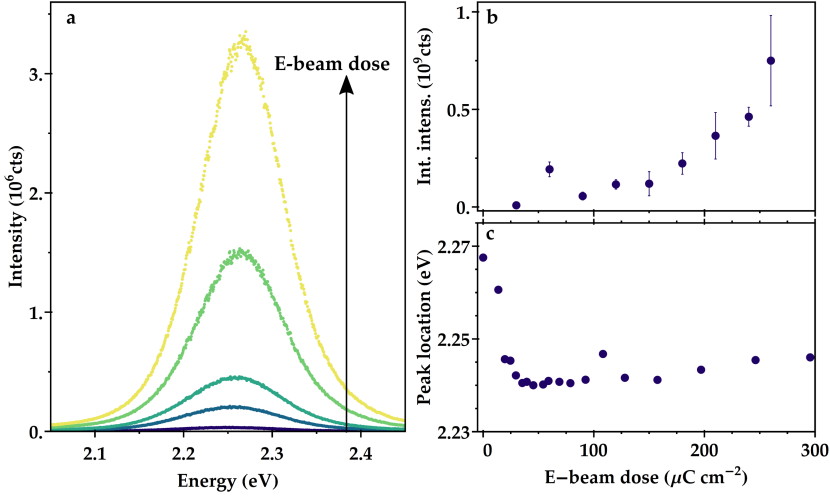


Figure 3.3: (a) Photoluminescence spectra of CdSe films after exposure with e-beam and development. (b) The integrated PL intensity as function of e-beam dose shows an increase in PL intensity as function of the exposure dose, which is related to the increased thickness of the remaining quantum dot film. Error bars indicate spread between multiple measurements on the same sample. (c) Position of peak fluorescence of CdSe films after exposure to e-beam and development. Exposure leads to an initial redshift, followed by a small blue-shift.

PL lifetime traces (Figure 3.4a) do not reveal a clear trend in changes of the PL lifetime. We observe multi-exponential decay that is fitted with a stretched exponential: $y(t) = A_1 e^{-\left(\frac{t}{\tau_1}\right)^\beta} + A_2 e^{-\frac{t}{\tau_2}}$ [107]. We find that lifetimes are relatively stable upon exposure (lifetimes $\tau_1 = 4.0 \pm 0.25$ ns, $\tau_2 = 1.7 \pm 0.5$ ns, Figure 3.4b), although it seems that exposure to e-beam leads to a slight decrease in the decay lifetime. The stretched exponential exponent β , shown in appendix Figure 2.13, as function of dose, also appears to be stable at $\beta = 0.36 \pm 0.018$ for e-beam exposure. If we use these lifetime components again to estimate a relative change in internal photoluminescence quantum yield (PLQY) (see appendix 3.5), it seems that e-beam exposure yields a relative increase in PLQY_{int} . It is likely that our assumption about the absence of changes in outcoupling plays a role in this observed increase. We think however that the exposure is at these doses is not affecting the quantum dots enough to disqualify this technique for optical applications.

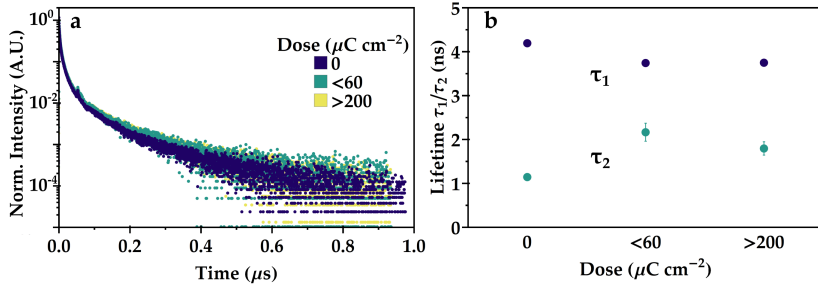


Figure 3.4: PL lifetime traces of (a) e-beam exposed CdSe films after development. (b) Fitted lifetime components of the e-beam exposed films as function of dose. There is no clear trend in the lifetimes, but radiative lifetime τ_1 becomes slightly shorter after exposure. Errorbars indicate the error of the fit.

As EBL electrons are very energetic and as we have observed in the previous chapter that lower energy light (5.5 eV) can already lead to cross-linking, we exposed the CQD layers to low-energy electrons (LEE, 0 - 70 eV) in order to investigate whether we observe a minimum threshold for electron energy to induce chemical changes. Figure 3.5 shows the average height of a developed CdSe film as function of dose and electron energy, based on AFM measurements (appendix 3.5). We can already observe changes to the material at electron energies as low as 3 eV. Increasing the dose does not seem to have a significant influence on the changes in the material as these doses are high enough to insolubilize the whole film. At these low energies higher doses are necessary for cross-linking than in the case of 50 keV electrons, indicating that the cross-linking process may be less efficient at lower energies. Nonetheless there is a difference between the minimum energy required by incident photons (5.5 eV, chapter 2) as compared to incident electrons (3 eV). This difference shows that the energy threshold for converting the material is different for photons and electrons, presumably because the way they induce chemical reactions is different. Low-energy photons, that do not induce ionization promote only resonant electronic transitions, which may induce chemical reactions if the relaxation of these states leads to bond cleavage. Electrons on the other hand can also generate radicals which may allow chemical changes at lower energy. Despite this, the fact that both electrons and photons lead to chemical changes shows that the patterning mechanism presented in these first chapters is versatile and universal. As

long as a minimum energy threshold is reached, 3 eV for electrons and 5.5 eV for photons, as-prepared quantum dots can be cross-linked to pattern them at micron- and nanoscale.

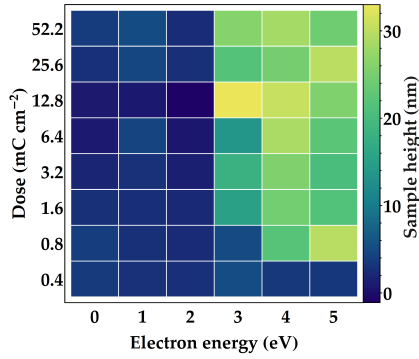


Figure 3.5: Thickness of CdSe films after exposure to low-energy electrons (LEEs) and development. Depending on the dose, 3 eV electrons can already lead to a solubility switch of the CQD film.

Finally, we demonstrate the versatility and the intricate patterns possible by directly patterning as synthesized CdSe quantum dots into a miniature version of the painting “The Girl with the Pearl Earring” by Johannes Vermeer (Figure 3.6a). This image was first pixelated, and the gray value was translated into the filling fraction of the individual pixel, which was then used for e-beam exposure. Figure 3.6b shows that also this complex developed structure shows bright PL, demonstrating the feasibility of directly patterning active semiconductor quantum dots for complex optoelectronic devices. Next to this we believe it should be possible to pattern monolayers or double layers of CQDs, for instance by crosslinking the ligands to functionalizing molecules on the substrate. Here it will be key to make use of this functionalization to create selective adhesion of the CQDs to the substrate.

3.3 CONCLUSIONS

We show a general one-step nanopatterning technique for as-synthesized CdSe quantum dots with direct e-beam lithography. Low-energy electrons (from 3 eV) can already be used to induce insolubility reactions to pattern CQDs. Highly energetic electrons

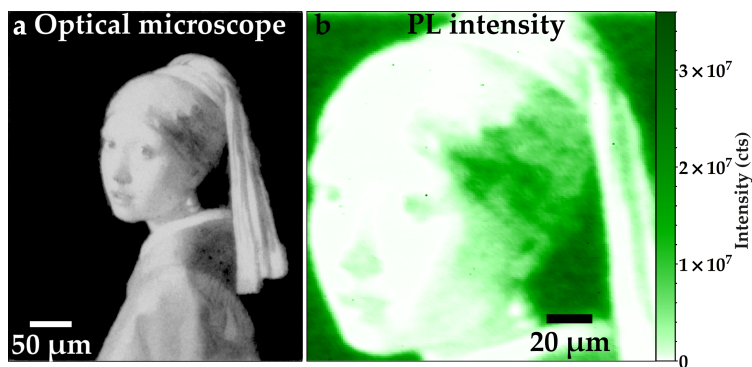


Figure 3.6: (a) Optical microscope image of “The Girl with the Pearl Earring” (Johannes Vermeer, Mauritshuis Den Haag, NL) patterned in CdSe quantum dots with e-beam. (b) Fluorescence map of the remaining CdSe quantum dot film. Excitation wavelength $\lambda = 405$ nm, detected emission $\lambda = 545$ nm. Note that the colorscale is reversed, as the luminescence of the CQDs yields a negative image.

(50 keV) from commercial EBL systems allow for patterning as well. Features can be as small as 60 nm which roughly corresponds to about 10-15 CQDs in diameter. Low doses in the order of several hundred $\mu\text{C cm}^{-2}$ are sufficient to induce the patterning mechanism, in the order of commercial state-of-the-art e-beam patterning materials. Optimizing ligand chemistry might improve this sensitivity even further. The luminescent properties seem to be relatively unaffected by the exposure, even at higher doses. The versatility and simplicity of the technique allows for intricate designs at both nano- and micron scale. This simple, universal patterning technique can open a route to numerous applications with active semiconductors patterned on the nanoscale.

3.4 EXPERIMENTAL METHODS

Chemicals and synthesis: Used chemicals and synthesis methods are similar to the methods described in chapter 2.

Film preparation: Samples for EUV exposure were made by spin coating thin films of quantum dots onto clean silicon substrates. The substrates were cleaned by subsequent ultrasonic cleaning in soap water, DI water, ACE and IPA. After sonication the substrates were cleaned 30 mins in acid piranha solution (7:3 vol

H₂SO₄:H₂O₂) and finally 15 mins ozone plasma. Quantum dot solutions with a concentration between 10 and 35 mg/mL were filtered (0.2 micron PTFE filter) and spin coated at 2500 rpm for 20 seconds, resulting in films with a thickness of around 20 - 100 nm.

High-energy e-beam exposure: E-beam exposure was done in a Raith Voyager commercial e-beam lithography system with a voltage of 50 kV, LC30 column mode with 0.135 nA beam current. Films were developed in toluene immediately after exposure.

Low-energy electron exposure: Experiments on exposing the quantum dot samples to low-energy electrons were performed in Leiden University using the ESCHER low-energy electron microscope (LEEM) experimental setup. The design of the setup is based on a commercial aberration-corrected LEEM SPECS P90 instrument. Exposure to electrons of well-controlled energy and dose was performed using a LEEM built-in beam blanking system. For each single exposure event the sample was exposed to electrons of known energy. The electron energy value was constant during each exposure event. After finishing the exposure the electron beam was blanked and the sample stage was moved to a new unexposed position. As the result a 2D array of exposed oval-shaped areas was created. Within the array the x-axis corresponds to a change of dose at constant electrons energy while the y-axis corresponds to changes of energy at constant dose. After the exposure, the sample was developed in toluene and resulting pattern was analyzed using AFM.

Scanning Electron Microscope: Scanning Electron Microscope images were taken by a FEI Verios 460 at voltages between 5 and 10 kV at 100 pA.

Atomic Force Microscopy: AFM images were taken on a Veeco Dimension 3100 (Bruker) and a Dimension Icon (Bruker) in tapping mode in tapping mode, at a linescan frequency of 1 Hz.

Photoluminescence: PL of samples was measured using a WITec alpha300 SR confocal microscope with 100× Zeiss objective (NA 0.9). A 405 nm Thorlabs S1FC405 fiber coupled laser diode was used as excitation source. A 405 nm notch filter was used to remove the laser light in the detection path which was coupled to the detector. Light is collected in reflection on a UHTC 300 VIS WITec spectrometer. The PL spectra were converted to the

energy scale using a Jacobian transformation [110]. The setup can be used to record single spectra as well as to perform spatial PL mapping.

Photoluminescence lifetime measurements: Fluorescence lifetimes were recorded with a home-built TCSPC setup (PicoQuant PDL 828 “Sepia II” and a PicoQuant HydraHarp 400 multichannel) in an inverted microscope with an Olympus 60 \times Plan Apochromat water immersion objective. The samples were excited by a 485 nm laser (PicoQuant LDH-D-C-485) , which was pulsed at a repetition rate of 0.5 MHz. The excitation laser signal was blocked in the detection path by a Thorlabs FEL-500 long-pass filter in combination with a 488-NF notch filter.

Optical microscope: Optical microscope images were recorded with a Zeiss AxioCam ICc 5 equipped with a 20 \times /0.2 objective.

3.5 APPENDIX

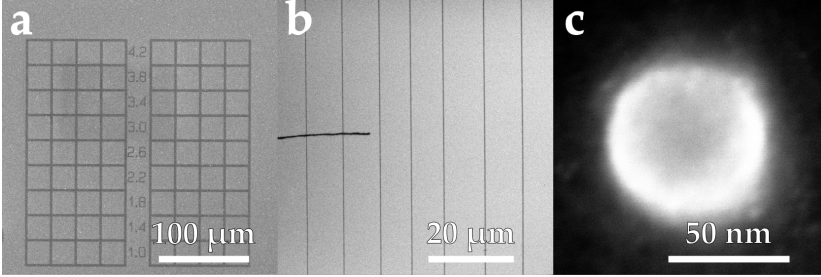
E-beam patterned QD films

Figure 3.7: More examples of patterned quantum dot films. (a) Micron sized straight lines and letters of CdSe. (b) Sub-100 nm curved lines of CdSe CQDs patterned by e-beam lithography, dose $100 \mu\text{C cm}^{-2}$. (c) Single pillar of CdSe CQDs patterned by e-beam, dose $100 \mu\text{C cm}^{-2}$. All samples are developed with toluene.

FWHM as function of SNR

The PL spectra of exposed and developed CdSe films were first normalized and then fitted with a Gaussian profile (Equation 2.1) in Mathematica in order to obtain peak location and FWHM, as described in appendix 2.5. Figure 3.8a shows the normalized spectra of e-beam exposed and developed CdSe films. As is the case with the EUV exposed samples, we observe a small narrowing of the linewidth with increasing dose, that becomes clear when isolating the FWHM in Figure 3.8b. The effect is small, however, and is most likely related to the SNR, as explained in appendix 2.5.

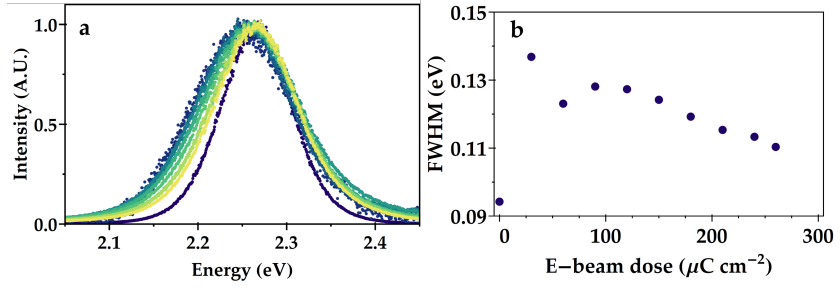


Figure 3.8: (a) Normalized PL spectra of e-beam exposed and developed CdSe films. Lighter colors indicate higher doses. Besides an initial redshift, differences between the spectra are very subtle. (b) The FWHM of the PL spectra as fitted for e-beam and exposed and developed CdSe films. There is an apparent narrowing of the linewidth with increasing dose.

Stretched exponentials of fitted lifetime curves of e-beam exposed CdSe films

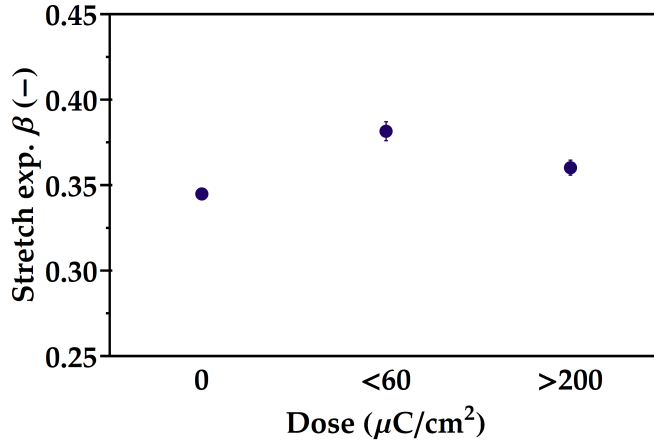


Figure 3.9: Fitted values of the stretched exponential exponent β of e-beam exposed CdSe films.

Estimation of internal PLQY of e-beam exposed CdSe films

We estimate the relative change of PLQY from the internal PLQY, similar to the method described in appendix 2.5, by dividing the rate of emission by the sum of all rates (Equation 2.2). We

observe a small increase in PLQY, but it should be noted that this method assumes no changes in outcoupling of light.

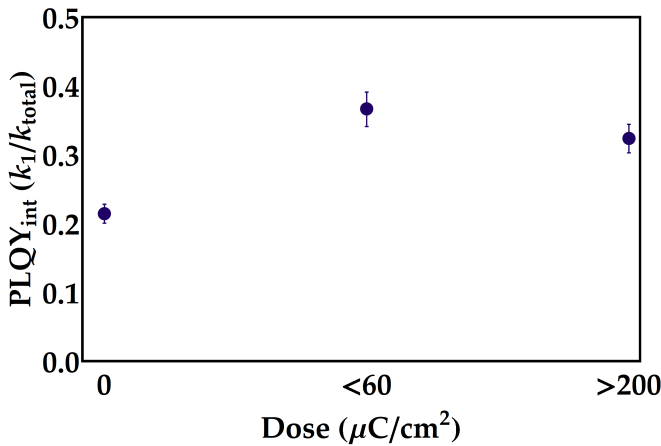


Figure 3.10: Estimated internal PLQY of e-beam exposed CdSe films.

Low Energy Electron exposed CdSe film

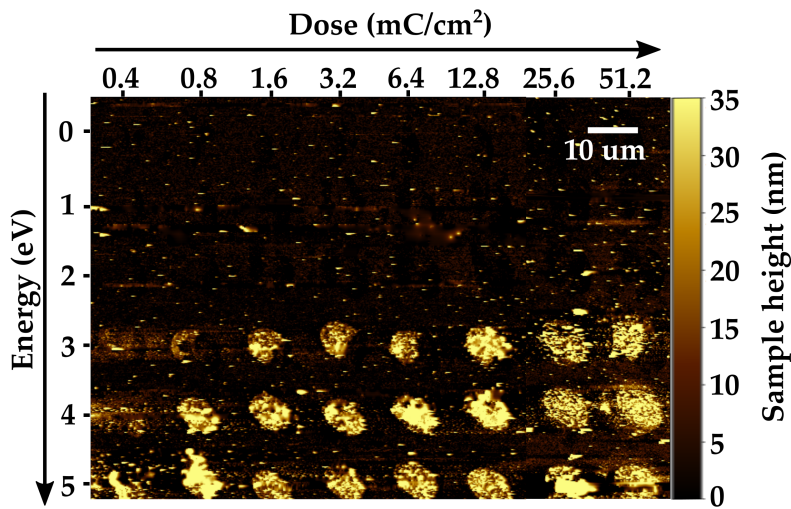


Figure 3.11: AFM image of dose test of CdSe quantum dots, exposed to low-energy electrons of different energy and at different dose. 3 eV electrons can already convert the material into an insoluble film.

DIRECT PATTERNING OF CSPBBR₃ NANOCRYSTALS VIA ELECTRON-BEAM LITHOGRAPHY

"The further one travels the less one knows. The less one really knows. "

— George Harrison, *The Inner Light* (1968)

Parts of this chapter are based on:

Dieleman, C. D., van der Burgt, J., Garnett, E.C. & Ehrler, B. "Direct patterning of CsPbBr₃ nanocrystals with electron-beam lithography" (in preparation)

4.1 INTRODUCTION

Perovskite nanocrystals (NCs) have proven themselves as an interesting materials platform for a diverse range of applications. Their simple colloidal synthesis allows for cheap solution processing and the system is easily tunable. Other semiconductor colloidal quantum dots (CQDs), like II-VI systems, are most commonly tuned by the quantum confinement effects arising from their small size [20, 21] and to a lesser extent by their composition, as it requires precise alloying [116, 117]. The bandgap of perovskite NCs, however, can be readily manipulated via compositional changes, most easily by halide exchange [37]. Mixture of the halides allows for gradual bandgap adjustments [37, 118]. Moreover, many different precursors and elements form the perovskite crystal structure, allowing easy substitution of elements and a wide library of possibilities in adapting the material to have desired properties, for instance with methylammonium-based [119], formamidinium-based [120] or lead-free tin-based perovskites [121]. Organic ligands, that passivate the surface of the crystals and provide colloidal stability, can also influence the electronic environment of the nanocrystals and alter the shape during synthesis. This allows perovskite NCs to be suitable for many applications including photovoltaics [2, 46], photodetectors [122, 123], scintillators [124, 125] and light-emitting diodes (LEDs) [5, 44, 45]. Next to this, perovskites have shown to be efficient emitters, exhibiting long charge carrier lifetimes and defect resistance. Patterning active materials like these is a useful way to expand their tunability as it may allow more intricate designs that can improve efficiencies or expand the functionality. In previous work we showed a method to pattern CQD directly by extreme-ultraviolet lithography (EUVL) or electron-beam lithography (EBL) without affecting their luminescent properties significantly. In this work we show this method can also be applied to perovskite nanocrystals, to create perovskite patterns down to 100s of nanometers that still show luminescence.

Most of the works on patterning perovskite NCs do not make use of direct lithography. Some approaches include self-assembly [126], laser assisted deposition [127, 128], ink-jet printing [129] or multi-step lithography [130, 131]. Previous work on patterning

perovskites via lithography has been carried out by Palazon et al. who showed that exposure of perovskite nanocrystals to an X-ray photoelectron spectroscopy (XPS) source could impede ion exchange in the crystals and reduce their solubility [76]. It is, however, not obvious that direct patterning with lithographic techniques is straight-forward. Although perovskites are often described as "defect resistant" due to the mobile nature of ions in the crystal, the material also has stability issues, induced by exposure to oxygen, water or even long exposure to light [132]. In scanning electron microscopes (SEMs) it is also observed that perovskite can be destroyed under the electron beam. Even though the damage in SEM imaging is induced by the high dose from repetitive scanning across the probe, the highly energetic (but lower dose) electron beam used in e-beam lithography could also lead to damages of the perovskite NCs, rather than induce local chemical changes that are necessary for direct patterning as observed in our previous chapters.

Here we synthesize CsPbBr_3 NCs, spin-coat them into thin films and expose them directly to an electron beam in a commercial lithography machine. Upon exposure and subsequent development of the films in various solvents we can create well-defined perovskite structures on the substrate. Feature sizes can be as small as 100s of nanometers. We find that the chemical changes in the ligands are due to a cross-linking reaction as well as partial detachment of the ligands that creates a less soluble assembly of nanocrystals. As the required doses are still relatively high, we do find some damage to the material in terms of a reduced photoluminescence quantum yield (PLQY). The developed samples are, however, still luminescent and we believe that this technique is suitable for device fabrication, especially with more efficient cross-linking ligands or repassivation of the crystal surface after processing.

4.2 RESULTS AND DISCUSSION

We synthesize CsPbBr_3 nanocrystals by adapting the approach of Protesescu [37] and Lu [133], which combines the hot-injection of a Cs-oleate into a solution of PbBr_3 , oleylamine (OIAm) and oleic acid (OA) in 1-octadecene (ODE). After purification we are

left with cubic CsPbBr_3 NCs of around 15 nm in toluene. These crystals can be spin-coated onto silicon substrates to form thin layers of nanocrystals with a thickness up to 100 nm. A typical film of NCs as can be seen in Figure 4.1a. As can be seen in the image, the cubic particles arrange themselves into larger ordered structures. These films are then directly exposed to the electron beam of a commercial e-beam lithography machine (Raith Voyager). This machine operates at 50 keV and different beam currents can be used for exposing the perovskite films. In order to explore whether the approach we used in the previous chapter is also applicable to these perovskite NCs, we expose the films to doses between 100 and 10 000 $\mu\text{C cm}^{-2}$ in line patterns with a width of 50, 100, 200 and 500 nm as well as 1, 2 and 5 μm . After the exposure we develop the samples in a solvent mixture of chloroform and refrigerated tetrahydrofuran (THF), leading to remaining structures of perovskite NCs on the substrate where the electron beam has exposed the film. Some of these structures can be observed in Figure 4.1b-h. This behavior, where material becomes partially insoluble electron beam exposure is reminiscent of negative photoresists that are cross-linked by the electron beam. Unlike commercial photoresists, that are typically converted with doses in the order of 100s of $\mu\text{C cm}^{-2}$, the perovskite nanocrystals need a higher exposure dose of 2000 $\mu\text{C cm}^{-2}$ in order to obtain a clear structure. Figures 4.1b-e show examples of different line patterns formed by the e-beam patterning. One can observe lines of 1 μm , 500 nm, 200 nm, and 100 nm respectively. In all cases, the individual nanocrystals can be observed. Down to 500 nm the lines are very well defined, with remarkably straight edges. When scaling down further, small imperfections start to influence the line roughness to a greater extent. As the NCs we use are cubic, good stacking and self-assembly is beneficial for straight edges. Another factor playing a role in the line-edge roughness is the particle size distribution. Even though in general the NCs are of similar size and shape, larger particles tend to be harder to redissolve during the development process and can lead to less optimal particle assembly. This may disrupt the line edges as is visible in the thinner lines of 200 nm and 100 nm in Figures 4.1d-e.

A balance between underexposure and overexposure of the features exists. When underexposing, not enough material remains on the substrate to form the desired features, while overexposure causes features to blur and leads to more particles remaining on the substrate where not intended. Some examples of this can be found in Figure 4.7 in the appendix. The optimum doses are relatively high as compared to commercial resist materials and also as compared to our previous work with CdSe and PbS [134], in the order of $2000 \mu\text{C cm}^{-2}$. This may be related to the size difference of the crystals, used in this work, as compared to previous systems. As the nanocrystal size is growing, the surface-to-volume ratio reduces and if patterning is dependent on ligand interactions, the reduction of ligands to particle volume may be detrimental for the sensitivity.

Figure 4.1f shows the map of Amsterdam as a pixelated image. Individual pixels are $200 \text{ nm} \times 200 \text{ nm}$ with an overall image size of $150 \mu\text{m} \times 150 \mu\text{m}$, making this a map with scaling 1 : 23 million. In Figures 4.1g and h magnifications of the image can be seen in the form of a line of pixels touching at the corners and a single isolated pixel respectively. These examples clearly show a resolution of 200 nm and placement of these structures is accurate at the defined positions. In the single pixel one can also observe the individual NCs. Here, again the influence of the arrangement of the crystals can be observed as the crystals seem to be oriented in a 45° angle with respect to the sides of the square, leading to slightly truncated corners. Although not the focus of this work, it could be interesting to further optimize the stacking of nanocrystals in the future, to match the final shape of the desired features.

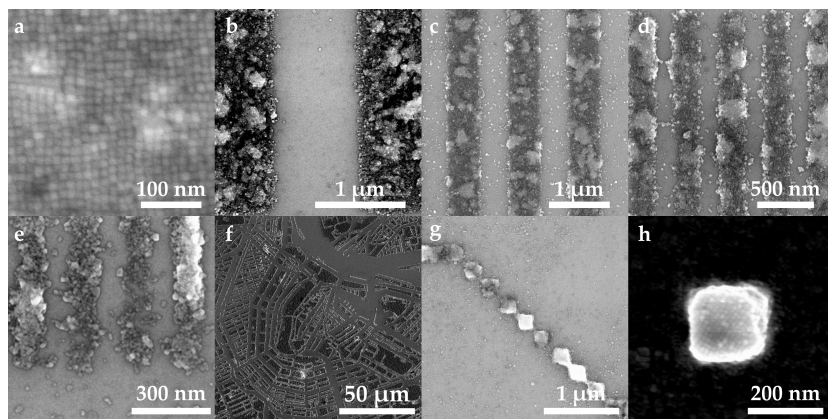


Figure 4.1: SEM images of unpatterned (a) and e-beam patterned (b-h) CsPbBr_3 nanocrystals at a dose of $2000 \mu\text{C cm}^{-2}$. (a) Shows the crystals after synthesis, spin-coated into thin films. (b-e) Show lines of NCS of $1 \mu\text{m}$, 500 nm , 200 nm and 100 nm , respectively. Thinner lines exhibit more apparent line-edge roughness as small variations in particle size have a larger effect on the relative smoothness of the line-edge of thinner lines. (f) A pixelated image of the map of Amsterdam consisting of $200 \text{ nm} \times 200 \text{ nm}$ pixels. (g-h) Detailed images of these pixels. These structures can be placed with high precision and touch in the corners. Good assembly of the NCS is beneficial for straight edges.

Figure 4.2 shows atomic force microscopy (AFM) images of the patterned nanocrystals. It is clear that good contrast of the patterns is achieved between the substrate and thick structures in the order of 100 nm . These thicknesses correspond to film thicknesses that are relevant for device fabrication.

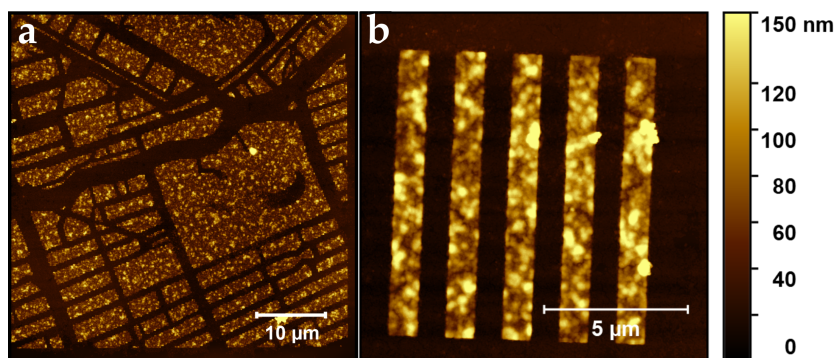


Figure 4.2: AFM images of patterned CsPbBr_3 nanocrystals, with a detail of the map of Amsterdam (a) and the $1 \mu\text{m}$ lines (b). There is good contrast between the intended structures and the substrate. The thickness is around 100 nm .

Patterning perovskite nanocrystals does not serve a function if their intrinsic functionality is lost. The photoluminescence (PL) should therefore remain after processing. We spatially map the PL with a confocal microscope system (*WITec alpha300 SR*) where the structures are excited with a 405 nm laser coupled into the objective. Figure 4.3a shows the PL spectrum of the CsPbBr_3 NCs. We observe the typical emission profile of CsPbBr_3 with peak emission around 2.42 eV or 513 nm, as observed by others [37, 133]. Figure 4.3 shows optical microscope and PL intensity maps side by side for e-beam patterned line patterns (b,c) and the Amsterdam map (d,e). The exposed and developed structures are still very brightly luminescent and show the same emission line shape as before exposure. The line patterns visible in the PL map have a width of 1 μm in the left column, 500 nm in the middle column and 200 nm in the most right column. 500 nm lines can be resolved by the microscope due to the high NA of the objective (0.9). The 200 nm lines cannot be spatially resolved, even though emission is detectable from this block of lines. The exposure doses in Figure 4.3 used for patterning are 2000 and 1000 $\mu\text{C cm}^{-2}$ for the 1 micron lines and 3000, 2000, 1600 and 1000 $\mu\text{C cm}^{-2}$ for the 500 nm lines from top to bottom, as shown in the figure. From the microscope images it seems that the lines in this region are more or less similarly resolved after patterning, but PL intensity appears slightly less bright for higher doses. For the 200 nm lines, which are written with the same exposure doses as the 500 nm lines, the story is slightly different. In this case, the lower dose of 1000 $\mu\text{C cm}^{-2}$ is not enough to form a thick structure and thus PL is not very bright. At least 1600 $\mu\text{C cm}^{-2}$ is necessary to resolve a clear structure, but both contrast and PL are higher at 2000 $\mu\text{C cm}^{-2}$. At higher doses, the PL seems to diminish again. This raises the question to what extent the patterning and exposure dose affects the photoluminescence quantum yield (PLQY), as the dose should be high enough to resolve the structures.

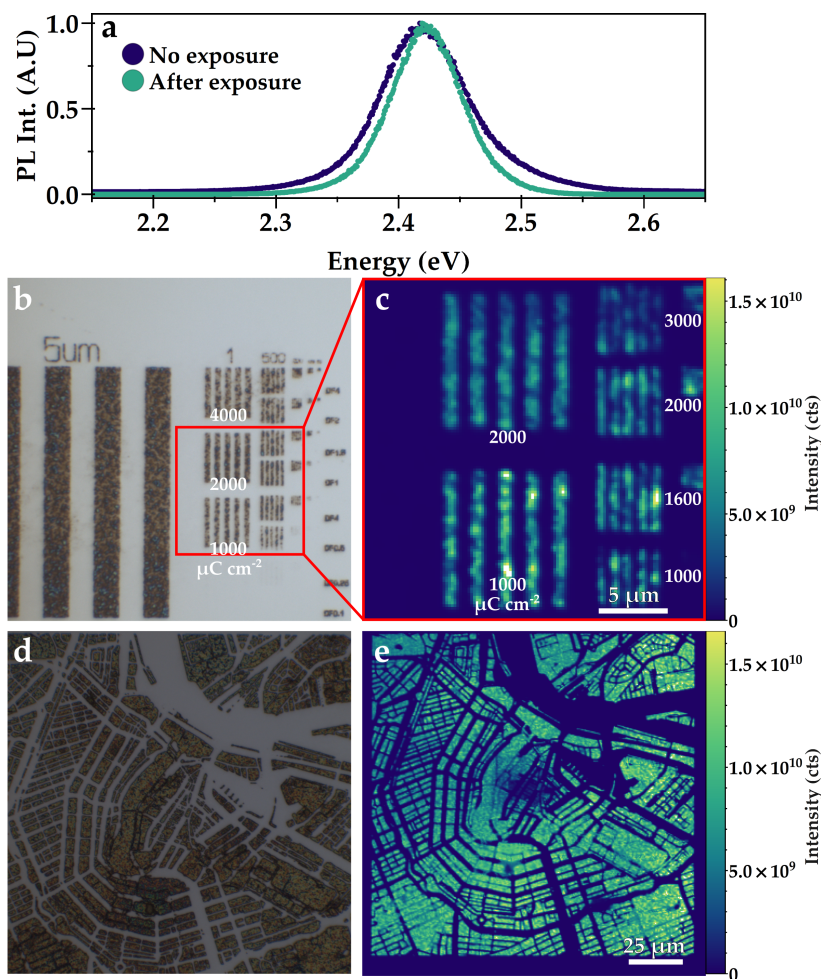


Figure 4.3: (a) Observed spectrum of patterned and unpatterned CsPbBr₃ nanocrystals. The spectra are very similar in shape and have a peak emission at 2.42 eV/ 513 nm. Optical microscope (b, d) and PL intensity maps (c,e) of patterned CsPbBr₃ NCs. Structures are excited with a 405 nm laser and PL around the peak emission of the perovskite is integrated. A dose of at least 1000 $\mu\text{C cm}^{-2}$ is needed for good contrast. Features down to 500 nm can be resolved. Doses over 2000 $\mu\text{C cm}^{-2}$ diminish the PL intensity. Exposure doses are in the image. The Amsterdam map is exposed at 2000 $\mu\text{C cm}^{-2}$.

In order to estimate the changes in PLQY we expose a film of CsPbBr₃ NCs to different e-beam doses without development and spatially map the absorbance as well as PL. Measuring absorbance properly requires a transparent substrate. As glass or quartz is not conductive, however, patterning a perovskite layer

on top of glass is not possible. It causes charging of the sample and drifting of the electron beam, which makes proper exposure impossible. Therefore, indium tin oxide (ITO)-coated glass substrates were used to allow for dissipation of charges under exposure. We expose the sample to different doses ranging from 200 to 10 000 $\mu\text{C cm}^{-2}$ (dose factor 0.1 - 5.0). Subsequently the absorbance at 405 nm, the same wavelength used for excitation of PL, of the exposed area was mapped in an integrating sphere setup [135]. Under the optical microscope it was already visible that exposure leads to changes in absorbance, as areas exposed to higher doses appear darker (see appendix, Figure 4.8). Figure 4.4a shows the absorbance map of exposure fields on an undeveloped CsPbBr_3 film. The dose factors need to be multiplied with 2000 $\mu\text{C cm}^{-2}$ in order to obtain the exposure dose. Figure 4.4b shows the measured absorbance as function of exposure dose for three different samples. The error bars indicate the standard deviation of the measured absorbance over the different pixels. We observe an increase of the absorbance from 0.126 ± 0.016 of the unexposed film to about 0.159 ± 0.011 at a dose factor of 1.0, after which the absorption seems to level off and only increases very slightly even when the exposure dose is 5 times higher. The observed trend is the same for all samples.

It is not immediately obvious why the absorption increases. One explanation could be an increased film thickness. In AFM, however, we do not observe any clear increase in film thickness as is evident from the thick remaining structures after development. Another explanation could be the outgassing of volatile organic compounds from the film, which might originate from breaking of the organic ligands. The relative increase in inorganic content of the film could give rise to absorption changes. In this case, however, one would expect a decrease in film thickness and a strong reduction in IR absorption of organic functional groups. As is shown in an upcoming section, this is not the case. A change in refractive index of the material is also a possibility, although we were not able to confirm.

Figure 4.4c shows a typical PL intensity map of one of the exposed samples. The intensity is normalized to the 95th percentile intensity value as some pixels were extremely bright. The mean values and spread of the PL in all the exposure fields can be found

Figure 4.4d. We observe a similar but opposite trend to the absorption: an initial fast decrease up to dose factor 1.0, from 0.704 ± 0.132 to 0.401 ± 0.069 , followed by a plateau and eventually further decrease. The exposure does therefore alter the material. Most of this change seems to happen up to $2000 \mu\text{C cm}^{-2}$, which coincides with the dose that yields well-defined features. Higher doses did not change the resolved features significantly, but it does seem to have a further effect on the PL properties. From the relative changes in absorbance, +26.1% and PL, -42.9%, one might estimate the PLQY does decrease quite significantly by a factor 2. This does, however, assume that the outcoupling is not changed in the exposed areas as the light is collected in an objective above the sample and the emission is not collected in every direction. A change in film roughness might, however, scatter more light into more shallow angles.

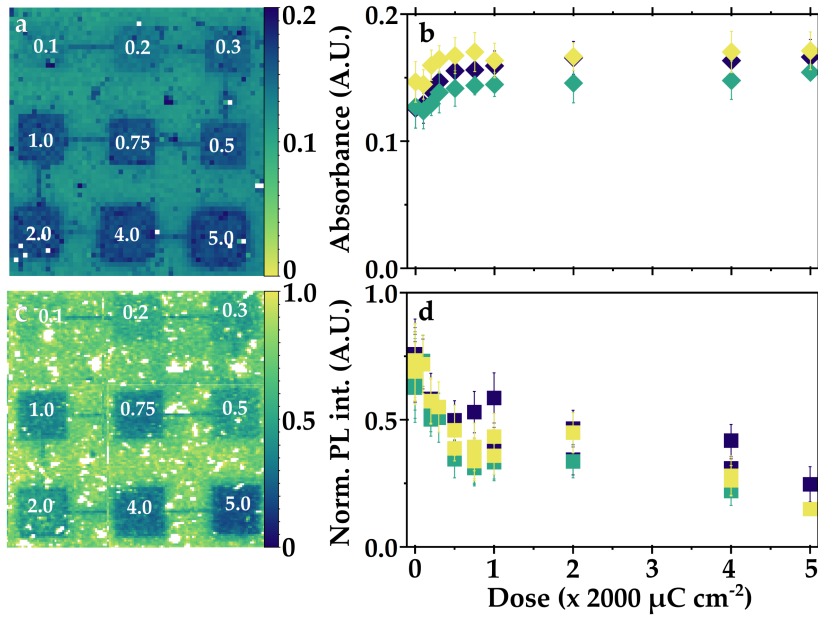


Figure 4.4: Absorbance and PL intensity of exposed but undeveloped CsPbBr₃ films. (a) Absorbance map of exposed NC film. White labels indicate the dose factor, which should be multiplied with $2000 \mu\text{C cm}^{-2}$. Individual exposure fields are $50 \mu\text{m} \times 50 \mu\text{m}$. (b) Absorbance as function of exposure dose of three different samples. (c) PL intensity map with the relative PL intensity per exposure dose. (d) Average PL intensity as function of exposure dose for three different samples.

We measure radiative lifetime to understand the changes we measured in PL intensity. We measure unexposed as well as patterned CsPbBr₃ films via time correlated single photon counting (TCSPC) with a pulsed 485 nm laser. We fit the decay curves with a two-exponential model, where the first term is a stretched exponential term (equation 4.1) in order to take into account the nature of nanocrystals [107, 134]. As they are an assembly of very small, single, isolated crystals, there is likely a distribution of radiative decay rates as these rates can slightly vary from crystal to crystal, more so than in a 3D bulk material. The stretch factor β is an indicator of how wide the distribution of rates is and can take a positive value below 1. A β of 1 indicates the limit where only one rate is present and we can ignore the stretched exponent.

$$I(t) = A_1 e^{\left(-\frac{t}{\tau_1}\right)^\beta} + A_2 e^{-\frac{t}{\tau_1}} + b.g. \quad (4.1)$$

where:

$I(t)$ = Number of PL counts at time t

A_n = Dimensionless prefactor for each exponential term

τ_n = Characteristic lifetime

β = Dimensionless stretched exponential factor

$b.g.$ = Background counts

The PL decay curves can be found in Figure 4.5. We fit the first 50 ns of lifetime decay and find two lifetime components, one around 1 ns and one around 4 ns. The fast decay component is constant over different doses, while the longer component has more spread. The observed spread is, however, also present from measuring different spots on the same sample. Fitted lifetime components of similar, unexposed samples can be found in appendix Figure 4.5. The stretched exponential β is stable around 0.75 (appendix Figure 4.10), which indicates a relatively small distribution of rates. Previously we assigned the faster component to be the radiative lifetime, while the longer component is related to non-radiative processes. From these data points, however, it is

not obvious that there is increase in the non-radiative processes as the longer lifetime component does not show a clear trend, although it does seem to increase with high exposure doses, over $4000 \mu\text{C cm}^{-2}$.

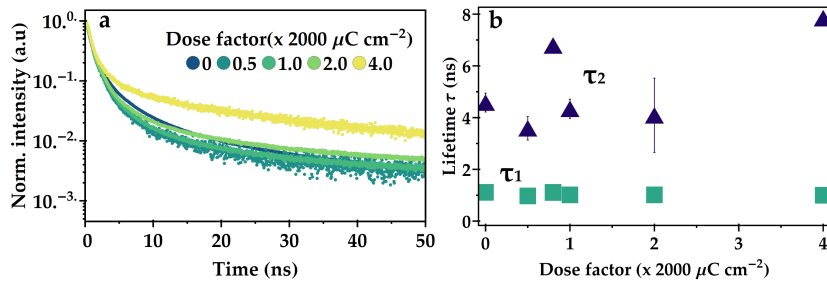


Figure 4.5: (a) Time resolved photoluminescence of exposed CsPbBr₃. (b) Fitted lifetime components.

The optical measurements therefore show an overall reduction in PL intensity with increasing exposure dose, although there is bright luminescence in developed structures with an unchanged lineshape. In a similar trend we observe an increase in absorption, likely due to changes in the refractive index. The measured radiative lifetime does not seem to change dramatically with dose, however. Although there are many processes that could influence the measured lifetime, it is possible that the short lifetime component is not purely radiative and therefore changes in non-radiative processes are less easily observed. For good integration into efficient devices, this requires more investigation.

In order to shed more light on the underlying patterning mechanism, we investigate the changes in the organic part of the perovskite, by measuring Fourier transform infrared spectroscopy (FTIR). The spectra of differently exposed perovskite films can be found in Figure 4.6. The changes are only very small, indicating no major loss of organic material. This excludes outgassing of volatile organic compounds as mechanism for changing absorption. The bands around 2950 cm^{-1} and 2850 cm^{-1} correspond to asymmetric and symmetric CH_2 stretches respectively. These are the most prominent bands due to the long carbon chains present in both oleic acid and oleylamine.

The features around 1450 cm^{-1} and 1550 cm^{-1} can be attributed to the COO^- anchoring group of oleic acid. These peaks are mostly unaffected by the exposure, indicating a good connection with the inorganic cations in the crystal structure, either Cs or Pb. An obvious change is the increase in the features between 3100 cm^{-1} and 3300 cm^{-1} , that can be ascribed to several NH_2 modes. This may indicate that with higher doses, more free amine-groups are present in the film, which could be an explanation for the decrease in PLQY, as not all facets of the perovskite will be properly passivated. The other change is happening in the wavenumber range around $1000 - 1100\text{ cm}^{-1}$. These peaks are related to stretches between two carbon atoms in a chain. The ratio between the high-wavenumber peak and the low-wavenumber peak is continuously shifting towards the latter with increasing dose. This points to rearrangement of ligand chains, and possible cross-linking. Overall we hypothesize that long ligands partly cross-link upon exposure, as we have observed before in previous work [134]. In combination with partial ligand detachment, which leads to charged surfaces, the nanocrystals are likely to form larger clusters of interconnected NCs. This strongly reduces the solubility of the crystals, thereby creating an insoluble material. The oleates are not affected, thereby keeping luminescence mostly intact.

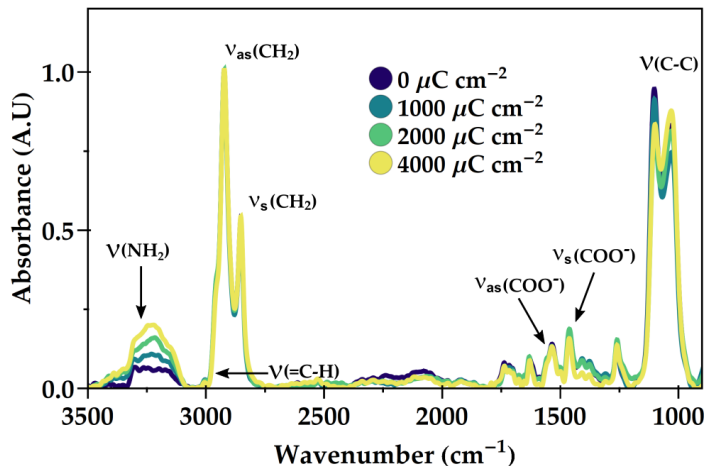


Figure 4.6: FTIR spectra of e-beam exposed CsPbBr₃. The films were exposed to different doses of electrons. The spectra are normalized to the peak at 2950 cm⁻¹. The main changes are observed in the amine groups and the arrangement of the C-C bonds within the long ligand chains.

4.3 CONCLUSION

We have shown that it is possible to pattern CsPbBr₃ nanocrystals in a simple one-step lithography process. We observe a reduction of PLQY of the material after processing, but luminescence remains and radiative decay is relatively stable. We attribute the patterning mechanism to cross-linking of the surface ligands, that next to passivating the surface and providing colloidal stability also function as the scaffold for creating a network that creates a cohesive perovskite pattern. The amine ligands, however, seem to partially detach from the crystal, thereby reducing the passivation. We can pattern the NCs down to 100s of nanometers. With this patterning of perovskite on the nanoscale it is possible to pursue better performing devices, for instance by making use of nanophotonic structures to engineer the emissive properties.

4.4 EXPERIMENTAL METHODS

Chemicals: Hexane (anhydrous) and toluene (anhydrous) were purchased from VWR. Lead bromide (PbBr₂, 98% pure) was pur-

chased TCI. Cesium carbonate (Cs_2CO_3 , 99.5% pure), 1-octadecene (ODE, technical grade 90%), oleic acid (OA, technical grade 90%), oleylamine (OIAM, technical grade 90%), tetrahydrofuran (THF, anhydrous, >99.9% pure), acetone (ACE, analytical grade), isopropanol (IPA, analytical grade), methanol (MeOH, analytical grade) were purchased from Sigma Aldrich. Double-side polished silicon wafers were purchased from Siegert Wafer. ITO-coated glass microscope slides (19 mm \times 19 mm) were purchased from Diamond Coatings.

Nanocrystal synthesis: Synthesis of the CsPbBr_3 nanocrystals was performed via a recipe adapted from Lu et al. [133] and Protesescu et al [37]. First cesium oleate precursor was prepared by adding 1.63 g of Cs_2CO_3 with 15.8 mL of OA with 34.2 mL ODE into a three-neck flask in a glovebox, to ensure oxygen and water-free conditions. The flask was attached to a Schlenk line and evacuated 3x and under flow of N_2 , then the solution was heated to 110 °C under continuous stirring for 3 hours until all precursors were dissolved and a clear solution with the color of melted butter had formed. The solution was cooled to room temperature, and small amounts were taken from this stock solution. For the final nanocrystal synthesis, 0.138 g PbBr_2 was combined in a glovebox with 0.5 mL OIAM, 0.5 mL OA and 10 mL ODE in a 50 mL three-neck flask. The flask was evacuated 3x and refilled with N_2 . Subsequently, the flask was heated to 120 °C and left for 1 hour to degas and boil off any water. The precursor dissolved as well and a clear, cream-colored solution formed. Subsequently, the temperature was increased to 150 °C and 1 mL of Cs-oleate precursor solution was injected. After a couple of seconds, the solution turned bright yellow/green and the reaction was subsequently quenched in an ice bath. The reaction solution showed bright green fluorescence under UV.

To purify the reaction product, 1 mL of the reaction liquid was mixed with 1 mL of toluene, followed by centrifugation at 12000 rpm for 10 minutes. The supernatant was discarded and the precipitate was dispersed in 200 μL of hexane. The solution was centrifuged for 10 minutes at 12000 rpm again and supernatant was again discarded. Finally, the precipitate was dispersed in 100 μL toluene and centrifuged 5 minutes at 4000 rpm. The supernatant was kept as final solution. This process was repeated until

all the reaction solution was purified.

Film preparation: Samples for exposure were made by spin-coating thin films of nanocrystals on clean silicon substrates. The substrates were cleaned by subsequent in soap water, DI water, ACE and IPA and finally 15 minutes of oxygen plasma. NC solutions were filtered (0.2 micron PTFE filter) and spin-coated at 2500 rpm for 20 seconds, resulting in films with a thickness of around 100 nm.

High-energy e-beam exposure: E-beam exposure was done in a Raith Voyager commercial e-beam lithography system with a voltage of 50 kV, LC30 column mode with 0.135 nA beam current. Films were developed in toluene immediately after exposure.

Scanning Electron Microscope: Scanning Electron Microscope images were taken by a FEI Verios 460 at voltages between 5 kV and 10 kV at 100 pA.

Atomic Force Microscopy: AFM images were taken on a Veeco Dimension 3100 (Bruker) in tapping mode. Linescan frequency was 1 Hz.

Photoluminescence: Photoluminescence of samples was measured using a WITec alpha300 SR confocal microscope with 100× Zeiss objective (NA 0.9). A 405 nm Thorlabs S1FC405 fiber coupled laser diode was used as excitation source. A 405 nm notch filter was used to remove the laser light in the detection path which was coupled to the detector. Light is collected in reflection on a UHTC 300 VIS WITec spectrometer. The PL spectra were converted to the energy scale using a Jacobian transformation [110]. The setup can be used to record single spectra as well as perform spatial PL mapping.

Photoluminescence lifetime measurements: Fluorescence lifetimes were recorded with a home-built TCSPC setup (PicoQuant PDL 828 “Sepia II” and a PicoQuant HydraHarp 400 multichannel) in an inverted microscope with an Olympus 60× Plan Apochromat water immersion objective. The samples were excited by a 485 nm laser (PicoQuant LDH-D-C-485), which was pulsed at a repetition rate of 10 MHz. The excitation laser signal was blocked in the detection path by a Thorlabs FEL-500 long-pass filter in combination with a 488-NF notch filter.

Absorption measurements: Absorption measurements were performed in a custom built integrating sphere setup, described

in previous work [135]. Absorbance was measured at 405 nm, under excitation of a 405 nm Thorlabs S1FC405 fiber coupled laser diode.

Optical microscope: Optical microscope images were recorded with a Zeiss, AxioCam ICc 5 equipped with a $20\times/0.2$ objective.

4.5 APPENDIX

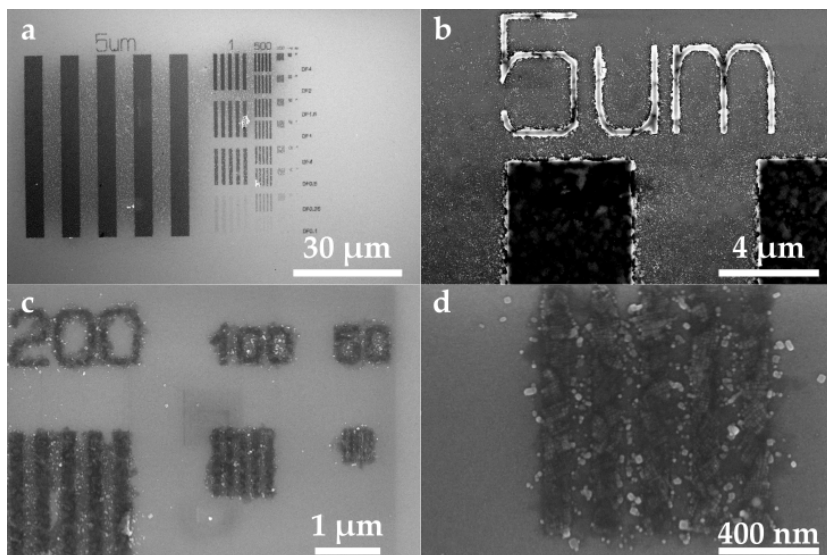
Overexposed perovskite nanostructures

Figure 4.7: SEM images of overexposed perovskite NC structures. The higher doses used in these parts of the exposure field ($4000 - 8000 \mu\text{C cm}^{-2}$) cause more residual NCs to remain on the substrate after development, even though in the intended patterns are also resolved.

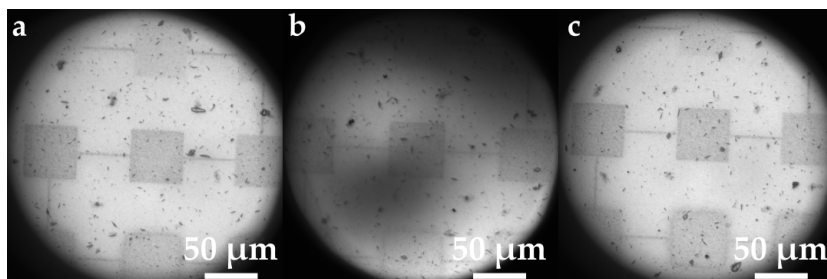
Optical microscope images of e-beam exposed perovskite NC films

Figure 4.8: Optical microscope images of 3 different e-beam exposed perovskite NC films. It is clear that exposure to the e-beam alters the absorbance of the films, as also observed in chapter 4, Figure 4.4.

TCSPC data of perovskite films

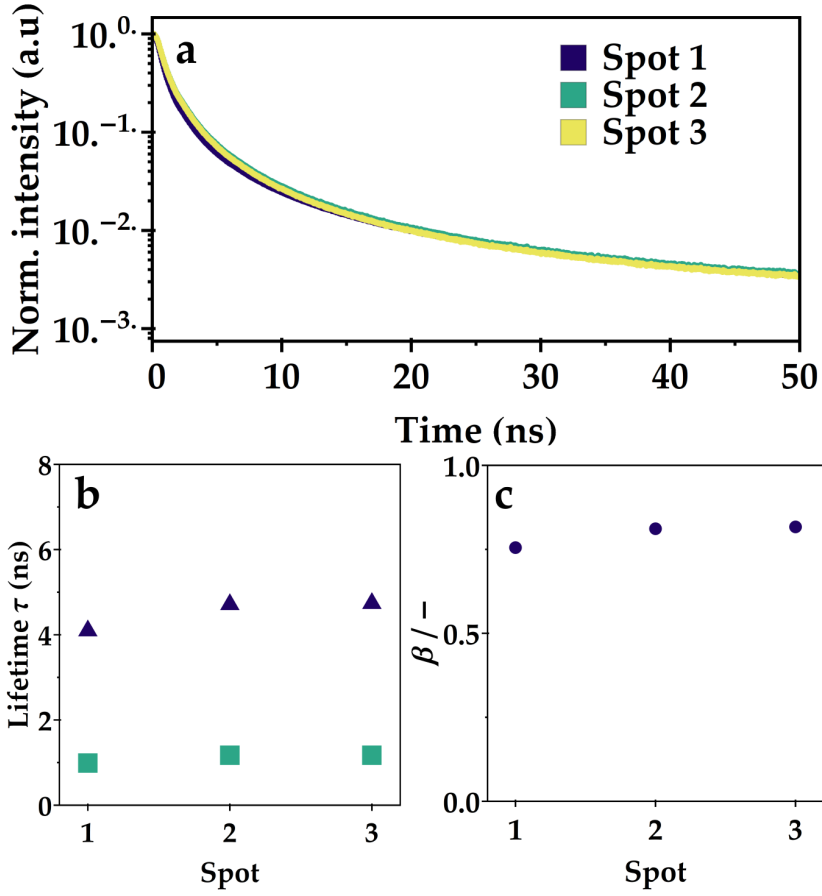


Figure 4.9: TCSPC data (a) and fitted lifetime components (b) τ_1 , τ_2 and (c) β .

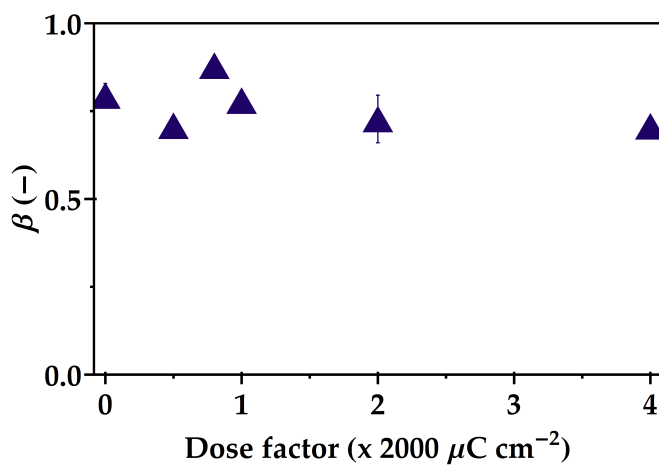


Figure 4.10: Fitted stretched exponent β of exposed perovskite films.

TOWARDS WAVEGUIDING AND LASING IN DIRECTLY PATTERNED COLLOIDAL QUANTUM DOT FILMS

*"To recognize that the greatest error is not to have tried
and failed, but that in trying, we did not give it our best
effort."*

— Gene Krantz (2000)

Parts of this chapter are based on:

Dieleman, C. D., Kolkowski, R., Pal, D., Geuchies, J.J., van der Burgt, J., Garnett, E.C., Houtepen, A.J., Koenderink, A.F. & Ehrler, B. "Directly patterned, electrochemically charged colloidal quantum dots for lasing devices" (in preparation)

5.1 INTRODUCTION

The excellent light-emitting properties of colloidal quantum dots (CQDs) make them interesting candidates for all kinds of applications. Their tunable bandgap, narrow emission line shapes and possibility to be used as single photon source, has made them exciting candidates for light-emitting diodes (LEDs) [136, 137], lasing structures [13, 138] and quantum emitters [8, 139]. Some CQD systems have already found their way into commercial products in several display technologies as accurate color filters. CQD lasers are among the most interesting applications of this class of nanomaterials. The combination of tunable emission wavelength, narrow line width with a cheap synthesis and solution processability, make for an attractive package that might unlock solution processable lasing devices. Some challenges, however, do remain. Although the quantum confinement effects, that give the colloidal CQDs their name, assure a large separation between quantized energy levels which makes the lasing threshold less sensitive to temperature fluctuations, the degeneracy of the band edge states requires that the average number of excitons in a CQD film is higher than 1 in order for stimulated emission to outcompete absorption [32]. Although CQDs support biexcitons, their lifetime is very short, in the order of <100 picoseconds [140]. This means that, in order to achieve optical gain and lasing, the CQD assembly needs to be pumped by high-powered continuous-wave lasers or with extremely short femtosecond pulses in order to put enough energy density into the system.

One way of overcoming this challenge is by charging or doping of the CQDs. The concept of doping is visualized in the scheme in Figure 5.1. In an undoped system, two conduction band (CB) edge states are available. After excitation, electrons, and the holes they leave behind in the valence band (VB), will thermalize to the band edges. In this situation there is an equilibrium between electrons at the band edges, in both energy levels. Therefore, the probability of a second photon being absorbed and exciting a second electron into the remaining CB edge state equals the probability it will cause stimulated emission of the first excited electron. On average the system will behave like a transparent material, since as many photons "leave" the material as are com-

ing in. A state of population inversion will only be reached when the ground state is quickly depleted by fs excitation or high excitation densities. Optical gain is only achieved when the stimulated emission can outcompete the absorption by excitation of VB edge electrons. When the material is doped, however, the lowest CB states at the band edge are already occupied. This effectively reduces the ground state absorption and therefore lowers the threshold for amplified stimulated emission (ASE), allowing for lower excitation densities to be sufficient to reach a state of population inversion. Previous works have shown that doping the CB of CdSe QDs is indeed a way to lower the gain threshold to values below one exciton per quantum dot [30, 77, 141]. There are several approaches to dope the CQDs either by photochemical doping or electrochemical charging. With photochemical charging an exciton is created in the quantum dot by the absorption of a photon. By adding a hole scavenger in the film, the electrons remain in the CQDs, effectively doping the CB edge. The downside of this method, is that the hole scavenger can be depleted as it is a sacrificial molecule, thereby losing its effectivity. This method also gives little direct control over the doping level, as the system needs to be excited first to create the charges.

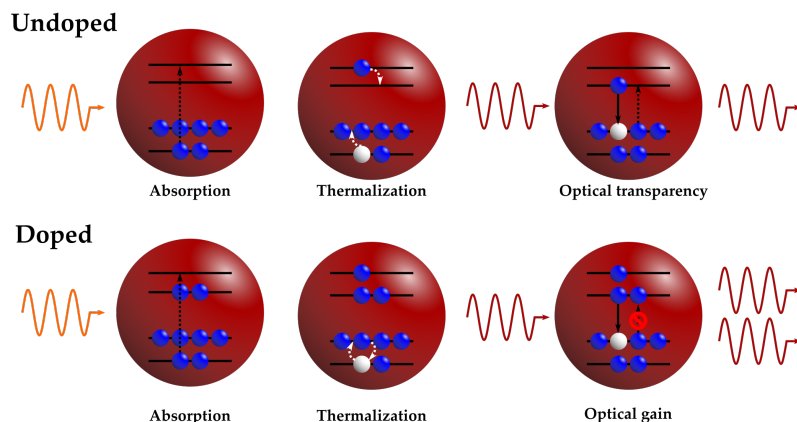


Figure 5.1: The principle of gain in doped CQDs. In an undoped system 2 electrons can occupy the CB edge states. After excitation of one electron, a second photon can either be absorbed or cause stimulated emission, leading to an average state of optical transparency. In the doped system, band edge transitions are initially blocked, meaning that after excitation of electrons higher than the bandgap and thermalization of the holes, a state of population inversion is reached much quicker, allowing for optical gain.

Electrochemical doping on the other hand works by applying a potential in an electrochemical cell where the quantum dot medium will act as a cathode that is reduced by injecting electrons. By countering the added negative charges by mobile ions in the electrolyte that can move into the quantum dot film, the charges can be stabilized inside the CQDs [142]. The benefits of this approach are the stability of doping, the reversibility and the accurate control over the doping levels. By simply changing the applied potential, the doping can be used to either only passivate trap states in the bandgap or also dope the other energy levels in the bands to a larger or smaller extent. Recently it was shown that this electrochemical doping does give a high degree of control over the gain threshold of CdSe/CdS/ZnS CQDs and can therefore be used to create and tune an effective gain medium [30].

In order to achieve lasing, it is however also necessary to combine an effective gain medium with an optical cavity. There are several examples of quantum dot films combined with optical cavities in order to achieve lasing [13, 138, 143, 144]. In all of these cases, the cavity is placed below or on top of the emitting

material either in the form of Fabry-Pérot cavity or distributed feedback (DFB) grating. Prins et al. showed that by creating 2D Bragg gratings out of CQDs, the Bragg scattering can manipulate the light emission [16], while Le Feber et al. used ring resonators made of CQDs to achieve lasing [13]. In both cases the CQDs are deposited into a template to form the pattern. In this work, we pattern the emitter (CdSe/CdS/ZnS CQDs), by means of direct electron-beam lithography (EBL) into a waveguiding structure that can supply distributed feedback to the system in order to act as an optical cavity. We observe directional emission of the outcoupled light and we can control the angle of emission by adjusting the grating period. We do not yet observe lasing in our structures. With the help of optical simulations we make suggestions towards fabricating a device that will show successful lasing with a low-threshold gain due to electrochemical charging.

5.2 BRAGG GRATINGS

For our design we choose to use a Bragg grating design as it can provide strong feedback in a system with a simple design. The Bragg equation, Equation 5.1, describes the relationship between the wavelength of light, the direction of light emission and the grating properties.

$$k_0 \sin \theta = \pm \frac{(2\pi n_{eff})}{\lambda_{em}} \pm m \frac{2\pi}{\Lambda} \quad (5.1)$$

where:

k_0 = The wave vector of the light

θ = The angle of light in free space

n_{eff} = The effective refractive index of the grating

m = The grating order

λ_{em} = Wavelength of the light

Λ = Periodicity of the grating

By matching the periodicity to the emission wavelength, one can obtain a wavevector in the out-of-plane direction, where θ

= 0 degrees. Simultaneously, there is a higher order mode in the in-plane direction providing distributed feedback, acting as optical cavity. By creating a bullseye grating, the grating period is the same in every radial direction, therefore providing this feedback from every direction in the plane. The downside of this type of grating, however, is that this effect is strongest when the center is excited, while the further one moves to the outside of the structure, towards larger radii of the concentric rings, the more the grating will behave like a line grating.

We fabricate these structures from CdSe/CdS/ZnS CQDs, that have shown to be efficient quantum dot emitters, and can be charged electrochemically to lower their gain threshold [30]. We fabricate the gratings from the emitters themselves via direct EBL as developed and described in an earlier work [134]. We use indium tin oxide (ITO)-coated glass substrates in order to allow for the electrochemical charging of the CQDs during the measurements. This conductive substrate can also dissipate charges during the electron-beam patterning. We spin coat a 80 - 100 nm film of CQDs on top of the substrate and irradiate the films directly with the e-beam. After development in tetrahydrofuran (THF) we obtain the desired structures as the e-beam cross-links the ligands and turns the individual CQDs into an insoluble cohesive structure. Figure 5.2 shows the fabrication process (a) and SEM images of the structures (b,c). We created a bullseye grating with a duty cycle of 50% and varying pitch from 300 to 500 nm. Each grating consisted of 300 concentric rings, thereby varying the size of the overall gratings, depending on the periodicity. The process leads to clear periodic structures from the CQDs directly. The edges are well defined, and individual CQDs can still be identified. These structures are large enough to be visible by eye, and illuminating the patterned substrates with UV light shows they remain brightly fluorescent, as seen in Figure 5.2d. Figures 5.2e and f show that the light is scattering differently from gratings with a different periodicity, indicating that the gratings are effectively interacting with incoming light.

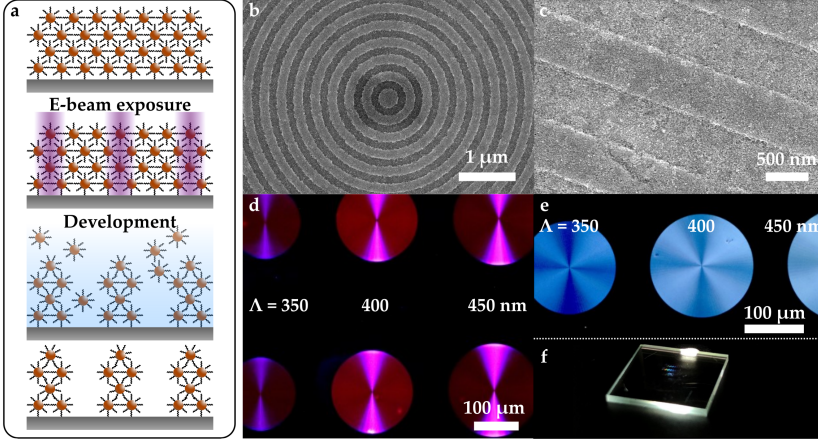


Figure 5.2: (a) Fabrication of bulls-eye gratings from CdSe CQDs following the direct EBL method described in earlier chapters. (b,c) SEM images of different gratings fabricated with direct EBL. The structures are well defined. (d,e) Optical microscope images of fabricated gratings with different periodicities under (d) UV or (e) regular illumination. The outcoupling of light for the grating with $\Lambda = 400$ nm is more efficient and therefore appears brighter. (f) Fabricated gratings on top of ITO-coated glass. The different gratings reflect different colors of light, depending on their periodicity.

We investigate the effect of the patterned structures on the angular emission pattern by characterizing the emission in Fourier space. We investigate the structures in with two different setups (see Experimental section, 5.6), one with continuous wave excitation at 405 nm and one with a femtosecond pulsed laser at 400 nm. We can measure the Fourier image of the emission pattern at a camera as well as on a spectrometer, to get a view of the dispersion relation of the emission in k -space as function of wavelength. Figure 5.2a shows the Fourier images of gratings with different periodicities varying from 300 nm to 500 nm in steps of 50 nm. We can clearly see that the structuring of the CQDs has a direct effect on the outcoupling of the light. When exciting the structures in the center, we observe rings of brighter intensity around the origin of the image at $k_x = 0$ and $k_y = 0$ with a radius depending on the periodicity. This is a clear indication that the light is directed into fixed angles depending on the periodicity, just as we would expect from Bragg scattering. We observe a good agreement between the Bragg theory (red lines in Figure 5.2a) and our measurements. Deviations are most likely from

manufacturing imperfections, as the edges of our gratings are not perfectly smooth. When we spectrally resolve the image of the back-focal plane (Figure 5.2b) we can also observe a clear trend when moving from structure to structure. As we move from structures with small periodicity (300 nm) to high periodicity (500 nm) we observe two bands, indicative of a photonic band structure, expected from the positive and negative term in equation 5.1. These lines are converging until they crossover in the $\Lambda = 400$ nm grating at 1.99 eV / 620 nm, close to the photoluminescence (PL) peak at 1.98 eV / 625 nm. By increasing the periodicity further, the bands start diverging. The crossover point of these bands is what we aim for, as it is indicative of a resonance at $k_{\parallel} = 0$ and therefore shows emission out-of-plane in a very narrow cone. This is thus also the period where we expect the strongest distributed feedback from the grating. The Fourier camera image shows that the only feature in this image is a bright spot in the middle, signaling directional emission in the direction normal to the sample plane. This effect can also be observed under a regular optical microscope, where the grating with the matching periodicity to the emission wavelength ($\Lambda = 400$ nm) appears to have brighter PL, which can be explained by the more effective outcoupling of the light in the direction of the objective.

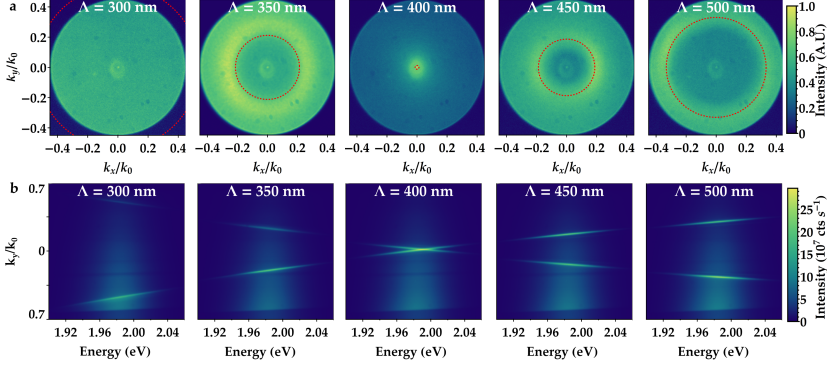


Figure 5.3: (a) Colormaps of Fourier space camera images of CdSe gratings with different periodicity. We observe rings of higher intensity around the center of the image, corresponding to light being scattered into specific angles. A periodicity of $\Lambda = 400$ nm causes bright emission into a small cone out-of-plane. Red circles indicate the expected angles of emission from Bragg theory. (b) Spectrally resolved Fourier images. We observe 2 bands converging and crossing each other at $k_{\parallel} = 0$ at the emission wavelength for the $\Lambda = 400$ nm grating, indicating out-of-plane emission optimized for the peak emission wavelength of the CQDs.

5.3 TOWARDS A LASING CQD DEVICE

The next step in getting to a lasing device is by electrochemically charging the sample and doping the CQDs with electrons. Figure 5.4 shows the PL spectrum over time, while the patterned films are periodically charged and discharged and therefore doped and dedoped by ramping the potential up and down between the open-circuit voltage of -0.3 V and -1.5 V against an Ag pseudo-reference electrode (PRE). Photoluminescence is quenched when the film is charged due to increased Auger recombination when charging the film. This pattern is similar to previously reported work, indicating that after patterning it is still possible to reversibly dope the material [30]. This control is important for realizing a lasing CQD device.

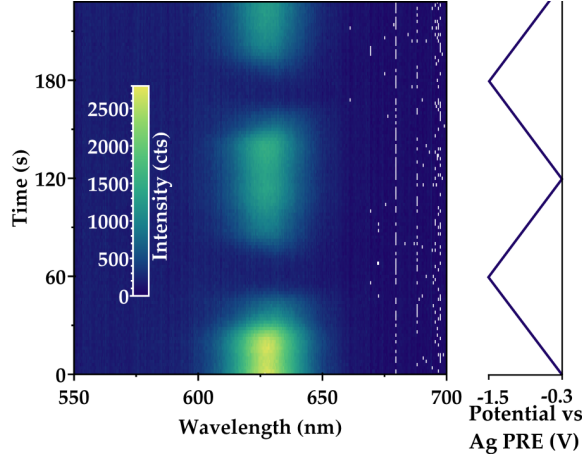


Figure 5.4: PL from patterned CQDs under applied potential. With the patterned CQD films as working electrode, the potential is cycled from -0.3 V, the open-circuit voltage, to -1.5 V. PL is quenched due to increased Auger recombination when the film gets charged.

Although we observe that our patterned CQD surfaces manipulate the light emission, we are not able to observe lasing from these metasurfaces, not even at extremely high pumping powers. This means that, even under these conditions, the gain is smaller than the loss in the system.

In order to understand our system better, and determine largest loss factors, we perform optical simulations. We determine the presence of optical resonances and their locations within the structures and check whether the fabricated structures can sustain a waveguided mode through the emitting layer. We model a simple 1D system in COMSOL, similar to our experimental grating, where we have a layer 120 nm CQDs on top of a 250 nm ITO layer on top of glass. The medium above the CQDs is simulated as air. We model the system for a periodicity of 400 nm with a 50% duty cycle. The results can be found in Figure 5.5. We do observe the presence of a waveguiding mode in the ITO layer, under the grating. This mode does cause a standing wave perpendicular to the substrate, leading to directional out-of-plane emission. We can observe this resonant optical mode also by a dip in transmission in Figure 5.5. The exact location of this dip is not exactly at the emission wavelength, but at 645 nm, indicating that a slight

change in the periodicity of the structure may achieve stronger resonance at 625 nm. When looking in the in-plane optical mode, we do observe a mode at 660 nm, again mostly present in the ITO or CQD layer. Both of these results suggest that the high index of the ITO ($n = 1.8$), which is higher than the index of the CQD layer ($n = 1.75$), is pulling the optical mode into the substrate, thereby not enhancing the electric field in the emitter layer enough to achieve lasing, but rather moving it to a location with high loss.

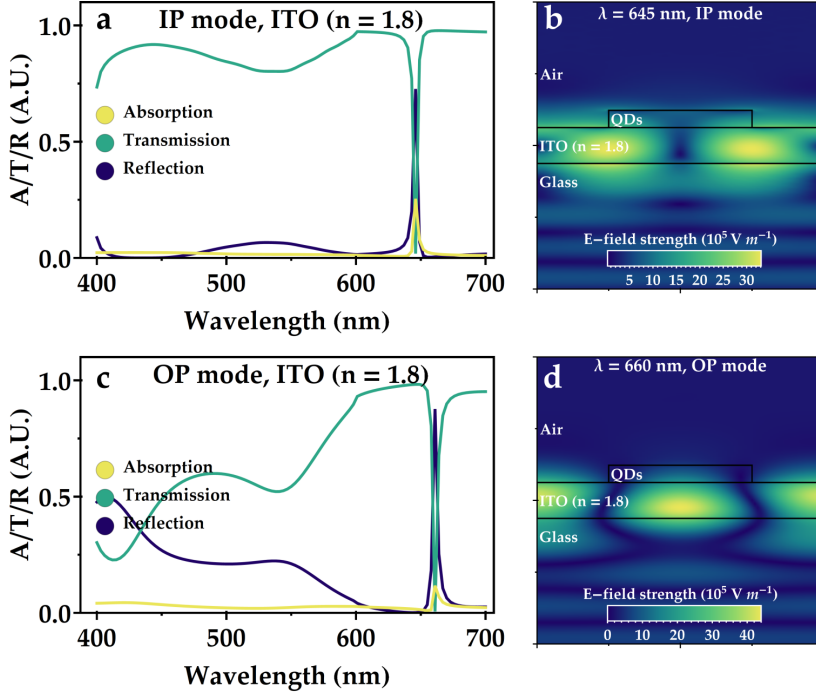


Figure 5.5: Results of optical modeling of our Bragg grating, as fabricated. We model a 120 nm film of CQDs on top of $n = 1.8$ ITO and glass in air. We scan a wavelength range in order to find optical modes in in-plane direction (a) and out-of-plane (c) direction. The spatial distribution of electric field strength of the modes in in-plane (b) and out-of-plane (d) directions. The modes are mostly present in the ITO layer.

5.4 DISCUSSION AND OUTLOOK

By extending the optical modeling we can investigate different systems to recommend changes to our design in order to achieve lasing in future devices. The primary challenge is to have a larger

share of the optical mode in the CQD layer than in the ITO. Here we discuss three possible changes to the pattern to accommodate this: refractive index changes in the ITO, increased CQD layer thickness and an index matching top layer. As mentioned in the previous section, patterning the emissive layer does affect the electric field and allows for waveguiding modes to exist in the stack. The relatively high index of the ITO, however, pulls the optical mode into this layer, thereby reducing the optical field strength in the CQD layer. By lowering the ITO index, the CQDs on top will become the higher index material and therefore a larger part of the optical mode's energy will live in the emitter layer. Previously the Klimov group has shown that this type of "index engineering" can be beneficial to confine the optical mode into the emitter layer when building lasing devices from CQDs. The desired lower index of $n = 1.5$ can be achieved by co-sputtering ITO and SiO_2 [138].

The second approach would be to fabricate patterned layers of CQDs on top of a dense base layer. In the current structures, the layer thickness is achieved by a one-layer spin-coating of a solution with very high concentration. In such an approach, the first layer would be spin-coated with intermediate concentration, followed by chemical cross-linking with a ligand exchange that immobilizes the CQDs. A second layer on top of the first could then be patterned into the desired grating.

Finally, one can confine an optical mode in the intermediate CQD layer by adding an extra layer on top of the patterned structure that is index matched to the substrate. This creates a waveguide much like the classic optical fiber. This top layer could be an insulating polymer layer like poly(methyl methacrylate) (PMMA) or SU-8, but as we are seeking to electrochemically dope the material as well, we instead suggest that this index-matched material will be the electrolyte. In the case of lower-index ITO, one such electrolyte could be dimethylsulfoxide (DMSO) which has a refractive index of $n = 1.479$. Figure 5.6 shows the optical mode in case of incorporating all these changes to the system. The individual contributions of these changes can be found in the appendix 5.7. As can be seen in Figure 5.6, the combination of these approaches is beneficial for confining the optical mode into the quantum dot layer, as lowering the ITO index moves the mode

more into the CQDs, the top layer pulls the mode even further out of the ITO and the increased CQD layer thickness accommodates a larger fraction for the mode in the emitter, although the effect is not as strong for the in-plane mode. In the case of increased CQD layer thickness with low-index ITO in air, there is also a strong in-plane mode in the CQD layer (see appendix Figure 5.12), however, the mode in the out-of-plane direction is less confined to the emitter layer. It is, however, clear that an increase in emitter layer thickness combined with low-index ITO will be beneficial. Finally, it should be noted that the modes are not yet coinciding with the wavelength of peak emission. Therefore, small changes to the periodicity should be made as well, in order to optimize the system further. With these improvements to the system, we are confident that lasing can be achieved from a solution processed device in the near future.

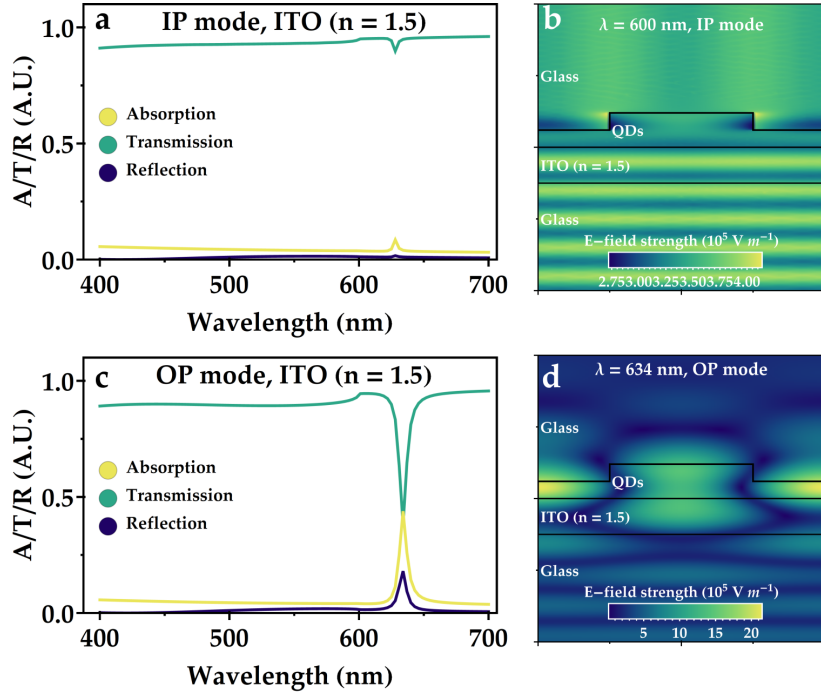


Figure 5.6: Results of optical modeling of our Bragg grating, with changes to the design: increased 240 nm film of CQDs between $n = 1.5$ ITO and glass and another layer of glass on top. We scan a wavelength range in order to find optical modes in in-plane (a) direction and out-of-plane (c) direction. The spatial distribution of electric field strength of the modes in in-plane (b) and out-of-plane (d) directions. The mode in-plane is not very strong, but the out-of-plane mode is now mostly present in the CQD emitter layer.

5.5 CONCLUSIONS

We have shown waveguiding structures patterned from emitters directly. Direct EBL is a suitable fabrication technique to pattern colloidal CQDs into optical surfaces to manipulate light emission. We show control over the angle of emission and that a standing wave for out-of-plane emission forms in the quantum dot grating. Electrochemical doping of the CQD structures is still possible at -1.5 V similar to unpatterned CQD films. In the current system, losses are too high to allow for lasing. In order to create an optical cavity that can support lasing, we need to adjust our system further. Here, index engineering plays an important role as the current structure does not confine enough of the mode

inside the emitter. By lowering the substrate index, increasing the emitter layer thickness and possibly adding an extra layer index-matched material on top, a lasing device can be achieved in the foreseeable future.

5.6 EXPERIMENTAL METHODS

Chemicals: Tetrahydrofuran (THF, anhydrous, >99.9% pure), octane (anhydrous, >99% pure), acetone (ACE, analytical grade) and isopropanol (IPA, analytical grade) were purchased from Sigma Aldrich. Double-side polished silicon wafers were purchased from Siegert Wafer. ITO-coated glass slides were purchased from Kintec and cut into (15 mm \times 15 mm) substrates.

Nanocrystal synthesis: Nanocrystal synthesis was performed following previously reported methods [30]. In short, the CdSe core crystals were synthesized by adding 60 mg of CdO with 280 mg of octadecylphosphonic acid (ODPA) in 3 g of TOPO in a three-neck flask. The mixture was heated to 150 °C under vacuum for 1 hour to melt the products and degas the solution. After 1 hour, the mixture was heated to 320 °C. After the solution turns clear, 1 mL of trioctylphosphine (TOP) was added before raising the temperature to 380 °C. At this temperature, a Se-precursor of 60 mg Se in 0.5 mL TOP was swiftly injected. After \pm 25 seconds reaction time, the reaction liquid was cooled to room temperature with an airgun. Purification was done by adding equal parts of methyl acetate to the reaction liquid, centrifugation and redispersion in hexane, followed by filtering thorough Milipore 0.2 μ m filters and a second washing step.

Synthesis of Cd-Oleate and Zn-Oleate: Cd-oleate was prepared by dissolving 1.32 g Cd-acetate with 7.4 g OA in 52.4 g ODE. For the Cd-oleate synthesis, 1.32 g of Cd-(acetate)₂ was dissolved in 52.4 g of ODE and 7.4 g of OA. The mixture was heated to 120 °C and left for 3 hours under vacuum. After 3 hours the solution was cooled to room temperature.

For Zn-oleate, Zn(II)-(acetate)₂ was added to 1.6 mL of OlAm and 1 g of OA in a 20 mL vial. The vial was heated in a nitrogen-purged glovebox to 130 °C.

Shell Growth of CdS and ZnS: For the CdS shell growth, 50 nmol of CdSe cores and 3.0 mL of ODE were added to a three-neck

flask. The mixture was degassed for 1 hour at room-temperature and for 2 hours at 120 °C. Subsequently, the solution was heated to 310 °C under a nitrogen flow. During the heating, from 240 °C onwards, Cd-oleate and 1-octanethiol in 8 mL ODE were injected dropwise using a syringe pump. After growth of the CdS shell the solution was degassed at a pressure of 0.5 mbar for 1 hour at 120 °C. For growing the ZnS shell, the core/shell solution is heated to 280 °C under nitrogen flow. At 210 °C a desired amount of Zn-oleate and 1-octanethiol in ODE was injected at a rate of 2 mL h⁻¹. After precursors are finished, the solution was cooled to room temperature with an airgun. The solution was washed twice by addition of methanol:butanol (1:2), redispersed in hexane centrifuged and washed once more with methyl acetate and finally redispersed in toluene. Finally, the solution was filtered with a 0.2 µm filter and stored in the glovebox.

Film preparation: Samples for exposure were made by spin-coating thin films of nanocrystals on clean silicon substrates. The substrates were subsequently cleaned in soap water, DI water, ACE and IPA and finally 15 minutes of oxygen plasma. NC solutions were filtered (0.2 micron PTFE filter) and spin-coated by adding a drop of 40 µL to the substrate and spinning 60 seconds at 500 rpm, followed by 30 seconds at 500 rpm, resulting in films with a thickness of around 80 - 100 nm.

High-energy e-beam exposure: E-beam exposure was done with a Raith Voyager commercial e-beam lithography system with a voltage of 50 kV, in MC40 or MC60 column mode with a 0.94 ± 0.02 or 2.20 ± 0.05 nA beam current, respectively. Films were developed by immersion in refrigerated THF for 45 - 50 seconds immediately after exposure, followed by a quick rinse in anhydrous octane. The sample was dried with a nitrogen gun.

Scanning Electron Microscope: Scanning Electron Microscope images were taken by a FEI Verios 460 at voltages between 5 kV and 10 kV at 100 pA.

Fourier microscopy: For recording of k-space images of the bullseye gratings two setups were used. The first setup is described by addition of a Fourier setup to an existing setup [135, 145]. For the Fourier path, a pellicle beam splitter (BP145B1 Thorlabs) was added right behind the objective. The samples were excited with a 405 nm laser (S1FC405 Thorlabs). The detection path consists of

a 450 nm long-pass filter, a set of telescopic lenses, a Fourier lens (0.4 NA) that can be taken out for real-space imaging, a tube lens and a CCD camera (Retiga Lumo model 01-RET-LUMO-R-M-16-C, Teledyne Photometrics). Fourier images were taken at 200 and 500 ms integration time, with 2×2 pixel binning.

In the second setup we used a pulsed femtosecond laser beam with a central wavelength of 400 nm, repetition rate 1 MHz and average power of around 1 μ W to excite the patterned CQD structures. This beam is created by frequency doubling of a near-infrared output beam from a Light Conversion ORPHEUS-F Optical Parametric Amplifier (OPA) at 800 nm, 1 MHz repetition rate, pulse duration around 120 fs. The infrared beam is focused on a beta-barium borate (BBO) crystal, producing second-harmonic generation (SHG) at 400 nm which is then collimated and filtered by a 750 nm short-pass filter. The blue light is coupled to a 10 m-long optical fiber and transported to another setup, where the light from the fiber is collimated by Nikon objective (10 \times , NA = 0.25). This beam is additionally filtered using a band-pass filter (400 nm center wavelength, 40 nm transmission window) and transmitted through a pair of linear polarizers for control of the power and polarization of the beam. Finally, the beam is focused by a Nikon objective (10 \times , NA 0.25), and incident on the sample. Emission is collected on the other side of the sample using a Nikon objective (50 \times , NA = 0.7). A 500 nm long-pass filter is used to block the beam. Images of the back-focal plane can be collected either in 2D on a Andor Clara CCD camera sensor, providing panchromatic Fourier images of luminescence, or in 1D, by Andor iVAC CCD camera using Shamrock 303i imaging spectrometer, providing spectrally resolved Fourier images of luminescence. Clear signatures of grating anomalies are recorded when the CQD grating grooves are oriented horizontally (as imaged in the camera sensor frame), and excited by a blue beam polarized parallel to the grooves. A figure of the setup can be found in the appendix 5.7.

Electrochemical charging of CQD films: We measured the spectro-electrochemical response of our CQD film in a three-electrode configuration, where the QD film on ITO was our working-electrode (WE), we used a Ag PRE and a Pt counter electrode (CE). The electrodes were submerged in a 0.1 M LiClO₄ in acetonitrile

electrolyte solution. The potential between the WE and PRE was scanned with 20 mV s^{-1} in between the open-circuit potential (-0.3 V) and -1.5 V two times, controlled by a PGSTAT128N Autolab potentiostat, and simultaneously, the PL of the film was recorded with a fiber-based UV-vis spectrometer (USB2000, Ocean Optics).

Optical simulations: We use finite element method simulations software COMSOL Multiphysics v5.2 to model the bullseye system. We approximate the 2D bullseye system as a 1D periodic array with a fixed pitch of 400 nm . As the system is large, we use Bloch - Floquet boundary conditions at the sides of the unit cell (along the periodicity axis) in the model. We defined two ports at the ends (perpendicular to the periodicity axis), namely the excitation and receiving port. The model was illuminated with a plane wave at normal incidence at the excitation port with both in-plane and out-of-plane electric field vectors and placed in the glass medium. The receiving port is on the air side; it absorbs almost all the incident light without any artificial reflection from that air boundary.

Optical microscope: Optical microscope images were recorded with a Zeiss, AxioCam ICc 5 equipped with a $20\times/0.2$ objective or $50\times/0.2$ objective.

5.7 APPENDIX

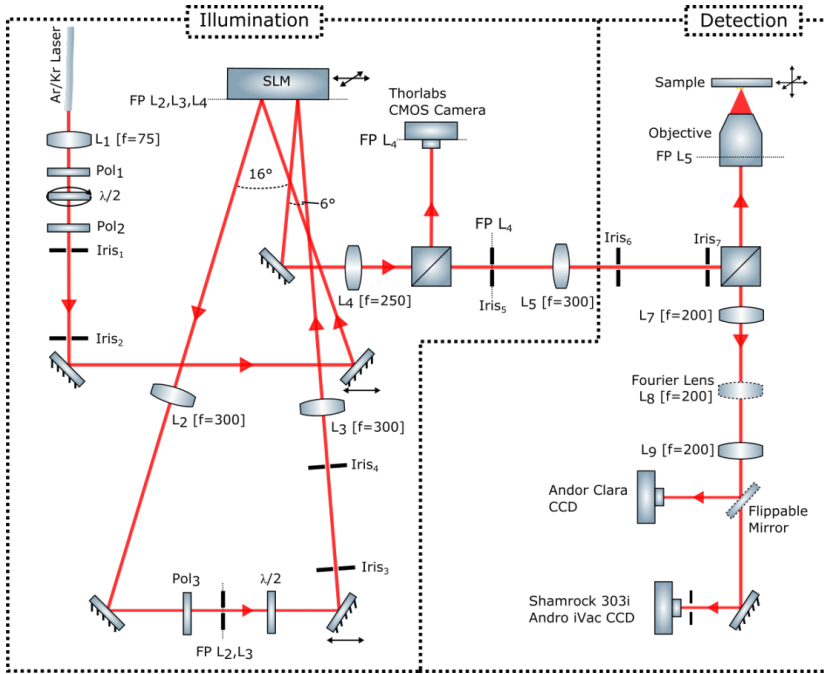
Laser setup for Fourier imaging

Figure 5.7: Overview of laser setup used for imaging spatial and spectral Fourier images.

Optical modeling results in thin CQD structures

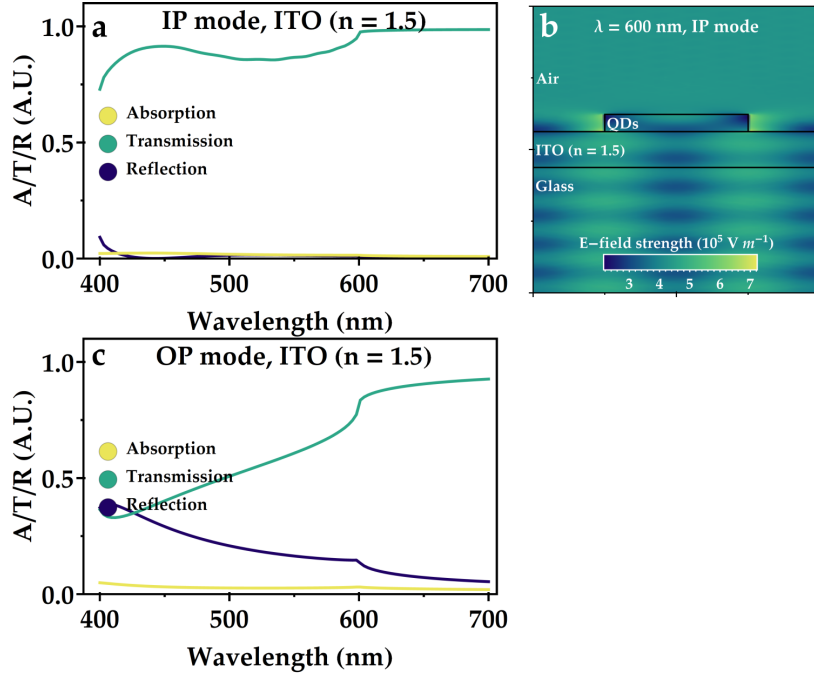


Figure 5.8: Results of optical modeling of our Bragg grating, with changes to the design: 120 nm film of CQDs on top of low-index $n = 1.5$ ITO and glass in air. We scan a wavelength range in order to find optical modes in (a) in-plane direction and (c) out-of-plane direction. The spatial distribution of electric field strength of the modes in (b) in-plane direction. We find no modes in the out-of-plane direction.

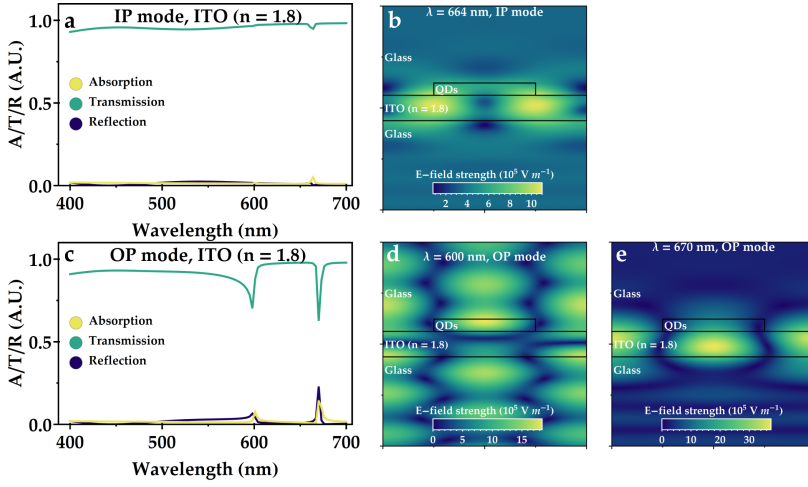


Figure 5.9: Results of optical modeling of our Bragg grating, with changes to the design: 120 nm film of CQDs on top of regular $n = 1.8$ ITO and glass, but with glass on top. We scan a wavelength range in order to find optical modes in (a) in-plane direction and (c) out-of-plane direction. The spatial distribution of electric field strength of the modes in (b) in-plane and (d,e) out-of-plane directions.

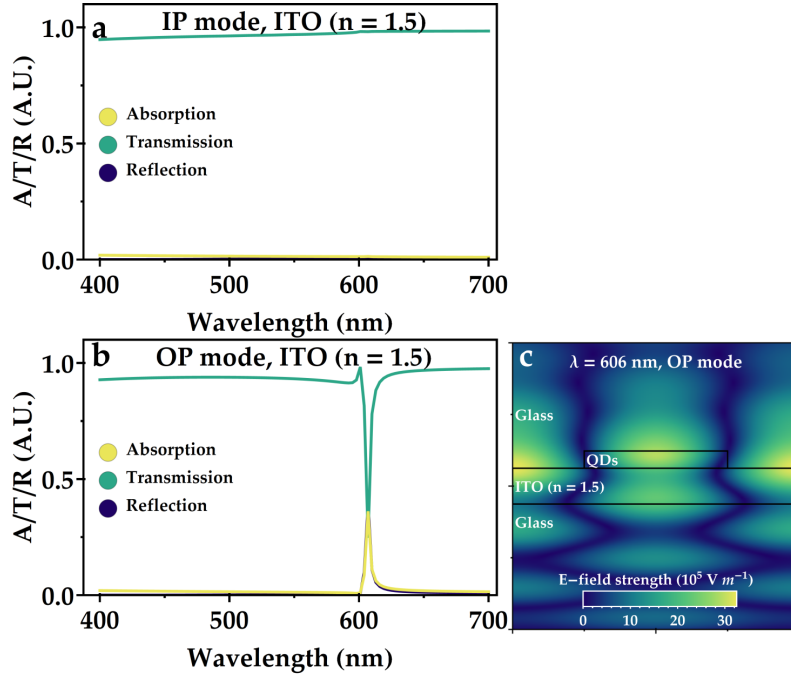


Figure 5.10: Results of optical modeling of our Bragg grating, with changes to the design: 120 nm film of CQDs on top of low-index $n = 1.5$ ITO and glass, but with glass on top. We scan a wavelength range in order to find optical modes in (a) in-plane direction and (b) out-of-plane direction. The spatial distribution of electric field strength of the modes in (c) out-of-plane direction. We find no modes in the in-plane direction.

Optical modeling results in thin CQD structures

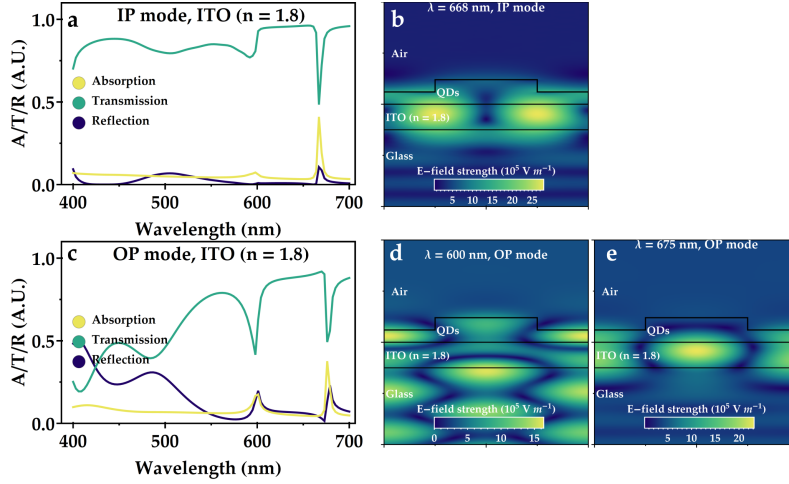


Figure 5.11: Results of optical modeling of our Bragg grating, with changes to the design: increased 240 nm film of CQDs on top of regular $n = 1.8$ ITO and glass in air. We scan a wavelength range in order to find optical modes in (a) in-plane direction and (c) out-of-plane direction. The spatial distribution of electric field strength of the modes in (b) in-plane and (d,e) out-of-plane directions.

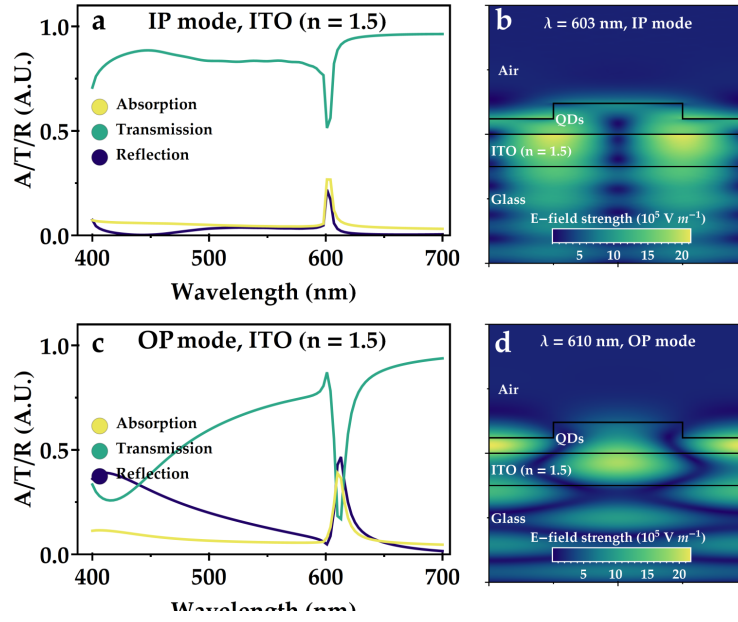


Figure 5.12: Results of optical modeling of our Bragg grating, with changes to the design: increased 240 nm film of QDs on top of $n = 1.5$ ITO and glass in air. We scan a wavelength range in order to find optical modes in (a) in-plane direction (c) and out-of-plane direction. The spatial distribution of electric field strength of the modes in (b) in-plane and (d) out-of-plane directions.

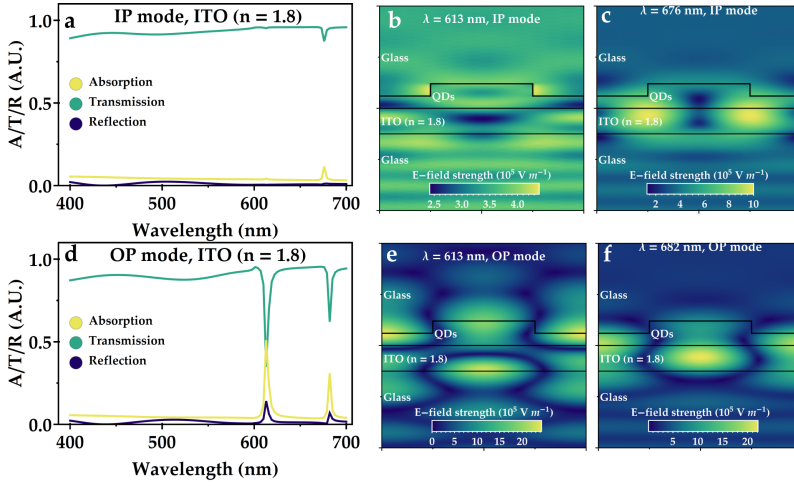


Figure 5.13: Results of optical modeling of our Bragg grating, with changes to the design: increased 240 nm film of CQDs on top of regular $n = 1.8$ ITO, but with glass on top. We scan a wavelength range in order to find optical modes in (a) in-plane direction (d) and out-of-plane direction. The spatial distribution of electric field strength of the modes in (b,c) in-plane and (e,f) out-of-plane directions.

REFERENCES

- [1] X. Lan, O. Voznyy, F. P. García de Arquer, M. Liu, J. Xu, A. H. Proppe, G. Walters, F. Fan, H. Tan, M. Liu, Z. Yang, S. Hoogland, E. H. Sargent, *Nano Letters* **2016**, *16*, 4630–4634.
- [2] Q. A. Akkerman, M. Gandini, F. Di Stasio, P. Rastogi, F. Palazon, G. Bertoni, J. M. Ball, M. Prato, A. Petrozza, L. Manna, *Nature Energy* **2017**, *2*, 1–7.
- [3] R. Wang, X. Wu, K. Xu, W. Zhou, Y. Shang, H. Tang, H. Chen, Z. Ning, *Advanced Materials* **2018**, *30*, 1704882.
- [4] N. Kirkwood, B. Singh, P. Mulvaney, *Advanced Materials Interfaces* **2016**, *3*, 1600868.
- [5] G. Li, F. W. R. Rivarola, N. J. L. K. Davis, S. Bai, T. C. Jellicoe, F. de la Peña, S. Hou, C. Ducati, F. Gao, R. H. Friend, N. C. Greenham, Z.-K. Tan, *Advanced Materials* **2016**, *28*, 3528–3534.
- [6] G. Azzellino, F. S. Freyria, M. Nasilowski, M. G. Bawendi, V. Bulović, *Advanced Materials Technologies* **2019**, *4*, 1800727.
- [7] T. B. Hoang, G. M. Akselrod, M. H. Mikkelsen, *Nano Letters* **2016**, *16*, 270–275.
- [8] X. Lin, X. Dai, C. Pu, Y. Deng, Y. Niu, L. Tong, W. Fang, Y. Jin, X. Peng, *Nature Communications* **2017**, *8*, 1132.
- [9] V. Adinolfi, I. J. Kramer, A. J. Labelle, B. R. Sutherland, S. Hoogland, E. H. Sargent, *ACS Nano* **2015**, *9*, 356–362.
- [10] D. M. Balazs, N. Rizkia, H.-H. Fang, D. N. Dirin, J. Momand, B. J. Kooi, M. V. Kovalenko, M. A. Loi, *ACS Applied Materials & Interfaces* **2018**, *10*, 5626–5632.
- [11] D. J. Norris, *Nature Photonics* **2019**, *13*, 230–232.
- [12] C. Huang, X.-B. Li, C.-H. Tung, L.-Z. Wu, *Chemistry - A European Journal* **2018**, *24*, 11530–11534.
- [13] B. Le Feber, F. Prins, E. De Leo, F. T. Rabouw, D. J. Norris, *Nano Letters* **2018**, *18*, 1028–1034.

- [14] C. R. Kagan, E. Lifshitz, E. H. Sargent, D. V. Talapin, *Science* **2016**, 353, 885.
- [15] H. Keum, Y. Jiang, J. K. Park, J. C. Flanagan, M. Shim, S. Kim, *ACS Nano* **2018**, 12, 10024–10031.
- [16] F. Prins, D. K. Kim, J. Cui, E. De Leo, L. L. Spiegel, K. M. McPeak, D. J. Norris, *Nano Letters* **2017**, 17, 1319–1325.
- [17] A. Capretti, A. Lesage, T. Gregorkiewicz, *ACS Photonics* **2017**, 4, 2187–2196.
- [18] T. S. Mentzel, D. D. Wanger, N. Ray, B. J. Walker, D. Strasfeld, M. G. Bawendi, M. A. Kastner, *Nano Letters* **2012**, 12, 4404–4408.
- [19] A. I. Ekimov, A. L. Efros, A. A. Onushchenko, *Solid State Communications* **1985**, 56, 921–924.
- [20] I. Moreels, Y. Justo, B. De Geyter, K. Haestraete, J. C. Martins, Z. Hens, *ACS Nano* **2011**, 5, 2004–2012.
- [21] C. Murray, D. J. Norris, M. G. Bawendi, *Journal of the American Chemical Society* **1993**, 115, 8706–8715.
- [22] B. M. Cossairt, *Chemistry of Materials* **2016**, 28, 7181–7189.
- [23] J. Park, J. Joo, G. K. Soon, Y. Jang, T. Hyeon, *Angewandte Chemie* **2007**, 46, 4630–4660.
- [24] M. A. Boles, D. Ling, T. Hyeon, D. V. Talapin, *Nat Mater* **2016**, 15, 141–153.
- [25] G. Kalyuzhny, R. W. Murray, *Journal of Physical Chemistry B* **2005**, 109, 7012–7021.
- [26] P. R. Brown, D. Kim, R. R. Lunt, N. Zhao, M. G. Bawendi, J. C. Grossman, V. Bulović, *ACS Nano* **2014**, 8, 5863–5872.
- [27] R. Wang, Y. Shang, P. Kanjanaboos, W. Zhou, Z. Ning, E. H. Sargent, *Energy & Environmental Science* **2016**, 9, 1130–1143.
- [28] N. Kirkwood, J. O. Monchen, R. W. Crisp, G. Grimaldi, H. A. Bergstein, I. Du Fossé, W. Van Der Stam, I. Infante, A. J. Houtepen, *Journal of the American Chemical Society* **2018**, 140, 15712–15723.

- [29] O. Chen, J. Zhao, V. P. Chauhan, J. Cui, C. Wong, D. K. Harris, H. Wei, H. S. Han, D. Fukumura, R. K. Jain, M. G. Bawendi, *Nature Materials* **2013**, *12*, 445–451.
- [30] J. J. Geuchies, B. Brynjarsson, G. Grimaldi, S. Gudjonsdottir, W. Van Der Stam, W. H. Evers, A. J. Houtepen, *ACS Nano* **2021**, *15*, 377–386.
- [31] D. Li, X. Zhang, M. Ramzan, K. Gu, Y. Chen, J. Zhang, B. Zou, H. Zhong, *Chemistry of Materials* **2020**, *32*, 6650–6656.
- [32] K. Wu, Y. S. Park, J. Lim, V. I. Klimov, *Nature Nanotechnology* **2017**, *12*, 1140–1147.
- [33] A. Kojima, K. Teshima, T. Miyasaka, Y. Shirai, *Proc. 210th ECS Meeting* **2006**.
- [34] J. Jeong et al., *Nature* **2021**, *592*, 381.
- [35] K. Yoshikawa, H. Kawasaki, W. Yoshida, T. Irie, K. Konishi, K. Nakano, T. Uto, D. Adachi, M. Kanematsu, H. Uzu, K. Yamamoto, *Nature Energy* **2017**, *2*, 1–8.
- [36] M. V. Kovalenko, L. Protesescu, M. I. Bodnarchuk, *Science* **2017**, *358*, 745–750.
- [37] L. Protesescu, S. Yakunin, M. I. Bodnarchuk, F. Krieg, R. Caputo, C. H. Hendon, R. X. Yang, A. Walsh, M. V. Kovalenko, *Nano Letters* **2015**, *15*, 3692–3696.
- [38] N. Mondal, A. De, A. Samanta, *ACS Energy Letters* **2019**, *4*, 32–39.
- [39] L. N. Quan, R. Quintero-Bermudez, O. Voznyy, G. Walters, A. Jain, J. Z. Fan, X. Zheng, Z. Yang, E. H. Sargent, *Advanced Materials* **2017**, *29*, 1605945.
- [40] F. Liu, Y. Zhang, C. Ding, S. Kobayashi, T. Izuishi, N. Nakazawa, T. Toyoda, T. Ohta, S. Hayase, T. Minemoto, K. Yoshino, S. Dai, Q. Shen, *ACS Nano* **2017**, *11*, 10373–10383.
- [41] S. Ten Brinck, I. Infante, *ACS Energy Letters* **2016**, *1*, 1266–1272.
- [42] Z. Liang, S. Zhao, Z. Xu, B. Qiao, P. Song, D. Gao, X. Xu, *ACS Applied Materials and Interfaces* **2016**, *8*, 28824–28830.
- [43] S. Sun, D. Yuan, Y. Xu, A. Wang, Z. Deng, *ACS Nano* **2016**, *10*, 3648–3657.

- [44] H. Hu, L. Wu, Y. Tan, Q. Zhong, M. Chen, Y. Qiu, D. Yang, B. Sun, Q. Zhang, Y. Yin, *Journal of the American Chemical Society* **2018**, *140*, 406–412.
- [45] H. Liu, Y. Tan, M. Cao, H. Hu, L. Wu, X. Yu, L. Wang, B. Sun, Q. Zhang, *ACS Nano* **2019**, *13*, 5366–5374.
- [46] D. Zhou, D. Liu, G. Pan, X. Chen, D. Li, W. Xu, X. Bai, H. Song, *Advanced Materials* **2017**, *29*, 1704149.
- [47] R. A. Lawson, A. P. Robinson, *Overview of materials and processes for lithography*, Vol. 11, Elsevier, **2016**, pp. 1–90.
- [48] G. E. Moore, *Electronics* **1965**, *4*, 114.
- [49] G. Moore, *IEEE International Electron Devices Meeting* **1975**, *21*, 11–13.
- [50] Y. Chen, *Microelectronic Engineering* **2015**, *135*, 57–72.
- [51] S. Chakrabarty, C. Sarma, L. Li, E. P. Giannelis, C. K. Ober in *SPIE Advanced Lithography*, International Society for Optics and Photonics, **2014**, pp. 90481C–90481C–5.
- [52] Y. Zhang, J. Haitjema, M. Baljozovic, M. Vockenhuber, D. Kazazis, A. Jung, Y. Ekinici, A. M. Brouwer, *Journal of Photopolymer Science and Technology* **2018**, *31*, 249–255.
- [53] H. H. Solak, *Journal of Physics D: Applied Physics* **2006**, *39*, R171–R188.
- [54] J. Shin, G. Han, Y. Ma, K. Moloni, F. Cerrina, *Journal of Vacuum Science & Technology B: Microelectronics and Nanometer Structures* **2001**, *19*, 2890.
- [55] T. Kozawa, S. Tagawa, *Japanese Journal of Applied Physics* **2010**, *49*, 30001.
- [56] S. F. Chini, A. Amirfazli, *Langmuir* **2010**, *26*, 13707–13714.
- [57] C. Wagner, N. Harned, *Nature Photonics* **2010**, *4*, 24–26.
- [58] J. Mulkens, M. Hanna, H. Wei, V. Vaenkatesan, H. Megens, D. Slotboom in *Extreme Ultraviolet (EUV) Lithography VI*, Vol. 9422, (Eds.: O. R. Wood, E. M. Panning), SPIE, **2015**, 94221Q.
- [59] TCMC, TSMC's N7+ Technology is First EUV Process Delivering Customer Products to Market in High Volume, **2019**, <https://pr.tsmc.com/english/news/2010>.

- [60] J. Jiang, D. De Simone, G. Vandenberghe in *Advances in Patterning Materials and Processes XXXIV, Vol. 10146*, (Eds.: C. K. Hohle, R. Gronheid), SPIE, **2017**, 101460A.
- [61] E. Reichmanis, F. M. Houlihan, T. X. Neenan, *Reviews Chemical Amplification Mechanisms for Microlithography*, tech. rep., **1991**, pp. 394–407.
- [62] J. A. Moore, J. O. Choi, *Degradation of poly (methyl methacrylate), deep UV, X-ray, electron-beam, and proton-beam irradiation*, American Chemical Society, **1991**, Chapter 11, pp. 156–192.
- [63] J. Passarelli, M. Murphy, R. Del Re, M. Sortland, L. Dousharm, M. Vockenhuber, Y. Ekinici, M. Neisser, D. A. Freedman, R. L. Brainard in *Advances in Patterning Materials and Processes XXXII, Vol. 9425*, (Eds.: T. I. Wallow, C. K. Hohle), SPIE, **2015**, 94250T.
- [64] R. Fallica, J. Haitjema, L. Wu, S. Castellanos, F. Brouwer, Y. Ekinici in *Extreme Ultraviolet (EUV) Lithography VIII, Vol. 10143*, (Eds.: E. M. Panning, K. A. Goldberg), SPIE, **2017**, 101430A.
- [65] C. Ober, E. Giannelis, *SPIE newsroom* **2014**, DOI [10.1117/2.1201409.005552](https://doi.org/10.1117/2.1201409.005552).
- [66] L. Li, S. Chakrabarty, K. Spyrou, C. K. Ober, E. P. Giannelis, *Chemistry of Materials* **2015**, 27, 5027–5031.
- [67] H.-H. Park, W. L. Law, X. Zhang, S.-Y. Hwang, S. H. Jung, H.-B. Shin, H. K. Kang, H.-H. Park, R. H. Hill, C. K. Ko, *ACS Applied Materials & Interfaces* **2012**, 4, 2507–2514.
- [68] J. Haitjema, Y. Zhang, M. Vockenhuber, D. Kazazis, Y. Ekinici, A. M. Brouwer, *Journal of Micro/Nanolithography MEMS and MOEMS* **2017**, 16, 1.
- [69] L. Wu, M. Tiekink, A. Giuliani, L. Nahon, S. Castellanos, *Journal of Materials Chemistry C* **2019**, 7, 33–37.
- [70] D. Qin, Y. Xia, B. Xu, H. Yang, C. Zhu, G. M. Whitesides, *Advanced Materials* **1999**, 11, 1433–1437.
- [71] S. Jaffar, K. T. Nam, A. Khademhosseini, J. Xing, R. S. Langer, A. M. Belcher, *Nano Letters* **2004**, 4, 1421–1425.

- [72] J. Y. Kim, C. Ingrosso, V. Fakhfour, M. Striccoli, A. Agostiano, M. L. Curri, J. Brugger, *Small* **2009**, *5*, 1051–1057.
- [73] M. Tamborra, M. Striccoli, M. L. Curri, J. A. Alducin, D. Mecerreyes, J. A. Pomposo, N. Kehagias, V. Reboud, C. M. Sotomayor Torres, A. Agostiano, *Small* **2007**, *3*, 822–828.
- [74] R. Platel, E. Palteau, L. Vaure, S. Raffy, F. Guérin, C. Nayral, F. Delpech, L. Ressler, *ACS Applied Nano Materials* **2021**, *2021*, 3544.
- [75] V. Nandwana, C. Subramani, Y.-C. Yeh, B. Yang, S. Dickert, M. D. Barnes, M. T. Tuominen, V. M. Rotello, *Journal of Materials Chemistry* **2011**, *21*, 16859.
- [76] F. Palazon, Q. A. Akkerman, M. Prato, L. Manna, *ACS Nano* **2016**, *10*, 1224–30.
- [77] Y. Wang, I. Fedin, H. Zhang, D. V. Talapin, *Science* **2017**, *357*, 385–388.
- [78] Y. Wang, J. A. Pan, H. Wu, D. V. Talapin, *ACS Nano* **2019**, *13*, 13917–13931.
- [79] D. B. Dement, M. K. Quan, V. E. Ferry, *ACS Applied Materials & Interfaces* **2019**, *11*, 14970–14979.
- [80] J. Torok, R. Del Re, H. Herbol, S. Das, I. Bocharova, A. Paolucci, L. E. Ocola, C. Ventrice Jr., E. Lifshin, G. Denbeaux, R. L. Brainard, *Journal of Photopolymer Science and Technology* **2013**, *26*, 625–634.
- [81] W. Haynes, D. R. Lide, T. J. Bruno, *CRC Handbook of Chemistry and Physics - Reference Book of Chemical and Physical Data*, 97th, (Ed.: W. Haynes), CRC Press, Boca Raton, **2017**, pp. 9–79 –9–80.
- [82] A. Narasimhan, L. Wisehart, S. Grzeskowiak, L. E. Ocola, G. Denbeaux, R. L. Brainard, *Journal of Photopolymer Science and Technology* **2017**, *30*, 113–120.
- [83] E. C. Mattson, Y. Cabrera, S. M. Rupich, Y. Wang, K. A. Oyekan, T. J. Mustard, M. D. Halls, H. A. Bechtel, M. C. Martin, Y. J. Chabal, *Chemistry of Materials* **2018**, *30*, 6192–6206.

- [84] L. Wu, M. Baljovic, G. Portale, D. Kazazis, M. Vockenhuber, T. Jung, Y. Ekinici, S. Castellanos Ortega, *Journal of Micro/Nanolithography MEMS and MOEMS* **2019**, *18*, 013504.
- [85] L. Zhang, R. He, H. C. Gu, *Applied Surface Science* **2006**, *253*, 2611–2617.
- [86] A. R. Smith, W. Yoon, W. B. Heuer, S. I. M. Baril, J. E. Boercker, J. G. Tischler, E. E. Foos, *The Journal of Physical Chemistry C* **2012**, *116*, 6031–6037.
- [87] M. H. Zarghami, Y. Liu, M. Gibbs, E. Gebremichael, C. Webster, M. Law, *Acs Nano* **2010**, *4*, 2475–2485.
- [88] L. Robinet, M.-C. Corbeil, *Studies in Conservation* **2003**, *48*, 23–40.
- [89] B. Smith, *Infrared Spectral Interpretation - A Spectral Approach*, CRC Press, Boca Raton, **1999**, pp. 31–66.
- [90] S. Maganov, V. Elings, M.-H. Whangbo, *Surface Science* **1997**, *375*, L385–L391.
- [91] C. A. Mack, *Journal of The Electrochemical Society* **1987**, *134*, 148.
- [92] C. R. Kagan, C. B. Murray, M. G. Bawendi, *Physical review. B Condensed matter* **1996**, *54*, 8633–8643.
- [93] C. R. Kagan, C. B. Murray, M. Nirmal, M. G. Bawendi, *Physical Review Letters* **1996**, *76*, 1517–1520.
- [94] S. A. Crooker, J. A. Hollingsworth, S. Tretiak, V. I. Klimov, *Physical Review Letters* **2002**, *89*, 18–21.
- [95] K. Tai, W. Lu, I. Umezu, A. Sugimura, *Applied Physics Express* **2010**, *3*, 035202.
- [96] K. F. Chou, A. M. Dennis, *Sensors* **2015**, *15*, 13288–325.
- [97] Y.-H. Kim, J.-S. Heo, T.-H. Kim, S. Park, M.-H. Yoon, J. Kim, M. S. Oh, G.-R. Yi, Y.-Y. Noh, S. K. Park, *Nature* **2012**, *489*, 128–132.
- [98] K. J. Williams, W. A. Tisdale, K. S. Leschkies, G. Haugstad, D. J. Norris, E. S. Aydil, X.-Y. Zhu, *ACS Nano* **2009**, *3*, 1532–1538.

- [99] A. Van Dijken, A. H. Janssen, M. H. Smitsmans, D. Vanmaekelbergh, A. Meijerink, *Chemistry of Materials* **1998**, *10*, 3513–3522.
- [100] J. Jasieniak, L. Smith, J. van Embden, P. Mulvaney, M. Califano, *The Journal of Physical Chemistry C* **2009**, *113*, 19468–19474.
- [101] A. J. Houtepen, Z. Hens, J. S. Owen, I. Infante, *Chemistry of Materials* **2017**, *29*, 752–761.
- [102] R. Ihly, J. Tolentino, Y. Liu, M. Gibbs, M. Law, *ACS Nano* **2011**, *5*, 8175–8186.
- [103] I. S. Nikolaev, P. Lodahl, A. F. van Driel, A. F. Koenderink, W. L. Vos, *Physical Review B* **2007**, *75*, 115302.
- [104] G. Schlegel, J. Bohnenberger, I. Potapova, A. Mews, *Physical Review Letters* **2002**, *88*, 4.
- [105] B. R. Fisher, H. J. Eisler, N. E. Stott, M. G. Bawendi, *Journal of Physical Chemistry B* **2004**, *108*, 143–148.
- [106] B. C. Fitzmorris, J. K. Cooper, J. Edberg, S. Gul, J. Guo, J. Z. Zhang, *The Journal of Physical Chemistry C* **2012**, *116*, 25065–25073.
- [107] O. Schöps, N. Le Thomas, U. Woggon, M. V. Artemyev, *Journal of Physical Chemistry B* **2006**, *110*, 2074–2079.
- [108] D. A. R. Barkhouse, R. Debnath, I. J. Kramer, D. Zhitomirsky, A. G. Pattantyus-Abraham, L. Levina, L. Etgar, M. Grätzel, E. H. Sargent, *Advanced Materials* **2011**, *23*, 3134–3138.
- [109] R. K. Čapek, I. Moreels, K. Lambert, D. De Muynck, Q. Zhao, A. V. Tomme, F. Vanhaecke, Z. Hens, *J. Phys. Chem. C* **2010**, *114*, 6371–6376.
- [110] J. Mooney, P. Kambhampati, *Journal of Physical Chemistry Letters* **2013**, *4*, 3316–3318.
- [111] A. Javier, D. Magana, T. Jennings, G. F. Strouse, *Applied Physics Letters* **2003**, *83*, 1423.
- [112] K. Gong, J. E. Martin, L. E. Shea-Rohwer, P. Lu, D. Kelley, A. F., *Journal of Physical Chemistry C* **2015**, *119*, 2231–2238.

- [113] M. T. Reetz, M. Winter, G. Dumpich, J. Lohau, S. Friedrichowski, *Journal of the American Chemical Society* **1997**, *119*, 4539–4540.
- [114] T. R. Bedson, R. E. Palmer, T. E. Jenkins, D. J. Hayton, J. P. Wilcoxon, *Applied Physics Letters* **2001**, *78*, 1921–1923.
- [115] F. Palazon, M. Prato, L. Manna, *Journal of the American Chemical Society* **2017**, *139*, 13250–13259.
- [116] R. E. Bailey, S. Nie, *Journal of the American Chemical Society* **2003**, *125*, 7100–7106.
- [117] S. J. Lim, M. U. Zahid, P. Le, L. Ma, D. Entenberg, A. S. Harney, J. Condeelis, A. M. Smith, *Nature communications* **2015**, *6*, 1–10.
- [118] Q. A. Akkerman, V. D’Innocenzo, S. Accornero, A. Scarpellini, A. Petrozza, M. Prato, L. Manna, *Journal of the American Chemical Society* **2015**, *137*, 10276–10281.
- [119] O. Vybornyi, S. Yakunin, M. V. Kovalenko, *Nanoscale* **2016**, *8*, 6278–6283.
- [120] L. Protesescu, S. Yakunin, S. Kumar, J. Bär, F. Bertolotti, N. Masciocchi, A. Guagliardi, M. Grotevent, I. Shorubalko, M. I. Bodnarchuk, C. J. Shih, M. V. Kovalenko, *ACS Nano* **2017**, *11*, 3119–3134.
- [121] A. Wang, Y. Guo, F. Muhammad, Z. Deng, *Chemistry of Materials* **2017**, *29*, 6493–6501.
- [122] J. Zhang, Q. Wang, X. Zhang, J. Jiang, Z. Gao, Z. Jin, S. Liu, *RSC Advances* **2017**, *7*, 36722–36727.
- [123] M. Gong, R. Sakidja, R. Goul, D. Ewing, M. Casper, A. Stramel, A. Elliot, J. Z. Wu, *ACS Nano* **2019**, *13*, 1772–1783.
- [124] Q. Chen et al., *Nature* **2018**, *561*, 88–93.
- [125] J. H. Heo, D. H. Shin, J. K. Park, D. H. Kim, S. J. Lee, S. H. Im, *Advanced Materials* **2018**, *30*, 1801743.
- [126] B. Xin, Y. Pak, S. Mitra, D. Almalawi, N. Alwadai, Y. Zhang, I. S. Roqan, *ACS Applied Materials and Interfaces* **2019**, *11*, 5223–5231.
- [127] X. Huang, Q. Guo, S. Kang, T. Ouyang, Q. Chen, X. Liu, Z. Xia, Z. Yang, Q. Zhang, J. Qiu, G. Dong, *ACS Nano* **2020**, *14*, 3150–3158.

- [128] W. Zhan, L. Meng, C. Shao, X.-g. Wu, K. Shi, H. Zhong, *ACS Photonics* **2021**, *8*, 765–770.
- [129] Y. Altintas, I. Torun, A. F. Yazici, E. Beskazak, T. Erdem, M. Serdar Onses, E. Mutlugun, *Chemical Engineering Journal* **2020**, *380*, 122493.
- [130] D. Xing, C.-C. Lin, Y.-L. Ho, A. S. A. Kamal, I.-T. Wang, C.-C. Chen, C.-Y. Wen, C.-W. Chen, J.-J. Delaunay, *Advanced Functional Materials* **2021**, *31*, 2006283.
- [131] C. Zou, C. Chang, D. Sun, K. F. Böhringer, L. Y. Lin, *Nano Letters* **2020**, *20*, 3710–3717.
- [132] L. Meng, J. You, Y. Yang, *Nature Communications* **2018**, *9*, 1–4.
- [133] C. Lu, M. W. Wright, X. Ma, H. Li, D. S. Itanze, J. A. Carter, C. A. Hewitt, G. L. Donati, D. L. Carroll, P. M. Lundin, S. M. Geyer, *Chemistry of Materials* **2019**, *31*, 62–67.
- [134] C. D. Dieleman, W. Ding, L. Wu, N. Thakur, I. Bepalov, B. Daiber, Y. Ekinici, S. Castellanos, B. Ehrler, *Nanoscale* **2020**, *12*, 11306–11316.
- [135] S. A. Mann, B. Sciacca, Y. Zhang, J. Wang, E. Kontoleta, H. Liu, E. C. Garnett, *ACS Nano* **2017**, *11*, 1412–1418.
- [136] X. Li, Y. B. Zhao, F. Fan, L. Levina, M. Liu, R. Quintero-Bermudez, X. Gong, L. N. Quan, J. Fan, Z. Yang, S. Hoogland, O. Voznyy, Z. H. Lu, E. H. Sargent, *Nature Photonics* **2018**, *12*, 159–164.
- [137] H. Shen, Q. Gao, Y. Zhang, Y. Lin, Q. Lin, Z. Li, L. Chen, Z. Zeng, X. Li, Y. Jia, S. Wang, Z. Du, L. S. Li, Z. Zhang, *Nature Photonics* **2019**, *13*, 192–197.
- [138] J. Roh, Y. S. Park, J. Lim, V. I. Klimov, *Nature Communications* **2020**, *11*, 1–10.
- [139] X. Brokmann, G. Messin, P. Desbiolles, E. Giacobino, M. Dahan, J. P. Hermier, *New Journal of Physics* **2004**, *6*, 1–8.
- [140] V. I. Klimov, A. A. Mikhailovsky, D. McBranch, C. A. Leatherdale, M. G. Bawendi, *Science* **2000**, *287*, 1011–1013.
- [141] O. V. Kozlov, Y. S. Park, J. Roh, I. Fedin, T. Nakotte, V. I. Klimov, *Science* **2019**, *365*, 672–675.

- [142] D. Vanmaekelbergh, A. J. Houtepen, J. J. Kelly, *Electrochimica Acta* **2007**, 53, 1140–1149.
- [143] C. Dang, J. Lee, C. Breen, J. S. Steckel, S. Coe-Sullivan, A. Nurmikko, *Nature Nanotechnology* **2012**, 7, 335–339.
- [144] M. M. Adachi, F. Fan, D. P. Sellan, S. Hoogland, O. Voznyy, A. J. Houtepen, K. D. Parrish, P. Kanjanaboos, J. A. Malen, E. H. Sargent, *Nature Communications* **2015**, 6, 1–8.
- [145] J. S. van der Burgt, C. D. Dieleman, E. Johlin, J. J. Geuchies, A. J. Houtepen, B. Ehrler, E. C. Garnett, *ACS Photonics* **2021**, 8, 1143–1151.

SUMMARY

Colloidal quantum dots (CQDs) and other semiconductor (SC) nanocrystals (NCs), like perovskites, are nanosized semiconductor particles with a tunable bandgap and interesting optical properties. CQD and other SC NCs, have been an active field of research for several decades because of their versatility in terms of synthesis and application. As solution-processable, tunable semiconductor, CQDs and NCs have been envisioned for numerous applications ranging from active material and stabilizer in photovoltaics, spectral downshifting for solar and display technologies, photodetectors and lasers, among others, some of which are already commercial mass products. The tunability of NCs makes it relatively easy to optimize the material to the intended application in terms of bandgap, absorption, emission wavelength, conductivity, charge transfer and compatibility with different surrounding materials and chemical environments. At the same time, patterning these nanocrystals at the nanoscale could add another knob to turn in order to expand the usability of CQDs or improve their performance. In this thesis we present work on patterning of CQDs and NCs with several lithographic techniques.

Chapter 1 starts with an introduction to quantum dots, nanocrystals and lithography. We cover the basics of the synthesis of II-VI CQDs as well as perovskite NCs. We introduce some of their applications and provide insight in the current landscape of patterned NCs. Next to this, we cover some fundamentals of lithography, both in the form of deep-ultraviolet lithography (DUVL) and extreme-ultraviolet lithography (EUVL) as well as electron-beam lithography (EBL).

In **Chapter 2** we demonstrate a general one-step nanopatterning technique for as-synthesized PbS and CdSe CQDs with advanced photolithography. We find we can use both relatively low energy photons (from 5.5 eV), as well as higher energy EUV photons (91.9 eV) for patterning features as small as 60 nm directly.

We find that the solubility change is achieved by cross-linking the organic ligands, to create a cohesive CQD film. Required doses are relatively low and, in the order of commercial state-of-the-art patterning materials ($\sim 120 \text{ mJ cm}^{-2}$) for EUV. The exposure to EUV photons, even to relatively high doses, does not significantly affect the luminescent properties, which allows for fabrication of luminescent structures directly.

In **Chapter 3** we expand on our patterning of PbS and CdSe CQDs with e-beam-based lithography techniques as well. We find that low-energy electrons (from 3 eV) can already be used to induce insolubility reactions to pattern CQDs, yet with high electron beam dose. Highly-energetic electrons (50 keV) from commercial EBL systems allow for patterning at much lower doses. Doses on the order of several hundred $\mu\text{C cm}^{-2}$ are sufficient to induce the patterning mechanism. This dose is in the same range as commercial state-of-the-art e-beam resists. From time correlated single photon counting (TCSPC) and photoluminescence (PL) experiments we find that luminescent properties seem to be relatively unaffected by the exposure. The intricate designs that are unlocked by EBL finally allows us to create a luminescent microscale version of the famous painting *Girl with the Pearl Earring* by Johannes Vermeer.

Chapter 4 covers another extension of the technique in terms of a different materials class: perovskites. We pattern CsPbBr_3 NCs via EBL into different designs. We find it is possible to create features around 100 nm and we can pattern the nanocrystals with high precision in elaborate designs. We observe a reduction of photoluminescence quantum yield (PLQY) of the material after processing, but luminescence is nonetheless bright and radiative decay is relatively stable. We attribute the patterning mechanism to cross-linking of the surface ligands as elucidated by Fourier transform infrared spectroscopy (FTIR). The amine ligands, however, seem to partially detach from the crystal, thereby reducing the passivation.

In the final **Chapter 5** we use our patterning technique for a light emission application. We fabricate waveguiding structures

patterned from emitters directly. The direct EBL described in **Chapter 2** is a suitable fabrication technique to pattern colloidal CQDs into optical surfaces, like Bragg gratings, to manipulate light emission. We show control over the angle of emission and that a standing wave for out-of-plane emission forms in the CQD grating. We show that the patterned film can be charged but so far no lasing was observed. Optical simulations show that in our system losses are currently too high. We need to adjust our system further, for instance with index engineering, as the current structure does not confine the optical mode enough inside the emitter.

SAMENVATTING

Colloïdale kwantumdeeltjes (CKD's) en andere halfgeleider nanokristallen (NK's), zoals perovskieten, zijn halfgeleider deeltjes op nanoschaal met een aan te passen bandkloof en interessante optische eigenschappen. CKD's en halfgeleider NK's vormen een actief onderzoeksveld voor meerdere decennia door hun veelzijdigheid op gebied van synthese en toepassingen. Door de eenvoudige verwerkbaarheid in oplossing en de aanpasbaarheid van deze halfgeleiders, hebben kwantumdeeltjes en NK's talloze toepassingen gevonden, variërend van actieve materialen of stabilisator in fotonvoltaïsche cellen, materiaal voor spectrale verschuiving voor zonnecel- en displaytechnologiën, fotodetectoren en lasers. De eerdergenoemde aanpasbaarheid van NK's maakt het relatief eenvoudig om het materiaal te optimaliseren voor de voorgenomen toepassing op het gebied van de bandkloof, absorptie, emissiegolflengte, geleidbaarheid, ladingsoverdracht en compatibiliteit met verschillende materialen en chemische omgevingen. Tegelijkertijd kan het vormen van patronen uit deze kristallen op nanoschaal een nieuwe knop toevoegen om aan te draaien ter uitbreiding van de functionaliteit of de toename van de prestaties van CKD's. In dit proefschrift presenteren wij werk op het gebied van het vormen van patronen uit CKD's en NK's met verschillende lithografische technieken.

Hoofdstuk 1 begint met een introductie over kwantumdeeltjes, nanokristallen en lithografie. We beschrijven de basis van de synthese van II-VI CKD's, evenals perovskiet NK's. We introduceren enkele toepassingen en geven inzicht in het huidige landschap van het vormen van patronen uit NK's. Hiernaast beschrijven we enkele fundamentele principes van lithografie, zowel in de vorm van optische diep-ultraviolet (DUV)-lithografie en extreem-ultraviolet (EUV)-lithografie als elektronenbundellithografie (EBL).

In **Hoofdstuk 2** demonstreren we een algemene techniek voor het creëren van nanopatronen uit eenvoudig gesynthetiseerde PbS en CdSe kwantumdeeltjes in een enkele productiestap met geavanceerde fotolithografie. We vinden dat we zowel fotonen met een relatief lage energie (vanaf 5.5 eV), als hoger energetische EUV-fotonen (91.9 eV) kunnen gebruiken om structuren te fabriceren die zo klein kunnen zijn als 60 nm. We vinden dat er een wisseling in oplosbaarheid plaatsvindt door vernetting van de organische liganden, waarmee een samenhangende KD-laag wordt gevormd. De benodigde doses zijn relatief laag en van dezelfde orde grootte ($\sim 120 \text{ mJ cm}^{-2}$) als moderne commerciële materialen die zijn ontworpen voor het creëren van nanopatronen. De blootstelling aan EUV-fotonen beïnvloedt de luminescente eigenschappen van de materialen niet significant, zelfs niet bij hoge doses, waardoor het mogelijk wordt om op een directe manier luminiscente structuren te maken.

In **Hoofdstuk 3** breiden we het vormen van patronen uit PbS and CdSe CKD's verder uit met elektronenbundellithografie-technieken. We vinden dat laag-energetische elektronen (vanaf 3 eV) al gebruikt kunnen worden om reacties te veroorzaken die de oplosbaarheid van de NK's verandert. Bij het gebruik van laag-energetische elektronen zijn echter hoge elektrondoses vereist. Het mechanisme voor patroonvorming wordt ook geïnduceerd door hoog-energetische elektronen (50 keV) van commerciële elektronenbundellithographiesystemen. In dit geval volstaan veel lagere doses, in de orde van enkele honderden $\mu\text{C cm}^{-2}$. Dit is vergelijkbaar met commerciële resistmaterialen. Uit tijdopgeloste en stabiele-toestandfotoluminescentie-experimenten vinden we dat de luminescente eigenschappen relatief ongemoeid blijven door de blootstelling aan de elektronenbundel. Omdat EBL het fabriceren van zeer ingewikkelde ontwerpen ontsluit, is het mogelijk om een luminescente microversie te fabriceren van het beroemde schilderij *Het Meisje met de Parel* van Johannes Vermeer.

Hoofdstuk 4 omvat wederom een uitbreiding op onze techniek, door het gebruik van een nieuw klasse materialen: perovskieten. We vormen patronen uit CsPbBr_3 NK's met EBL in verschillende ontwerpen. Het is mogelijk om structuren te maken zo klein als

100 nm en kunnen deze structuren met grote precisie plaatsen, waardoor we ingewikkelde ontwerpen kunnen fabriceren. We observeren een afname in de fotoluminescentiekwantumopbrengst van het materiaal na het fabricageproces, maar luminescentie is niettemin helder en stralend verval is relatief stabiel. We schrijven het mechanisme voor patroonvorming toe aan vernetting van de liganden, zoals Fourier Transformatie Infrarood Spectroscopie aan het licht brengt. De amineliganden lijken ook deels van de kristaloppervlakte gescheiden, waardoor de passivatie van de kristallen afneemt.

In het laatste **Hoofdstuk 5** passen we onze patroonfabricage toe om lichtemissie te beïnvloeden. We fabriceren een lichtgeleidende structuur van een emitterend materiaal zelf. De directe EBL-methode die is beschreven in **Hoofdstuk 2** is een geschikt procedé voor het vormen van CKD's in optische structuren, zoals Braggroosters, om lichtemissie mee te manipuleren. We laten zien dat we controle hebben over de emissiehoek van de lichtbundel en dat een staande golf wordt gevormd die zorgt voor een directionele bundel loodrecht op de structuur. Het materiaal kan ook elektrochemisch worden opgeladen om de drempel voor optische versterking te verlagen, maar tot op heden zien we geen lasing. Optische simulaties laten zien dat er in ons huidige systeem teveel verliezen zijn. Het systeem zou verder geoptimaliseerd kunnen worden, bijvoorbeeld door indexoptimalisatie, om de optische modus beter in het emitterende materiaal te begrenzen.

LIST OF PUBLICATIONS

The chapters of this thesis are based on the following publications:

- [1] **Dieleman, C. D.**, Ding, W., Wu, L., Thakur, N., Bespalov, I., Daiber, B., Ekinici, Y., Castellanos, S. & Ehrler, B. "Universal direct patterning of colloidal quantum dots by (extreme) ultraviolet and electron beam lithography", *Nanoscale* **2020** 12(20), 11306-11316
- [2] **Dieleman, C. D.**, van der Burgt, J., Garnett, E.C. & Ehrler, B. "Direct patterning of CsPbBr₃ nanocrystals with electron-beam lithography" (*in preparation*)
- [3] **Dieleman, C. D.**, Kolkowski, R., Pal, D., Geuchies, J.J., van der Burgt, J., Garnett, E.C., Houtepen, A.J., Koenderink, A.F. & Ehrler, B. "Directly patterned, electrochemically charged colloidal quantum dots for lasing devices" (*in preparation*)

Other publications by the author:

- [4] van der Burgt, J. S., **Dieleman, C. D.**, Johlin, E., Geuchies, J. J., Houtepen, A. J., Ehrler, B., & Garnett, E. C. "Integrating sphere Fourier microscopy of highly directional emission", *ACS Photonics* **2021** 8(4), 1143–1151
- [5] Doleman, H. M., **Dieleman, C. D.**, Mennes, C., Ehrler, B., & Koenderink, A. F. "Observation of cooperative Purcell enhancements in antenna–cavity hybrids", *ACS Nano* **2020** 14(9), 12027-12036
- [6] Muscarella, L. A., Hutter, E. M., Sanchez, S., **Dieleman, C. D.**, Savenije, T. J., Hagfeldt, A., Saliba, M., & Ehrler, B. "Crystal orientation and grain size: do they determine optoelectronic properties of MAPbI₃ perovskite?", *The Journal of Physical Chemistry Letters* **2019** 10(20), 6010-6018

- [7] **Dieleman, C. D.**, Denissen, P. J., & Garcia, S. J. "Long-term active corrosion protection of damaged coated AA2024-T3 by embedded electrospun inhibiting nanonetworks", *Advanced Materials Interfaces* **2018** 5(12), 1800176

ACKNOWLEDGMENTS

It is done. Finally finished. My PhD has been a tremendously eventful period of my life. One I look back on with a mix of emotions. It has been a time full of interesting challenges, discovery of the unknown, larger and smaller victories and wonderful new encounters. At the same time, there have also been times where it felt lonely, or where doubts and fears could feel overwhelming. Overall though, looking back on where I started 4 years ago, and where I am now, both on a professional and a personal level, I cannot conclude otherwise than that I have matured in the way I see the world and will tackle new challenges ahead. It has been, without a doubt, the hardest thing I have ever done, but I can look back proudly on the final result. Of course, I could not have managed to do so without the many people, whose contributions, big or small, along the way have helped me in completing this book. I am incredibly thankful to all of you and would like to thank you for your support.

First of all, my supervisor and promotor Bruno Ehrler. I am eternally grateful for the opportunity you have given me to do a PhD at a place as wonderful as AMOLF and the trust you have put in hiring an engineer for a physics project. You have built a wonderful research group and I hope I have met the standard I see with the rest of our group. I have thoroughly enjoyed our time together. You are a great mentor, as you were always supportive, gave me the opportunity to explore on my own and put things in perspective when I seemed to lose track of the bigger picture in my professional or personal life. It was also great to have seen you grow in your role as the group became more mature. I hope we will keep in touch in the future.

My second promotor, Albert Polman, I want to thank for always being interested and enthusiastic about my work. Although your role was more hands-off, you were always up-to-date and supportive. You have built LMPV to be a wonderful environment to work and your tireless enthusiasm for good science, as well as

your constant reminders of the impact of our work in society are contagious and very inspirational.

I also want to thank my co-promotor Sonia Castellanos Ortega. Although our collaboration through ARCNL came to a somewhat abrupt end, it was great to work with you. You were often more excited than I was, and seeing you literally jump with joy or audibly gasp after a good result was a great motivator.

More thanks go out to Fred Brouwer from ARCNL and Wim van de Zande and Sander Wuister from ASML, who were also involved in the project at the start. Your input is valued greatly.

The best part of the last 4 years was working on a day-to-day basis with the friendly and wonderful people of the Hybrid Solar Cells group. As mentioned before, I can only hope to have met the standard I see with all of you. I want to thank you all in no particular order. Benjamin Daiber, you were a fantastic office mate for almost 4 years and have grown to be a wonderful friend over the years. Thank you for your patience in teaching me several physics concepts, coming up with Mathematica functions and have encouraging words when I ran into barriers professionally or personally. I also valued our discussions on the bigger and smaller problems in the world, whether it was German car manufacturers getting away with Dieselgate, the looming Covid-19 pandemic, Dutch politics or the added value of a coffee sock over a paper filter. I hope you find the place where you can make the world a little bit better. Loreta Muscarella, you are a talented scientist and a good friend. Thank you for turning me a little bit Sicilian. I will keep making your recipes and thank you for teaching me how to voice my frustrations in Italian, "*Madonna*". Don't ever lose your drive and passion, they make you unstoppable! Lucie McGovern, thank you for always being kind, cheerful and supportive. Guilty Pleasure Fridays in the lab were amazing and thanks for letting me crash when I needed to move last minute. Moritz Futscher, thank you for being such a great mentor and helpful and friendly colleague in- and outside the lab. Seeing you work was an absolute inspiration. Silvia Ferro, it was nice to work with you and hope you are able to thrive in the group. Imme Schuringa, it was so great to see you bring your energy to the group, even though you started at the hardest time possible.

I am sure you will come out on top. Tianyi Wang, thanks for your help in the lab and with asking many critical questions in the group meeting. Eline Hutter, it was amazing to have you in the group. With your passion and determination you are a role model and inspiration for any researcher. Gianluca Grimaldi, I am very thankful for all the things you taught me about quantum dots and it was great to be able to share and discuss doubts when the future seemed unpredictable. Thanks to Jumin Lee for always being a great co-worker in the lab. It was great to learn a lot about Korea and hear about your European travel adventures. Moritz Schmidt, Jeroen de Boer and María Gélvez-Rueda, although we did not work long together, it was a pleasure to meet you, you are great additions to the group. Weiyi Ding, the master student I supervised, although the project turned out to be hard, I am happy and proud we were able to finish and even partly publish it. I think we both learned a lot during that time and I wish you the best for the next step. Ruirt Bosma, thanks for teaching me how to make quantum dots. Stefan Tabernig, Joris Bodin, Emil Kensington and David Langhorst, you were great office mates and fun to discuss science or random things with. Koen van der Hoven, Merlinde Wobben, Marnix Ackermans, Isabel Koschany, Toon Maassen, Rens van Roosmalen, Jouke Blom, Andrea Pollastri, Merlijn Kersten, Hsiu-Min Wu thanks for adding your energy and enthusiasm to the group. Last but not least, thanks to our lab technician Marc Duursma, for always keeping the lab running. You were always helpful and willing to look for better solutions and hunting down problems in the lab.

My project would not have been possible without the help of the great AMOLF staff both on the scientific and support side. I want to thank all the LMPV group leaders, Albert Polman, Bruno Ehler, Erik Garnett and Esther Allarcón - Lladó for creating an exciting, connected, open and collaborative environment to work. Special thanks to the other group leaders of the nanophotonics department, Femius Koenderink, Ewold Verhagen and Saïd Rodríguez for teaching me in other physics disciplines as well and supporting interesting collaborations. I also want to thank Joost Frenken for always staying connected in the collaborations between AMOLF and ARCNL and showing interest in my work. No

experimental scientist can do anything without proper technical support. Special thanks to the cleanroom staff, Hans Zeijlemaker, Dmitry Lamers, Igor Hoogsteder, Andries Lof and in particular Bob Drent. Your tireless help in the cleanroom and Nanolab was extremely valuable to get any scientific work done. And of course you were always brightening up the AMOLF BBQs and Christmas Lunches. I am also grateful for the help of the engineering department, mechanical workshop and electronics department, in particular Ricardo Struik, Niels Commandeur, Tom Brouwer, Jan van der Linden, Mark Willemse, Jan Zomerdijk, Niels Winkelaar and Iliya Cerjak with help ranging from cutting silicon wafers to 3D printing gifts for group members and helping creating wonderful centerpieces for the Christmas lunch. Thanks to Erny Lammers and Petra Vastenhouw for your limitless enthusiasm in telling the world about our work within the lab. Also thanks to all those people working in the background to make sure AMOLF runs as it should. The secretarial staff, Floortje van den Berg, Karelia Wrona, Henriëtte Langeveld and Teressa van der Linden without whom so many things would fall apart. Clyde Vliet and the rest of facilities for making sure we have a good working environment, the canteen staff for taking care of the coffee, the cleaning staff for ensuring we can always do our work in a clean environment, ICT that enabled us to do our daily work and quickly switch to home-office when it was demanded, HR for taking good care of all employees, Finance and Purchase for supporting our traveling and lab needs, Health and Safety for keeping us safe and of course the friendly faces of Juliette Essen-Hartings, Marjo Wijnands and Ad Winnubst at the reception desk, being representative for the welcoming environment that AMOLF is. Finally, Huib Bakker and Paula van Tijn, for managing the institute and creating a safe work environment, especially during the hard times in the pandemic.

I want to thank all the scientists I had the privilege to collaborate with. Jaco Geuchies and Arjan Houtepen thank you for being interested in the work I developed and starting an interesting collaboration with me that sparked so many more within AMOLF. I hope we can still get the result we were after. Radek Kolkowski, thanks for your patience in the lab and enthusiasm

for our work. I have learned a lot from you. Deba Pal, thanks for stepping in last-minute to make me understand my results a bit better. I hope I can return the favour to help you achieve your goals as well. Julia van der Burgt, it was a pleasure working with you and it was extremely satisfying we were able to finish the project before you became a mother! I am so glad my work was beneficial to someone else. To my first collaborator, Hugo Doeleman, I enjoyed working with you in my first attempt to pattern some quantum dots and I am happy my small contribution turned out to be useful. Michaela Vockenhuber and Yasin Ekin, thank you for the opportunity to attempt some crazy patterning experiments in the beamline at PSI. Special thanks to Yu Zhang, Lianjia Wu and Neha Thakur for all of your help at the beamline and dealing with all the samples I gave to you over the years. Ivan Beshpalov, thank you for your hard and enthusiastic work with my quantum dots in the LEEM.

The atmosphere at AMOLF is great, in large part due to the many social interactions made possible by the PV. Being part of that for two years was a great experience and I want to thank all the people I worked with. Thanks to Hans Hendrikse for being a bold and loud chairman and master of ceremonies, Lukas Helmbrecht, your creative ideas never cease to amaze me, thanks to Giorgio Oliveri for always being cheerful, Jente Vandersmissen for your boundless energy, Yorick Bleijer for your organized work and Loreta Muscarella for looking better in Cupid wings than I do. Yvonne Goos, thank you for sharing your good taste in music, Isabelle Palstra for your infectious, unmeasurable enthusiasm and creativity, Alexander Korotkevich for keeping everyone down to earth, Niels Commandeur for your unrelentless drive for perfecting physical props, Jeffrey den Haan for your leadership, Marnix Ackermans for adding a little bit of Delft student spirit in the mix, Wessel Zwart for coming up with bold ideas, Lennart van Buren for your hard work and Teresa van der Linden for always being enthusiastic, even if you had no time. I had such a good time with all of you and we organized some events we can be proud of!

Then there is so many people I have gotten to know over the years at AMOLF and ARCNL to a larger or lesser extend, that I am bound to forget someone. However, I want to thank Gede Adhyaksa, Parisa Khoram, Harshal Agrawal, Dónal van Uunen, Sarah Gillespie, Jian-Yao Zheng, Hongyu Sun, and Susan Rigter for being great lab mates, Sven Askes for proofreading and feedback and many research suggestions, Biplab Patra for teaching about nanocrystal synthesis, Jenny Kontoleta for adding cheer and good music taste to the lab, Kevin Cognée for helping with housing in Amsterdam, Tom Veeken for all the help with the Witec, Mark Aarts for help with the AFM, Olivier Lugier and Reinout Jaarsma for your help with the XPS. Annemarie Berkhout, Arno van der Weijden, Robin Buijs, Andrea Cordaro, Luuk van Laake, Matthias Liebrau, Marloes Bistervels, Kelly Mauser, Verena Neder, Nick Schilder, Jesse Slim, Magda Solá Garcia, Nasim Tavakoli, Marco Valenti, Nika van Nielen, Jarich Haijtema, Robbert Bloem, Najmeh Sadegh, Anniket Thete and so many others, I have enjoyed our conversations and encounters, short or long, at poster sessions, coffee breaks, borrels, BBQs, outings or on the dance floor of Physics Veldhoven.

Outside of work I also had many people that were supportive, interested in my work or allowed me to take my mind of. Alex Nederlof and Stuart Edelenbos, so much has changed in 4 years, are we finally adults now? I am glad you were around to help me through the ups and downs and make life a bit easier with a well-timed pun, delicious meal, awesome jam session, poorly-timed drum fill/blues scheme, or perfectly assembled Spotify playlist. And thank you for still being impressed by the term *quantum dot*. Thomas Neijenhuis thanks for all the musicality, inspiration to go running and your valuable help with moving to Amsterdam. Joris Roebroeks, Suzan Heijkoop, Doris van Hooijdonk, Boukje van Liempt, Joost Döbken, thanks for all the fun times with the Suits, musical or otherwise. Anne-Fleur Edelenbos, thank you for organizing amazing dinner parties. Ilse Roos, Tom Korporaal, Guus van Bohemen, Jerry de Knegt, thank you for asking me to play corny 90s music. I still hope we can one day perform. René Geelhoed, Jethro Steijvers, Julian Steijvers, Berend Kooijman, Stijn Tholhuijsen, Piter-Jan Goodijk thanks for still being

the weird bunch that I hung out with in high school. Maurits Kok, Bart Root thank you for the interesting conversations about life, the universe and everything in it. Paul Denissen, Wouter Post, Wouter Vogel, Arijana Suša, Kevin de Boom, Michael den Brabander, Bart Smeets, Kirk Schepers, Matěj Karasék, Jamie Junel, thank you for the fun times discussing life in research, the real world or some random stuff whether at the Atmosfeer, Beestenmarkt, online or anywhere else. Jeroen Mangelschots and Lara Fricke, it is great to still hang out with you after all those years, even though it has been tough to cross borders recently.

Finally, I am very grateful for the support of my family. Stephanie McGuire, Renee van Westreenen, Koos Jansen, thank you for including me in the family and making me feel supported. Dave McGuire and Maria McGrath, thank you for giving me an insight in Kimberly's American side of the family and making me feel at home at the other side of the world. To my sweet grandmother, it is very special being able to share this accomplishment with you. Thank you for always being interested and understanding. I am thankful for my amazing parents for always believing in me and supporting my choices. You have always told me to take the opportunities I get and utilize my potential. Thank you for living up to this and allowing me to take chances, even if that means being further apart. My lovely sister Lotte, thank you for your support and love. I hope you can be proud of your little brother. I am for sure proud of you and Guy, being amazing parents to sweet, little Blandine. Finally, my dearest Kimberly. You have always been my greatest supporter by letting me be myself. I could not have done this without knowing I could always lean on you. Your drive, determination and perseverance have always been an inspiration to me and you have pulled me through the roughest of times. It was difficult being separated in the middle of a pandemic, but it only made us stronger. I love you with all my heart and would follow you anywhere.

CURRICULUM VITAE

PERSONAL INFORMATION

Christian Dieleman
christiandieleman@outlook.com

17/01/1991 Born in Goes, NL

EDUCATION

2002 – 2008 Gymnasium
Buys Ballot College, Goes, NL

2008 – 2014 Bachelor of Science
Aerospace Engineering
Technische Universiteit Delft, NL

2014 – 2016 Master of Science
Aerospace Engineering, Novel Aerospace Materials
Technische Universiteit Delft, NL
Thesis *Active corrosion protection of AA2024-T3
by inhibitor loaded electrospun nanofibers*
Supervisor *Dr. S. J. Garcia*

2017 – 2021 PhD candidate
Degree from *University of Amsterdam, NL*
Research at *AMOLF & ARCNL, Amsterdam, NL*
Thesis *Patterning colloidal nanocrystals with light
& electrons*
Promotors *prof. dr. A. Polman*
prof. dr. B. Ehrler